Chemical Shuttle Additives in Lithium Ion Batteries

Final Technical Report

DE-EE0001938

Period Covered: October 2009 – May 2012

June 2014

Mary L. Patterson, Ph.D.
EnerDel, Inc.
3023 N. Distribution Way, #100
Greenfield, Indiana 46140

Prepared for the U.S. Department of Energy
National Energy Technology Laboratory
Under Contract Number DE-EE0001938

Perfluoro Aryl Boronic Esters as Chemical Shuttle Additives in Lithium Ion Batteries
Final Technical Report

June 2014

Mary L. Patterson, Ph.D.
EnerDel, Inc.
3023 North Distribution Way, #100
Greenfield, IN 46140

Redox shuttles could provide an added measure of control for lithium ion batteries beyond that which is provided by the battery management system. Redox shuttles, which are electrolyte additives, provide electrochemical overcharge protection. Since they possess a reduction-oxidation potential that is slightly above the maximum cathode potential during normal use, they should cause no degradation in cell performance during normal operation, but should shuttle excess electrons during overcharge conditions, effectively limiting the full cell voltage.

The goals of the Chemical Shuttle Additives program were to discover and implement a redox shuttle that is compatible with large format lithium ion cells utilizing $LiNi_{1/3}Mn_{1/3}Co_{1/3}O_2$ (NMC) cathode material and to understand the mechanism of redox shuttle action. Many redox shuttles, both commercially available and experimental, were tested and much fundamental information regarding the mechanism of redox shuttle action was discovered. In particular, studies surrounding the mechanism of the reduction of the oxidized redox shuttle at the carbon anode surface were particularly revealing.

Shuttles that were evaluated in various lithium ion cell chemistries include:

- 2-(pentafluorophenyl)-tetrafluoro-1,3,2-benzodioxaborole (BDB) supplied by Argonne National Laboratory (ANL), Lemont, Illinois
- 2,5-di-tert-butyl-1,4-dimethoxybenzene (DDB) supplied by 3M, St. Paul, Minnesota
- $Li_2B_{12}F_{12}$ supplied by Air Products, Allentown, Pennsylvania (pure compound) and Showa Denko, Japan (in electrolyte)
- 1,4-bis(2-methoxyethoxy)-2,5-di-*tert*-butyl-benzene (ANL-RS2) supplied by Argonne National Laboratory (ANL), Lemont, Illinois
- A 4.5V class redox shuttle supplied by Argonne National Laboratory (ANL), Lemont, Illinois

Although redox shuttles with an appropriate redox potential and sufficient chemical and electrochemical stability for cells utilizing cathodes with potentials higher and lower than that of NMC, a redox shuttle that is viable for use in large format lithium ion cells with NMC cathodes was not found.

The effect of the anode on the capacity loss of lithium ion cells with redox shuttles in cells utilizing lithium, lithium titanate, or graphite cells was studied.

Molecular imprinting of the redox shuttle molecule during solid electrolyte interphase (SEI) layer formation likely contributes to the successful reduction of oxidized redox shuttle species at carbon anodes. This helps understand how a carbon anode covered with an SEI layer, that is supposed to be electrically insulating, can reduce the oxidized form of a redox shuttle.

This material is based upon work supported by the Department of Energy national Energy Technology Laboratory under Award Number DE-EE0001938.

Full Legal Disclaimer

Table of Contents

Table of Figures

Table of Tables

1 SUMMARY

The goals of this program were to discover and implement a redox shuttle that is compatible with large format lithium ion cells utilizing $LiNi_{1/3}Mn_{1/3}Co_{1/3}O_2$ (NMC) cathode material and to understand the mechanism of redox shuttle action. Many redox shuttles, both commercially available and experimental, were tested and much fundamental information regarding the mechanism of redox shuttle action was discovered. In particular, studies surrounding the mechanism of the reduction of the oxidized redox shuttle at the carbon anode surface were particularly revealing.

The initial redox shuttle candidate, namely 2-(pentafluorophenyl)-tetrafluoro-1,3,2-benzodioxaborole (BDB) supplied by Argonne National Laboratory (ANL, Lemont, Illinois), did not effectively protect cells containing NMC cathodes from overcharge.

The ANL-RS2 redox shuttle molecule, namely 1,4-bis(2-methoxyethoxy)-2,5-di-*tert*-butyl-benzene, which is a derivative of the commercially successful redox shuttle 2,5-di-tert-butyl-1,4-dimethoxybenzene (DDB, 3M, St. Paul, Minnesota), is an effective redox shuttle for cells employing $LiFePO_4$ (LFP) cathode material. The main advantage of ANL-RS2 over DDB is its larger solubility in electrolyte; however, ANL-RS2 is not as stable as DDB. This shuttle also may be effectively used to rebalance cells in strings that utilize LFP cathodes. The shuttle is compatible with both LTO and graphite anode materials although the cell with graphite degrades faster than the cell with LTO, possibly because of a reaction with the SEI layer. The degradation products of redox shuttle ANL-RS2 were positively identified.

Commercially available redox shuttles $Li_2B_{12}F_{12}$ (Air Products, Allentown, Pennsylvania and Showa Denko, Japan) and DDB were evaluated and were found to be stable and effective redox shuttles at low C-rates. The $Li_2B_{12}F_{12}$ is suitable for lithium ion cells utilizing a high voltage cathode (potential that is higher than NMC) and the DDB is useful for lithium ion cells with LFP cathodes (potential that is lower than NMC). A 4.5 V class redox shuttle provided by Argonne National Laboratory was evaluated which provides a few cycles of overcharge protection for lithium ion cells containing NMC cathodes but it is not stable enough for consideration. Thus, a redox shuttle with an appropriate redox potential and sufficient chemical and electrochemical stability for commercial use in larger format lithium ion cells with NMC cathodes was not found.

Molecular imprinting of the redox shuttle molecule during solid electrolyte interphase (SEI) layer formation likely contributes to the successful reduction of oxidized redox shuttle species at carbon anodes. This helps to understand how a carbon anode covered with an SEI layer, that is supposed to be electrically insulating, can reduce the oxidized form of a redox shuttle.

2 INTRODUCTION

Redox shuttles could provide an added measure of control for lithium ion batteries beyond that which is provided by the battery management system. Redox shuttles, which are electrolyte additives, provide electrochemical overcharge protection. Since they possess a reduction-oxidation potential that is slightly above the maximum cathode potential during normal use, they should cause no degradation in cell performance during normal operation, but should shuttle excess electrons during overcharge conditions, effectively limiting the full cell voltage. The mechanism of redox shuttle action is that they are oxidized at the cathode during overcharge and diffuse to the anode, where they are reduced. This shuttling effect continues indefinitely for an ideal redox shuttle.

In reality, there are several technical challenges that must be overcome. The addition of redox shuttle compounds to lithium ion batteries is a relatively new concept that has not been attempted in large format lithium ion batteries. Among the potential technical challenges are:

- Chemical stability of the redox shuttle additive: ideally, the redox shuttle species should possess perfect chemical stability, that is, it should not react with any of the other chemicals and materials contained in the lithium ion cell in either its oxidized or reduced state.
- Electrochemical stability of the redox shuttle additive: ideally, the redox shuttle species should have perfect electrochemical reversibility.
- The redox shuttle additive may affect the performance of the battery adversely: ideally, the presence of the redox shuttle species should not interfere with key performance parameters such as initial and reversible cell capacities; C-rate capability; power capability; resistance; operating temperature range; operating voltage range; charge and discharge curves; calendar life; cycle life; self discharge; and any other relevant performance parameters. This is an important consideration due to the high concentration of redox shuttle species that needs to be present in the electrolyte to be effective at inhibiting overcharge. Of special significance is that redox shuttle species are likely incorporated into the solid electrolyte interphase (SEI) layer on carbon electrodes.
- The diffusion coefficient of the redox shuttle additive must be high enough so that a large current density can be tolerated during overcharge: the diffusion coefficient depends on, among other considerations, the additive's size, shape, molecular weight, charge, electrolyte viscosity, and solvation.
- Redox shuttle additives need to be inert toward all internal cell materials.
- Too much heat may be generated during the redox process: the redox shuttle by its very nature mimics a soft internal short. Heating occurs during the shuttling process and the localized heat that is produced may disrupt the SEI layer, causing degradation of the lithium ion cell. The heating rate depends on the magnitude of current that the redox shuttle agent needs to shuttle to prevent overcharge.

This report describes the evaluation of experimental and commercially available redox shuttles. Additionally, fundamental studies on topics such as the effect of the anode on overcharge cycle life and how the oxidized form of the redox shuttle is reduced at the anode were performed.

3 RESULTS

3.1 Redox Shuttle BDB

The initial sample of the initial redox shuttle additive (2-(pentafluorophenyl)-tetrafluoro-1,3,2-benzodioxaborole, or BDB) from Argonne National Laboratories (ANL) was 0.5 grams and the second was 1.0 grams for a total of 1.5g total received. This small quantity necessitated the use of coin cells for initial testing, since coin cells require only 100µl of electrolyte. For a 3% concentration by weight of BDB, only about 3.6 mg of BDB is required for each coin cell. Larger pouch cells were employed as larger quantities of BDB and other redox shuttles became available.

Cyclic voltammetry (CV) was run on a 1 mM solution of BDB in an electrolyte of 25% ethylene carbonate (EC), 5% propylene carbonate (PC), 70% ethyl methyl carbonate (EMC), and 1.2M $LiPF_6$. A three electrode electrochemical cell consisting of a platinum working electrode and lithium metal counter and reference electrodes was employed. The result is shown below and confirms the 4.43 V reduction-oxidation potential. It also shows a E_{ox}-E_{red} = ΔE = 85 mV, which means that the system is not completely reversible. According to theory, a completely reversible system has a ΔE of 60 mV.

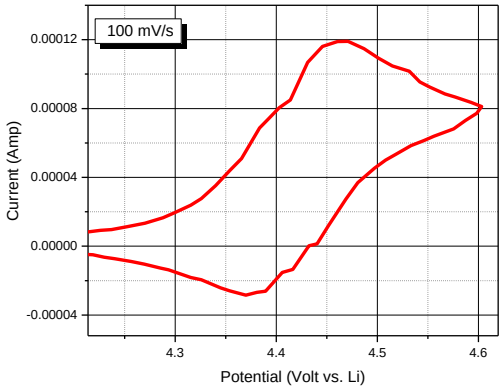

Figure 1. Cyclic voltammogram (CV) of BDB

The diffusion coefficient of BDB was determined to be 1.38 x 10^{-5} cm^2/sec using the Randles-Sevcik equation and the CV of BDB at different scan rates.

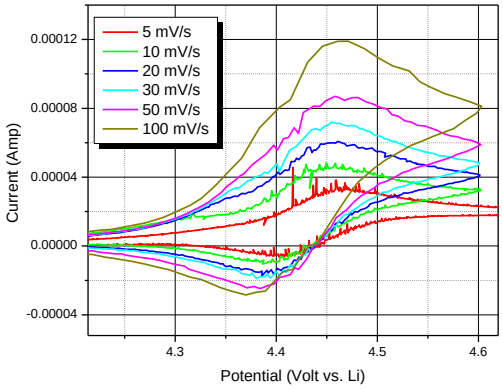

Figure 2. CV of BDB at various scan rates

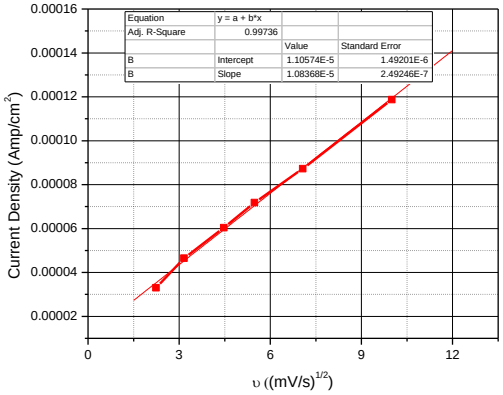

Figure 3. Best fit line to data for BDB diffusion coefficient calculation

To be an effective redox shuttle, the long term electrochemical and chemical stability is of critical importance. The electrochemical reversibility of BDB in electrolyte was evaluated using a larger voltage window. Carbon anodes typically reach almost 0 mV when the cell is charged, while the NMC cathode may reach 4.2 V (all potentials in this report are vs. Li/Li^+ unless otherwise stated). The voltage window 4.8 V to 0.1 V was scanned and the results are below.

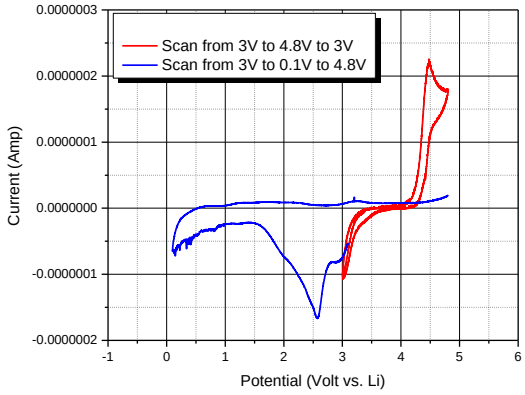

Figure 4. CV of BDB in the voltage range 4.8V to 0.1V

It can be seen that there is a large reduction reaction occurring around 2.6 V. The nature of the reduction reaction is unknown and may be related to the BDB itself, impurities such as unreacted starting materials or water in the BDB, or products of chemical or electrochemical instability of the BDB. To evaluate the electrochemical reversibility, fifty CV scans in the voltage range 4.8 to 0.1 V were run and the results are below.

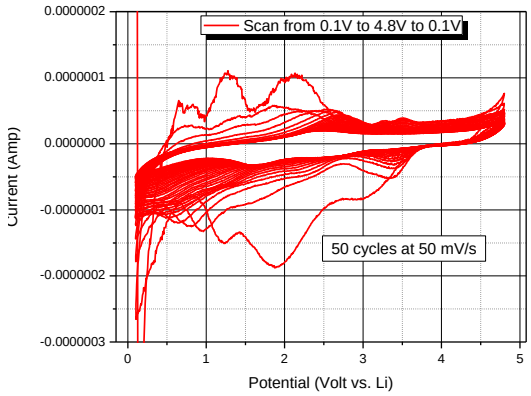

Figure 5. Fifty CV cycles between 4.8V and 0.1V

After the scans, the platinum working electrode had a brown residue on the surface, indicating that degradation of the BDB had occurred.

Coin half cells were made using NMC or hard carbon to determine the effect of the presence of BDB on the initial, reversible, and irreversible capacity of the anode and cathode active materials. The first cycle formation results for the NMC half cell is shown below.

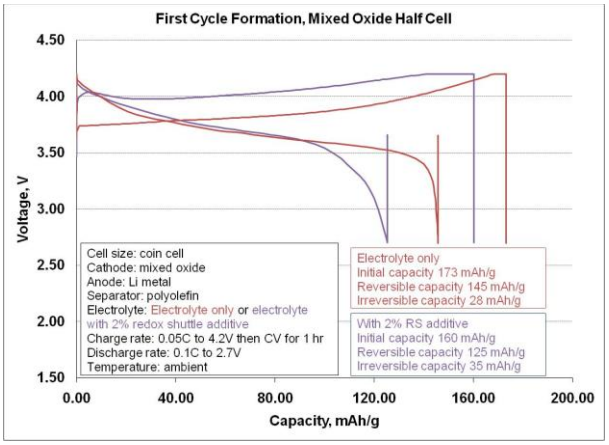

Figure 6. First cycle formation for NMC half cell with and without BDB

The BDB displaces the charge curve and produces a larger irreversible capacity and smaller reversible capacity. The discharge rate capability of the NMC half cells is also adversely affected by the presence of the BDB.

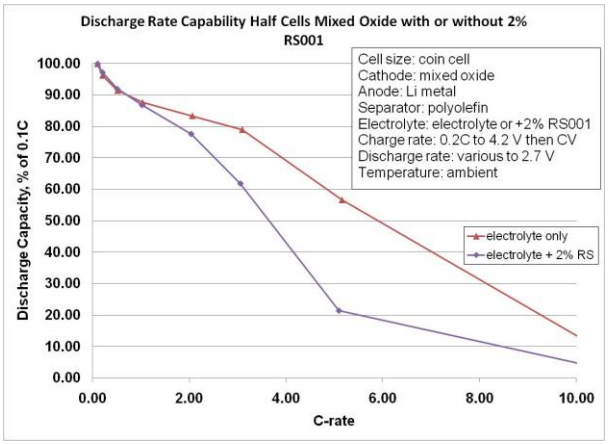

Figure 7. Discharge rate capability of NMC half cells with and without BDB

Hard carbon half cells were evaluated next with and without BDB and the first cycle formation results are below.

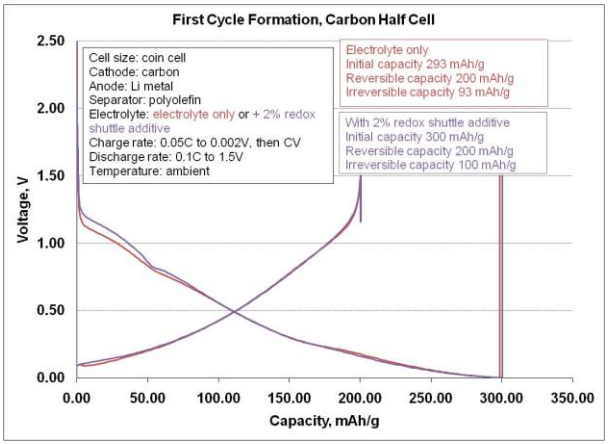

Figure 8. First cycle formation of hard carbon half cells with and without BDB

The initial and reversible specific capacity of the hard carbon is not affected by the presence of the BDB. The discharge rate capability is also not affected very much by the presence of the BDB, as seen below.

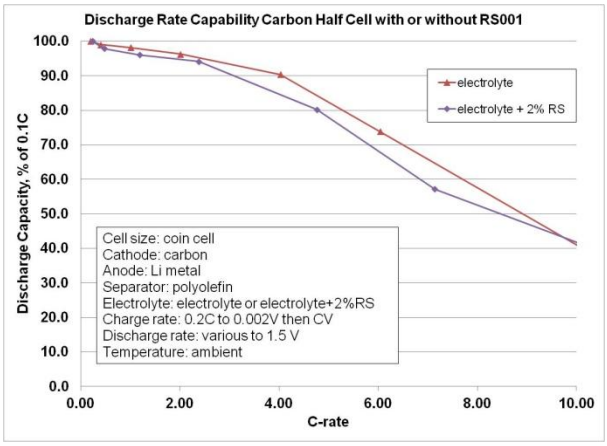

Figure 9. Discharge rate capability of hard carbon half cells with and without BDB

Full coin cells of NMC and hard carbon were activated with electrolyte with and without BDB and the first cycle formation results are below.

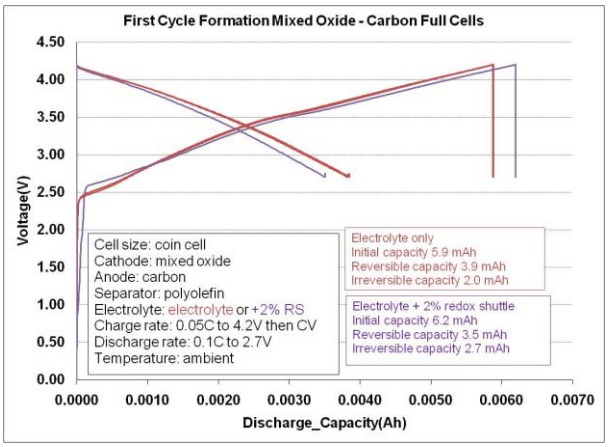

Figure 10. First cycle formation for NMC-hard carbon full cells

The full cells containing the BDB have a larger initial capacity and smaller reversible capacity than those without BDB. Cycling at a 1C rate was performed for almost 200 cycles and the results are below.

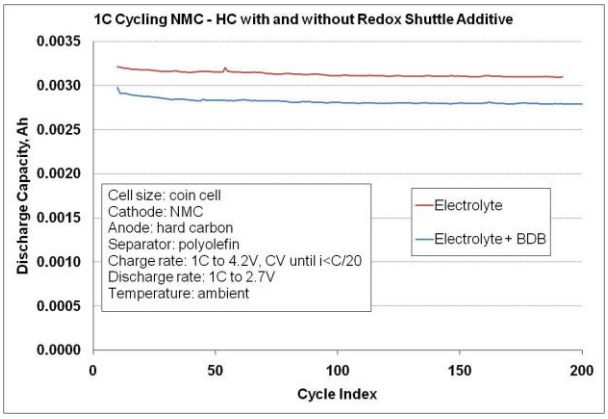

Figure 11. 1C cycling NMC-hard carbon full cells

The cells containing the BDB have a decreased capacity compared to those without, but the cycling does not seem to be affected adversely. Overcharge cycles were run after the 200 normal charging cycles and the BDB was found to not protect the cells from overcharge, as seen below.

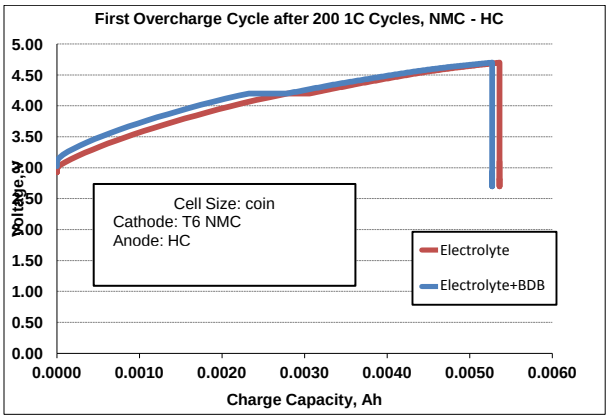

Figure 12. First overcharge cycle after 200 normal charge cycles

ANL suggested that the BDB can be stabilized and its performance can be enhanced by the addition of LiF. The BDB is a strong Lewis base because the boron is surrounded by only three pairs of electrons. This causes instability because it will react with many chemical entities to fill that empty fourth orbital. Fluoride ion from the LiF ion pairs with the BDB and stabilizes it by reducing its reactivity. Coin half cells were constructed using NMC and activated with electrolyte containing BDB and LiF and the first cycle formation results are below.

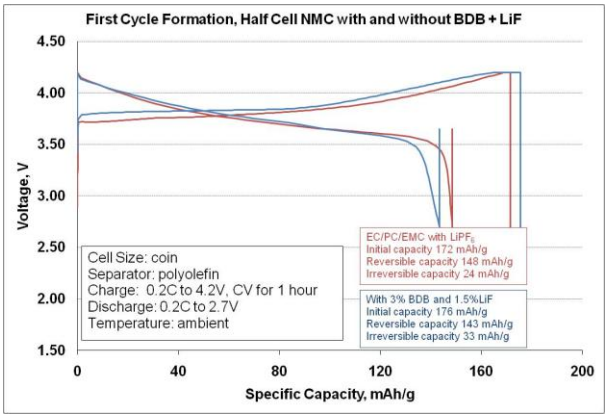

Figure 13. First cycle formation for NMC half cells with and without BDB+LiF

Addition of LiF to the BDB improves the specific capacity of the NMC half cells compared to the BDB alone. It also improves the charging curve voltage profile, making it match more closely with the cells that do not contain BDB.

Ten overcharge cycles were run on these coin cells. The cells were charged to either 150% overcharge or 4.7 V, whichever came first. The first cycle showed partial overvoltage protection, as can be seen below.

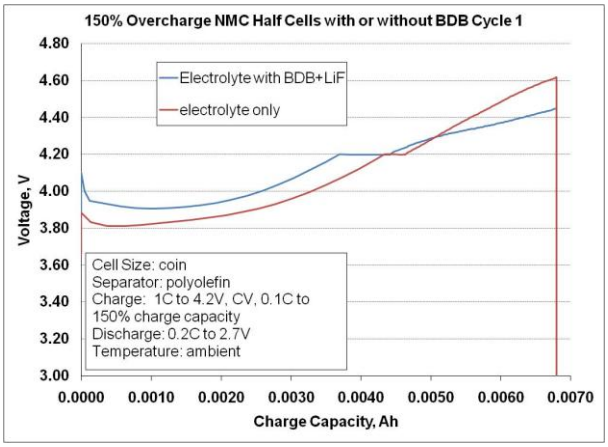

Figure 14. First overcharge cycle after formation for NMC half cells

The BDB did not provide any overcharge protection in the second through tenth overcharge cycles. The tenth overcharge cycle is shown below.

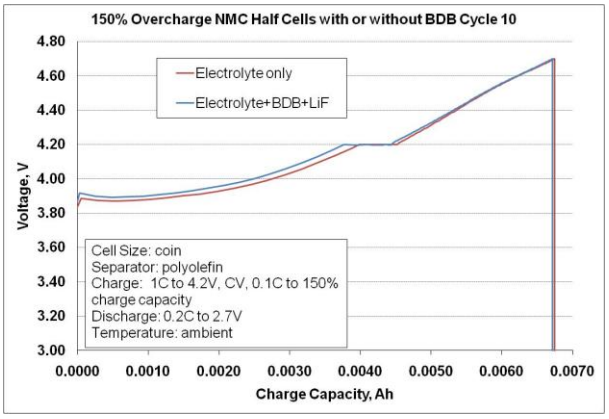

Figure 15. Tenth overcharge cycle after formation for NMC half coin cells

BDB exhibits neither the electrochemical nor chemical stability necessary to be an effective redox shuttle. It was not known if the lack of performance is due to an inherent property of the molecule, an impurity such as water or unreacted starting material, or a product formed by electrochemical or chemical instability.

To evaluate the effect that impurities might have on the performance of the BDB, a source (Daikin, Japan) of extremely pure $C_4F_4(OH)_2$ was located and sent to Argonne National Laboratories to be converted into 2-(pentafluorophenyl)-tetrafluoro-1,3,2-benzodioxaborole (BDB). This provided a level of purity that allowed a true evaluation of the molecule's capability as a redox shuttle agent. Two samples of high purity BDB were prepared at Argonne: precipitated and sublimed. Their purity was confirmed using gas chromatography – mass spectrometry. The sublimed sample had higher purity than the precipitated sample as described later in this report, and both samples were of higher purity than the previous samples. However, neither sample of pure BDB was effective in providing overcharge protection for cells with NMC cathodes and further evaluation of BDB was discontinued.

3.2 Redox Shuttle $Li_2B_{12}F_{12}$

While the Argonne National Laboratories redox shuttle molecule purity issues were being resolved, we decided to evaluate $Li_2B_{12}F_{12}$, which has been previously reported as a high voltage redox shuttle [1]. Cyclic voltammetry (CV) was run on a 1.0 M $LiPF_6$ in 25/5/70 EC/PC/EMC solution (baseline electrolyte) with 0.1 M of $Li_2B_{12}F_{12}$ as the redox shuttle additive. A three electrode electrochemical cell consisting of a platinum working electrode and lithium metal counter and reference electrodes was employed. The result is shown in Figure 16 and has a 4.7 V reduction-oxidation potential which is 0.1 V higher than reported. It also has a E_{ox}-E_{red} = ΔE = 140 mV which is higher than reported (100 mV) and higher than expected for a fully reversible system (60 mV) although this value may be higher due to uncompensated solution resistance in the experiment rather than poor reversibility. It is not clear what is responsible for the peaks at 3.2 or 2.5 V although it does not appear to be due to impurities in the electrolyte since the baseline solution does not have them.

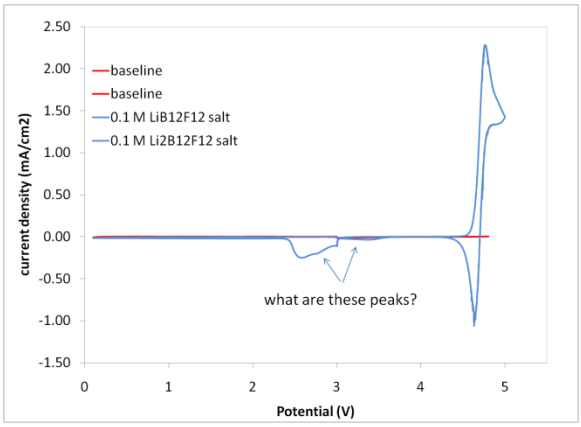

Figure 16. CV of 0.1M $Li_2B_{12}F_{12}$ in 1.0 M $LiPF_6$ in baseline electrolyte

The diffusion coefficient of $Li_2B_{12}F_{12}$ was determined to be 1.22 x 10^{-6} cm^2/s using the Randles-Sevcik equation and the CV of $Li_2B_{12}F_{12}$ at different scan rates (Figures 17 and 18) which is lower than reported by Argonne (2.1 x 10^{-6} cm^2/s) but the electrolyte solution is different which can affect the diffusion coefficient. The scan at 100 mV/s does not have as high a current as expected and was not used in calculating the diffusion coefficient. The lower current at 100 mV/s might be cause by slow oxidation kinetics.

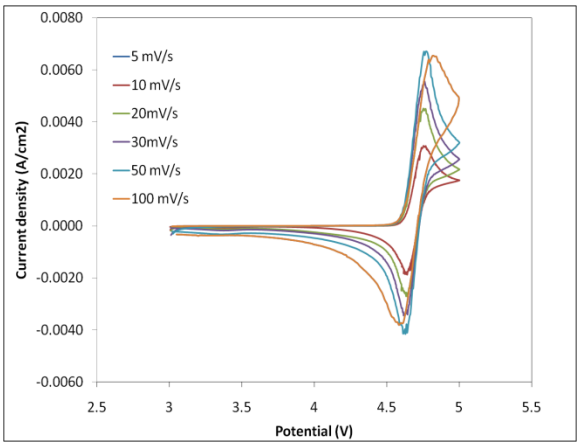

Figure 17. CV of 0.1M $Li_2B_{12}F_{12}$ in baseline electrolytes at varying rates

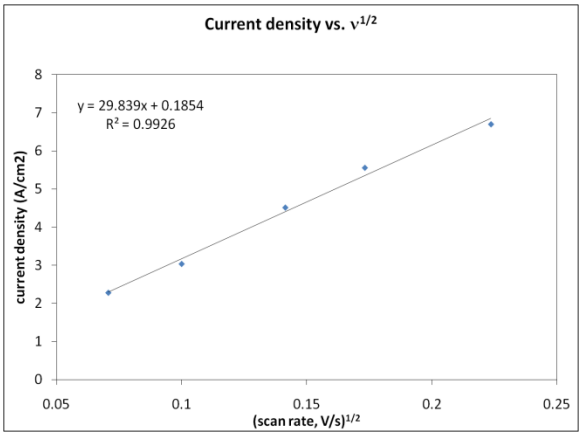

Figure 18. Best fit line for diffusion coefficient of 0.1M $Li_2B_{12}F_{12}$ in baseline electrolyte

The electrolyte solution with the $Li_2B_{12}F_{12}$ shuttle was continuously cycled between 3.0 and 5.0 V. Repeated cycling reduces the current as can be seen in Figure 19. However, when the electrode was cleaned, the current returned to the original value which suggests that a passivating layer may be formed on the Pt electrode. The passivation of the Pt electrode might be caused by the oxidation of electrolyte solvents (they start to oxidize at about 4.7 V) and have nothing to do with the redox shuttle.

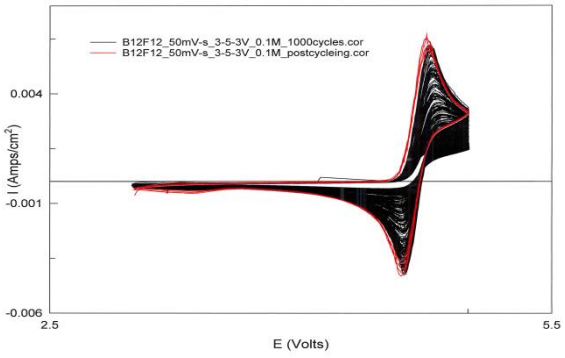

Figure 19. Continuous CV of electrolyte with the $Li_2B_{12}F_{12}$ redox shuttle

Half cells were constructed with NMC cathode material in pouch cells and cycling was performed. The electrolyte used in all cell testing was 1.0 M $LiPF_6$ 25/5/70 EC/PC/EMC + 0.1 M $Li_2B_{12}F_{12}$ which was compared to our baseline electrolyte 1.2 M $LiPF_6$ in 25/5/70 EC/PC/EMC so that both were 1.2 M in Li^+ ions. The cells were formed under normal conditions (charged to 4.2 V and discharged to 2.7 V at slow rates). The average first charge and discharge capacities and first cycle Coulombic efficiency are shown in Table 1 below and are not significantly different from the baseline. It is worth noting that the Coulombic efficiency is nearly the same as the baseline, so the redox shuttle is not active up to 4.2 V.

	Baseline	Baseline + RS
1st Chg (mAh)	54.74	54.87
1st DChg (mAh)	48.00	48.10
Efficiency (%)	87.68	87.66

Table 1. Formation data for NMC half cell (RS= $Li_2B_{12}F_{12}$)

These NMC half cells were then overcharged at a C/5 rate to 200% state-of-charge (SOC) or 4.95 V, whichever occurred first. While the baseline cells reached 4.95 V during the first overcharge cycle, Figure 20, cells with $Li_2B_{12}F_{12}$ were limited to about 4.75 V for the first 15 overcharge cycles, Figures 20 and 21. However, it is clear that the overcharge protection begins to fade since the voltage at the end of each overcharge cycle increases with cycle number as the cells are continually overcharged, Figures 21 and 22.

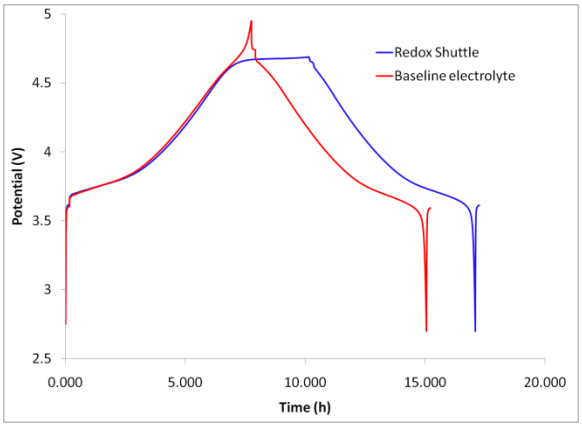

Figure 20. NMC half cells with and without $Li_2B_{12}F_{12}$ redox shuttle during overcharge

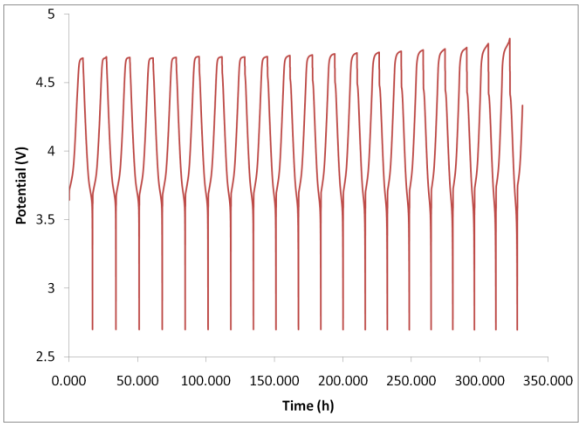

Figure 21. First 20 overcharge cycles in a NMC half cell with and without $Li_2B_{12}F_{12}$

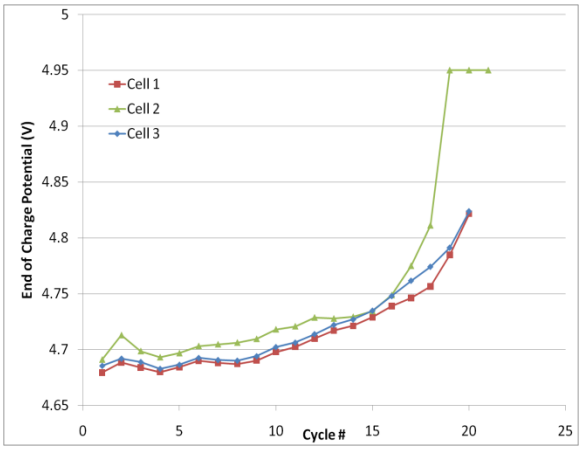

Figure 22. NMC half cell potentials after cells containing $Li_2B_{12}F_{12}$ were overcharged 200%

The overcharge protection provided by the redox shuttle does afford some extra cycle life to NMC half cells compared to cells without the shuttle, Figure 23.

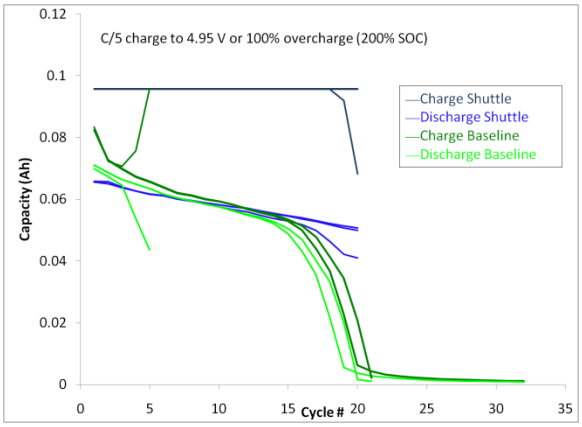

Figure 23. Cycle life of NMC half cells with $Li_2B_{12}F_{12}$ (blue) and without (green)

Half cells with hard carbon anode material in pouch cells were also tested. The formation data is shown in Table 2. The capacity for the electrolyte with the redox shuttle is a little lower but no taper charging was performed which may have affected the results. The rate capability, Figure 24, is also a little lower and this is probably due to differences in the conductivity of the electrolyte. Overall though, there does not appear to be any significant problem or incompatibility of the redox shuttle (in its reduced form) with the hard carbon anode material.

	Baseline	Baseline + RS
1st Chg (mAh)	28.9	25.8
1st DChg (mAh)	39.3	35.7
Efficiency (%)	73.7	72.1

Table 2. Formation data for hard carbon half cells (RS = $Li_2B_{12}F_{12}$)

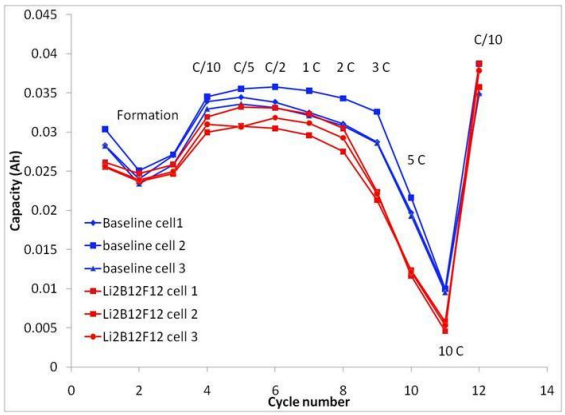

Figure 24. Comparison of HC half cell discharge rate with and without $Li_2B_{12}F_{12}$

Formation and rate testing of NMC-hard carbon full cells showed little to no effect of the $Li_2B_{12}F_{12}$ redox shuttle on the formation cycles, Table 3, and the rate capability of the cell, Table 4, compared to cells with the baseline electrolyte.

Table 3. Formation data for NMC/HC full cells (RS = $Li_2B_{12}F_{12}$)

	Baseline	Baseline + RS
1st Chg (mAh)	55.3	55.5
1st DChg (mAh)	39.5	39.2
Efficiency (%)	71.3	70.5

Table 4. Discharge rate capability for full cells with and without the redox shuttle $Li_2B_{12}F_{12}$

Rate	Avg. Baseline capacity (mAh)	Avg. Redox shuttle capacity (mAh)
C/10	38.1	37.9
C/5	37.6	37.4
C/2	36.7	36.2
1 C	35.6	34.5
2 C	33.4	29.8
3 C	26.1	22.0
5 C	11.8	12.0
10 C	4.9	5.3
C/10	37.6	37.5

The cells were then cycled 100 times between 2.7 and 4.2 V (no overcharge), Figure 25. The cells with the redox shuttle initially had lower capacity but cycled well and actually appear to have a slightly slower capacity fade rate. The Coulombic efficiency of the cells with the redox shuttle (Figure 26) was near 100% which demonstrates that the shuttle was not at all active during cycling up to 4.2 V. If the shuttle was active the Coulombic efficiency would be lower since charge would be consumed by the shuttling process.

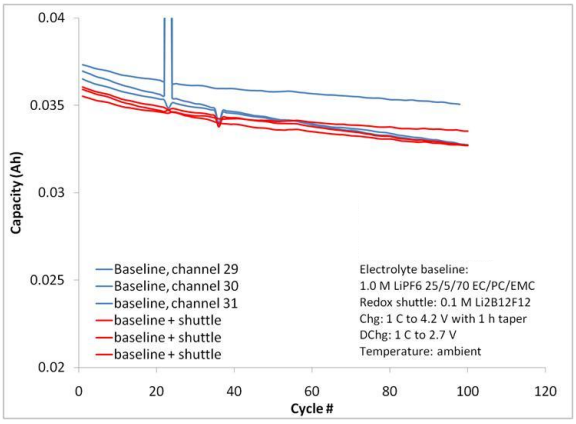

Figure 25. NMC-HC with $Li_2B_{12}F_{12}$ cycling under a normal voltage profile

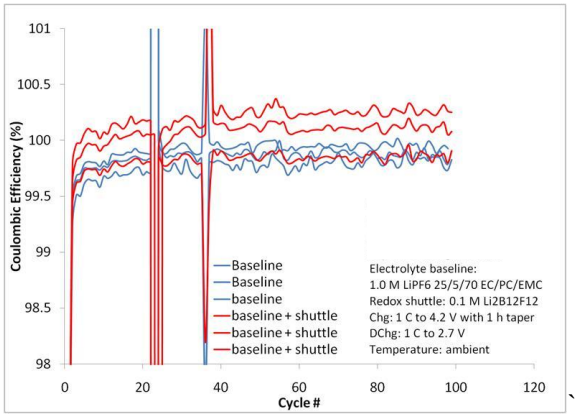

Figure 26. NMC-HC with $Li_2B_{12}F_{12}$ Coulombic efficiency during normal cycling conditions

Following 100 cycles between 4.2 and 2.7 V, the full cells were then overcharged to 200% state-of-charge (SOC) or 4.95 V, whichever occurred first, similar to the testing with the NMC half cells. The redox shuttle material was still active and functioning after cycling under normal conditions. The voltage of the cells with the redox shuttle did not reach 4.95 V during 200% charging for the first 6-8 overcharge cycles, Figure 27. The initially lower capacity of the cells with the redox shuttle is expected since the cells are not as highly charged as the baseline cells because the redox shuttle is functioning, Figure 28. As the shuttle's ability to prevent overcharge fades, the cell capacity initially increases. However, the cycle life of cells with the redox shuttle was actually *worse* than cells with no redox shuttle during overcharge, presumably due to cells containing redox shuttle spending more time at the overcharge voltage than cells with no redox shuttle. This is in direct contrast to the results with the NMC half cells, Figure 23. Because the redox shuttle seems to improve cycle life in NMC half cells and the reduced form of the shuttle (the species present during normal cycling) does not hurt cycle life in full cells, the reduced cycle life of cells

containing the redox shuttle in full cells may be caused by a poor interaction of the oxidized form of the shuttle with the hard carbon anode or its SEI layer that it does not have with the lithium metal anode in the NMC half cells. The Li anode may reduce the oxidized form of the redox shuttle more quickly or more cleanly than hard carbon does. Additionally, if Li is consumed, a half cell is a more plentiful reservoir of lithium than a full cell, resulting in less capacity fade.

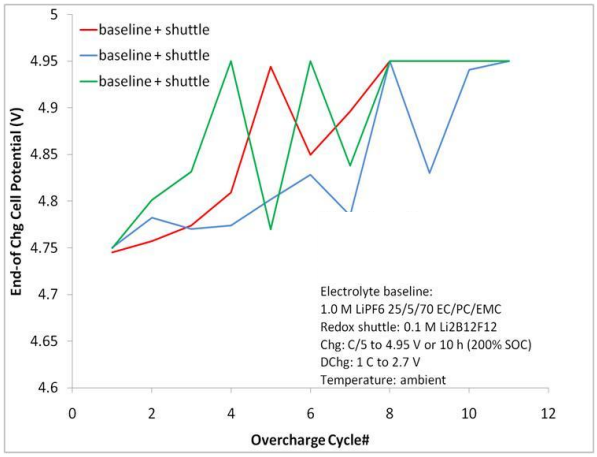

Figure 27. End of charge cell potential during 200% overcharge

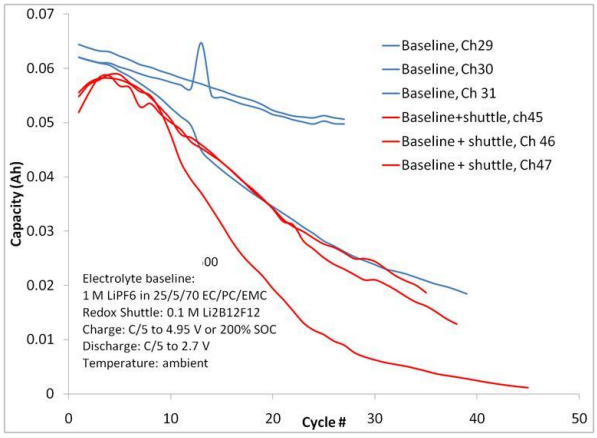

Figure 28. Full cell discharge capacity versus cycle number during overcharge

The $Li_2B_{12}F_{12}$ redox shuttle provides about 6 to 8 cycles of overcharge protection in an NMC – hard carbon full cell. It has a redox potential of 4.6-4.7 V which is probably too high for use in cells with NMC cathodes, where the normal charging voltage is about 4.1 to 4.2 V. It may however be ideal for cathodes that operate around a potential of 4.5 V.

3.3 Diffusion coefficient and maximum charge rate for BDB and $Li_2F_{12}B_{12}$

The diffusion coefficients for $Li_2B_{12}F_{12}$ and 2,5-di-tert-butyl-1,4-dimethoxybenzene (DDB) were evaluated. Both $Li_2B_{12}F_{12}$ and DDB have been previously reported as redox shuttles for Li-ion batteries

[1,2]. The diffusion constant was measured in two different standard electrolytes because the solvent viscosity can impact the diffusion coefficient, which ultimately affects the maximum current that can be shuttled.

Using Equation 1, the diffusion coefficient may be calculated after measuring the peak current at various scan rates during a cyclic voltammetry experiment.

Equation 1 $$I_p = 2.69x10^5 \cdot n^{3/2} \cdot A \cdot D^{1/2} \cdot v^{1/2} \cdot C$$

where I_p = peak current in amperes;

n = number of electrons transferred;

A = electrode area in cm^2;

D = diffusion coefficient in cm^2/second;

v = voltage scan rate in volts/second; and

C = concentration of redox shuttle in moles/cm^3.

The cyclic voltammograms of 1 mM BDB (Figures 29 and 30), DDB (Figures 31 and 32), and $Li_2B_{12}F_{12}$ (Figures 33 and 34) in the electrolytes 1.2 M $LiPF_6$ in 30/70 EC/DEC (electrolyte #1) and 1.2 M $LiPF_6$ in 25/5/70 EC/PC/EMC (electrolyte #2) are shown below. The scan rates used were 5, 10, 20, 30, 40, 50, and 100 mV/s.

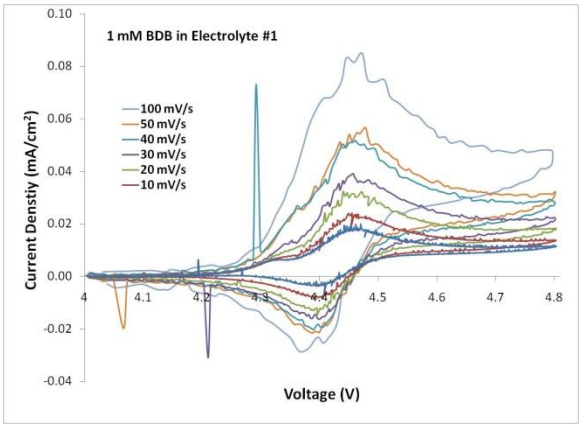

Figure 29. Cyclic voltammograms of 1 mM BDB in electrolyte #1

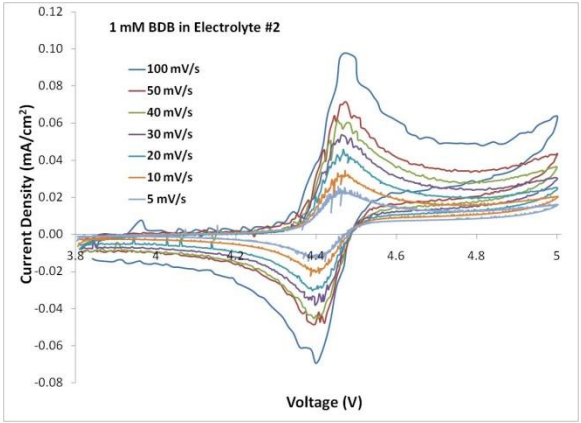

Figure 30. Cyclic voltammograms of 1 mM BDB in electrolyte #2

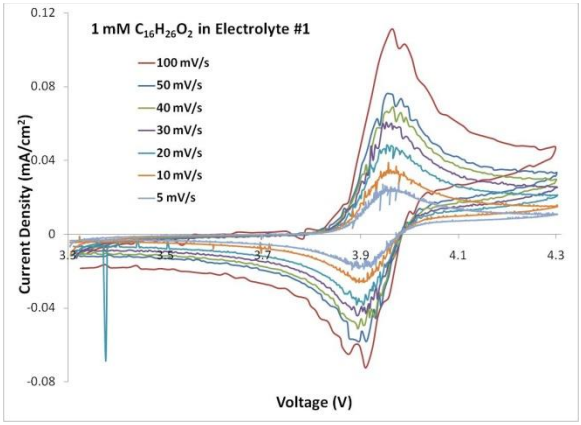

Figure 31. Cyclic voltammograms of 1 mM DDB in electrolyte #1

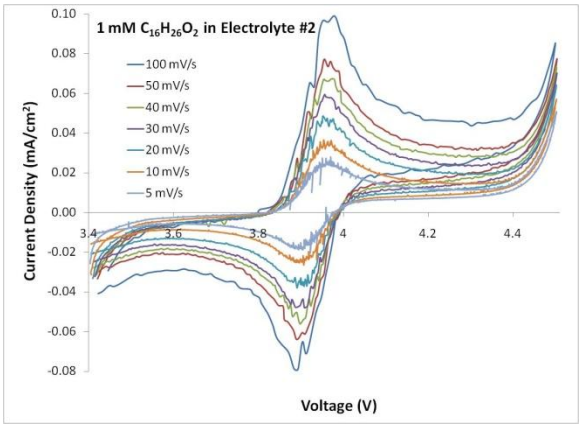

Figure 32. Cyclic voltammograms of 1 mM DDB in electrolyte #2

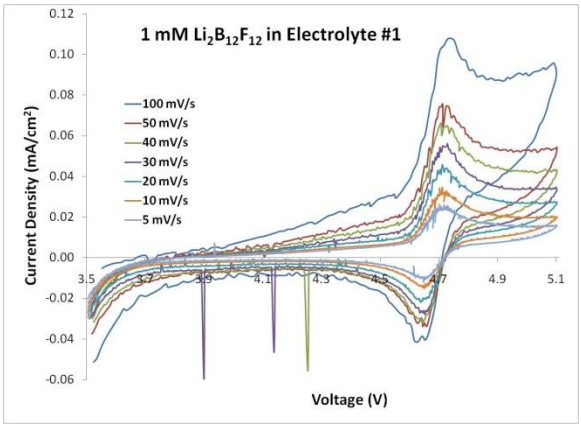

Figure 33. Cyclic voltammograms of 1 mM $Li_2B_{12}F_{12}$ in electrolyte #1

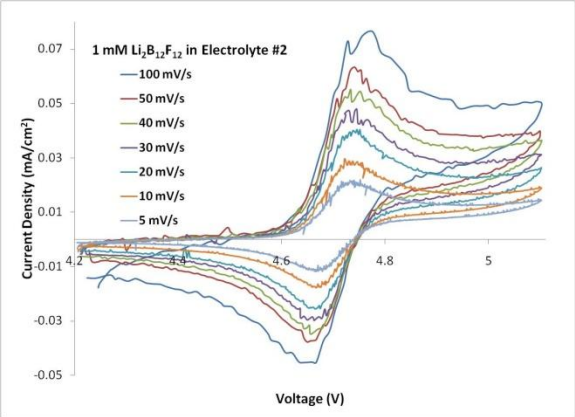

Figure 34. Cyclic voltammograms of 1 mM $Li_2B_{12}F_{12}$ in electrolyte #2

A summary of the redox potential and diffusion coefficient for these three redox shuttles is shown in Table 5. The first two values are from the literature [1, 2].

Table 5. Redox potentials and diffusion coefficients for redox shuttles

Redox Shuttle	Electrolyte Composition	Average Redox Oxidation Potential, V	Diffusion Coefficient, cm^2/sec
$Li_2B_{12}F_{12}$	1M $LiPF_6$ in 3:7 EC:EMC	4.6	2.1×10^{-6}
DDB	0.5 M LiBOB in 1:2:1:2 PC:DMC:EC:DMC	3.95	1.6×10^{-6}
$Li_2B_{12}F_{12}$	#2	4.72	9.76×10^{-7}
$Li_2B_{12}F_{12}$	#1	4.70	1.55×10^{-6}
DDB	#2	3.96	1.35×10^{-6}
DDB	#1	3.95	1.69×10^{-6}
BDB	#2	4.47	1.12×10^{-6}
BDB	#1	4.45	1.08×10^{-6}

The redox potential of the shuttle should be about 0.1 to 0.3 V above the maximum potential that the cathode reaches during normal charging. If the oxidation potential of the redox shuttle molecule is too low, the shuttle will be oxidized during normal charging. This would cause inefficient and incomplete cell charging because some of the charging current would be consumed by the oxidation of the redox shuttle molecule. If the oxidation potential of the redox shuttle molecule is too high, damage to the cell may occur and significantly shorten its life. In an extreme case, the shuttle would provide no protection at all. Based on this consideration, cells with layered oxide cathode materials that operate at 4.1 to 4.2 V should employ a redox shuttle with an oxidation potential in the range of about 4.2 to 4.5 V. The oxidation potential of $Li_2B_{12}F_{12}$ at about 4.7 V is too high but this material might be suitable for high voltage cathodes. The DDB has an oxidation potential of about 3.95V that is too low for mixed oxide cathodes but might be useful for $LiFePO_4$. The BDB has a redox potential in the desired range for mixed oxide cathodes but it does not provide effective overcharge protection in full cells with NMC cathodes and hard carbon anodes.

The diffusion coefficient of the redox shuttles varies with the electrolyte and in large part is influenced by the viscosity of the solution. For $Li_2B_{12}F_{12}$ and DDB, the diffusion coefficient is higher in electrolyte #1. For BDB, the diffusion coefficient is slightly higher in electrolyte #2 than electrolyte #1. This difference might because of an interaction between the BDB which is a Lewis acid and the carbonate solvents which are Lewis bases. This could also explain the lower diffusion coefficient for BDB compared to $Li_2B_{12}F_{12}$ which has a similar molecular mass.

The diffusion rate of the redox shuttle governs an upper limit on the charge current that may be shuttled once the redox potential of the shuttle is reached. A cell charged above this rate would enter into overcharge despite the presence of the redox shuttle molecule. The maximum charge current density in A/cm^2 may be calculated from the diffusion coefficient, D (cm^2/sec), using equation 2 where n is the number of electrons removed in the oxidation (dimensionless), F is Faraday's constant (96485 coulombs/mole), C is the concentration (mol/cm^3), and L is the distance between the electrodes (cm).

Equation 2 $$I_{max}/A = nFDC/L$$

In terms of C-rate, the maximum charge current varies depending on the cell capacity. For high energy cells such as that would be used in EV applications, the theoretical maximum C-rate is about 1 to 2C. For high power applications, in which the cells have smaller capacity but similar geometry, the theoretical maximum current corresponds to about a 2 to 4 C-rate. Since high power applications demand higher C-rates, redox shuttles are unlikely to be applicable for high power cells. Further, due to tortuosity and other factors in real lithium ion cells, the maximum C-rate attainable is realistically on the order of 0.5C.

3.4 Electrolyte stability and the effect of moisture

During the course of testing, the solutions of some of the electrolytes were observed to become yellow over time in the presence of DDB and BDB, while control solutions of electrolyte alone remained colorless. The yellowing of electrolyte solutions is thought to be related to organic compounds formed after the breakdown of $LiPF_6$ as shown in Scheme 1. The hydrofluoric acid (HF) concentration is higher in the DDB solution with the more intense yellow color as shown in Table 6. It is not clear why the DDB or BDB should cause the yellowing of the electrolyte solution. The DDB or BDB may be involved in the decomposition of $LiPF_6$ by shifting the equilibrium in the top reaction of Scheme 1 to the right. Also, trace contaminants or other decomposition products may be involved.

$$LiPF_6 \rightleftharpoons LiF + PF_5$$

$$PF_5 + H_2O \rightarrow POF_3 + 2HF$$

Scheme 1

Table 6. Moisture and HF content of electrolytes with DDB and BDB

Electrolyte	Average Moisture Concentration, ppm	Average HF Concentration, ppm
Electrolyte #2	7.12	---
Electrolyte #1	3.35	---
1 mM DDB in #2 (very yellow)	5.72	74
1 mM DDB in #1 (slightly yellow)	4.87	48
1 mM BDB in #2	3.91	---
1 mM BDB in #1	2.94	---

Freshly prepared electrolytes with BDB had lower water content than electrolytes without BDB. BDB is a Lewis acid and may shift the equilibrium of the decomposition of $LiPF_6$ shown in Scheme 1 to the right by abstracting fluoride ion to form a new Li salt. The abstraction of fluoride from $LiPF_6$ yields PF_5 which readily reacts with water to form HF. POF_3 has been shown to catalyze the decomposition of organic carbonate solvents [3]. This could explain the lower measured water content and yellowing of the solution. Further, BDB reacts with water to form the starting materials of the synthetic reaction, namely TFC (3,4,5,6-tetrafluorocatechol) and pentafluorobenzene boronic acid, as shown later in this report. Both of these reactions may explain the lower concentration of water in the electrolyte solutions after the addition of BDB.

The reactions that result in the yellow color of the electrolyte also appear to be responsible for the irreversible oxidation of the redox shuttle. Electrolyte with DDB that was stored for one month that had a yellow color did not have a reversible peak at 3.95 V as it did when the electrolyte was freshly prepared as shown in Figure 35. Also, the addition of water to electrolyte containing BDB produces an irreversible oxidation peak at 4.45 V, as shown in Figure 36. This is important since a by-product of BDB synthesis is water (condensation reaction) and water could be an impurity. Further, water enters cell packaging that is not hermetically sealed. Water may react with BDB to form the starting materials.

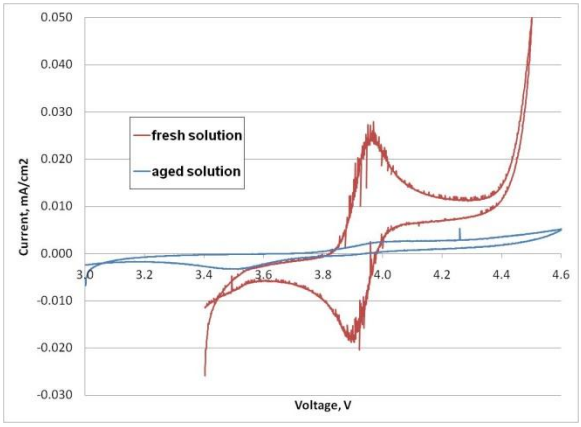

Figure 35. CVs of fresh electrolyte with DDB and after 1 month of storage

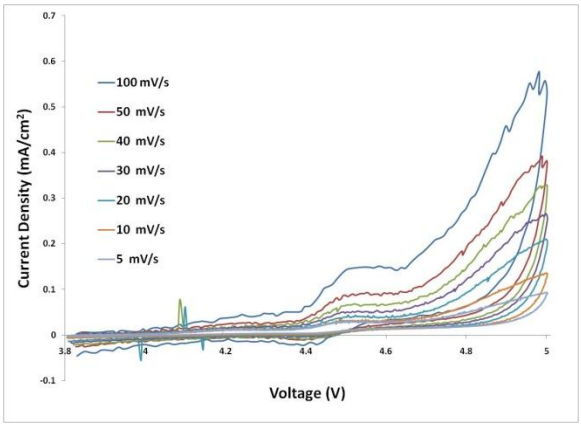

Figure 36. CVs of 1 mM BDB and 1% water added to electrolyte #2.

3.5 Effect of LiF and SEI film formation

As previously stated, BDB is a Lewis acid. It has a 3-coordinate boron center that may accept a Lewis base such as F^-. It was suggested by Argonne National Laboratory that the addition of LiF stabilizes the BDB. The fluoride ion complexes the BDB, forming an anion. This anion is expected to be less susceptible to hydrolysis and would be less likely to abstract fluoride from the PF_6^- anion.

Cyclic voltammetry of the BDB with and without the addition of LiF also shows that there are differences in the reduction potential at a graphitic electrode. Without the addition of LiF, there is a reduction peak at 1.3 V during the first scan from 3 to 0 V at a rate of 1 mV/sec and a graphite working electrode, as shown in Figure 37. With the addition of LiF, the reduction peak at 1.3 V is not present. Also, the peak at about 0.6 V which is attributed to solvent reduction is suppressed in the electrolyte of the BDB without LiF. Without the addition of LiF, the BDB has an electron deficient three coordinate boron center that is likely easily reduced. Addition of LiF not only fills the boron atom's outer shell with eight electrons but also forms an anion which could be more stable than a neutral species.

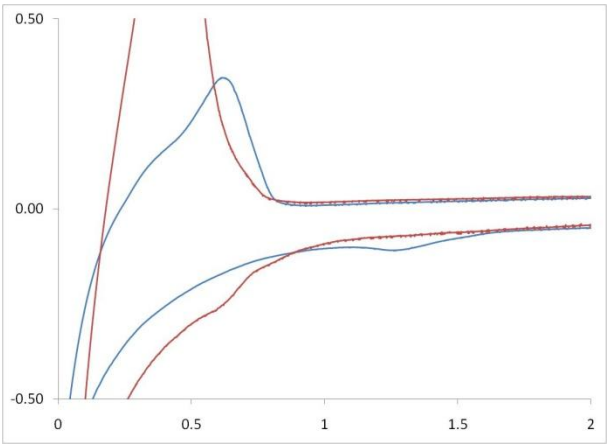

Figure 37. CVs of BDB without LiF (blue) and with LiF (red)

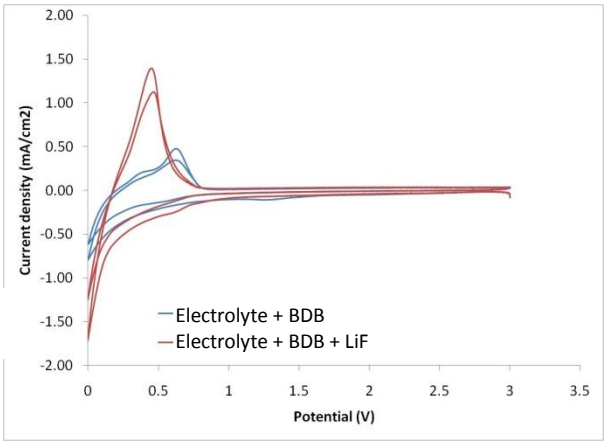

Figure 38. Cyclic voltammograms of BDB without LiF (blue) and with LiF (red)

The BDB without LiF therefore appears to be involved in the formation of the SEI layer on the graphite surface. Continued reduction of BDB does not appear to occur as the reduction peak at 1.3 V is not present on subsequent cycles as shown in Figure 38. Also, the suppression of the peak at 0.6 V suggests that there are less solvent reduction products in the SEI. The lithium intercalation into the graphite is shifted to more negative potentials and its deintercalation is shifted to more positive potentials. This suggests that the film formed from the BDB without LiF may be more resistive than films formed with BDB and LiF or standard electrolytes. The cyclic voltammogram of electrolyte with BDB and LiF resembles that of electrolyte alone; the cyclic voltammogram of electrolyte with only BDB is different as explained above.

3.6 Fundamental Mechanistic Studies on the Reduction of Oxidized Redox Shuttle Molecules at Carbon Anodes

A central fundamental question concerning the function of redox shuttles is the mechanism by which oxidized redox shuttle molecules are reduced at the anode during overcharge [4]. The anode is supposed to be electrically insulating due to the presence of the solid electrolyte interphase (SEI) layer and this would seemingly prevent the reduction of oxidized redox shuttle molecules. It is possible that an SEI layer formed in the presence of a redox shuttle molecule is molecularly imprinted for it and will have enhanced molecular recognition, transport, and electrochemical sensitivity properties toward it. Sensors made by the polymerization or electropolymerization of monomers in the presence of the desired analyte species have enhanced sensitivity toward that particular analyte [5]. The SEI layer formed in the absence of the redox shuttle molecule will not be molecularly imprinted for it, although it may show some kinetically favorable properties due to the possible molecular imprinting of other similar species present during SEI formation such as solvent molecules or solvated Li ions. Molecular imprinting of the SEI layer by the redox shuttle molecule may facilitate the reduction of the oxidized redox shuttle species, even though the SEI layer is electrically insulating.

Molecular imprinting was discovered in 1931 by M.V. Polyakov [5]. Sodium silicate was polymerized in the presence of additives; after drying and extensive washing, the silica had a higher capacity for the adsorption of the chemical that was present during polymerization. Experiments were performed that explained the enhanced adsorption of the molecules in terms of templating, in which cavities with the shape and electrostatic properties of the molecules present during polymerization were formed. Thus, the polymer was imprinted for those molecules compared to other species.

In the 1950s, molecular imprinting was used to prepare silica chromatographic substrates with enhanced selectivity for desired analytes, and it was discovered that chiral selectivity could also be controlled. In the 1970s, the principles of molecular imprinting were applied to organic polymers. Sensors employing various electrochemical detection techniques and selective catalysis are two common uses for molecularly imprinted polymers. No mention in the literature has been found that attributes the ease with which oxidized redox shuttle molecules are reduced at carbon anodes in lithium ion cells to molecular imprinting.

Lithium iron phosphate (LFP) – graphite full cells with a capacity of 34 mAh were formed in the presence or absence of 0.1 M 2,5-di-tert-butyl-1,4-dimethoxybenzene (DDB) in a 30% EC, 70% DEC, 1.2 M $LiPF_6$ electrolyte. DDB is a well characterized redox shuttle molecule with an E^0 of about 3.95V [2]. Figure 39 shows the electrochemical impedance spectroscopic (EIS) results for cells that are formed with electrolyte only (dotted line) versus electrolyte with the addition of DDB (solid line). This indicates that the SEI layer formed in the presence of DDB is different than that formed in the absence of DDB.

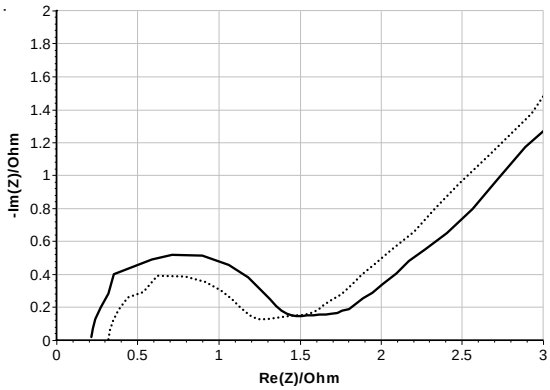

Figure 39. EIS of LFP - graphite pouch cells formed in the absence or presence of DDB

After formation, an equal volume of 0.2 M DDB in electrolyte was added to the cells that were formed in the absence of DDB, so that the concentration of DDB in both sets of cells was 0.1 M. The cells were then subjected to 100% overcharge conditions at a 0.2 C rate. Figure 40 shows the voltage vs. capacity profiles for cells from each formation condition with the absence of DDB (dotted lines) or presence of DDB (solid lines). All cells successfully avoided overcharge, but the cells formed in the absence of DDB operate at a higher voltage than the cells formed in the presence of DDB. More facile electron transfer in the cells formed in the presence of DDB may be an indication that molecular imprinting occurred during formation.

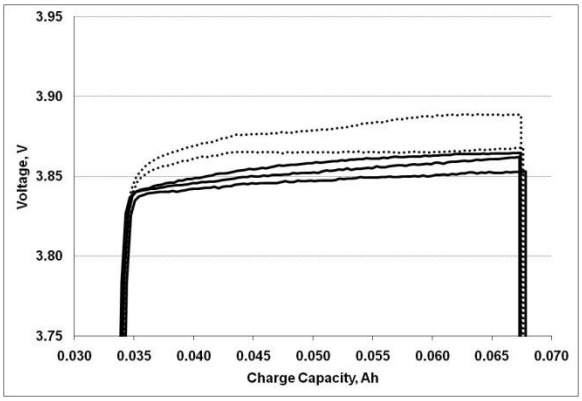

Figure 40. Profile for overcharged LFP – graphite pouch cells with or without 0.1 M DDB.

Further experiments were performed to support or reject the involvement of molecular imprinting in the reduction of oxidized redox shuttle molecules at carbonaceous anode surfaces and are presented later in this Technical Report.

3.7 Redox Shuttle ANL-RS2

A redox shuttle, 1,4-bis(2-methoxyethoxy)-2,5-di-*tert*-butyl-benzene (ANL-RS2), was provided by Argonne National Lab. Cyclic voltammetry (CV) was run on a 1.2 M $LiPF_6$ in 25/5/70 EC/PC/EMC solution with 0.01 M of ANL-RS2 added as the redox shuttle additive. A three electrode electrochemical cell consisting of a platinum working electrode and lithium metal counter and reference electrodes was employed. Cyclic voltammograms are shown below and the redox shuttle has a 3.96 V reduction-oxidation potential. This potential is too low to be used with "4 V cathodes" but may be used with lithium iron phosphate (LFP). It also has a E_{ox}-E_{red} = ΔE = 80 mV which is higher than expected for a fully reversible system (60m V) although this value may be higher due to uncompensated solution resistance in the experiment rather than poor reversibility.

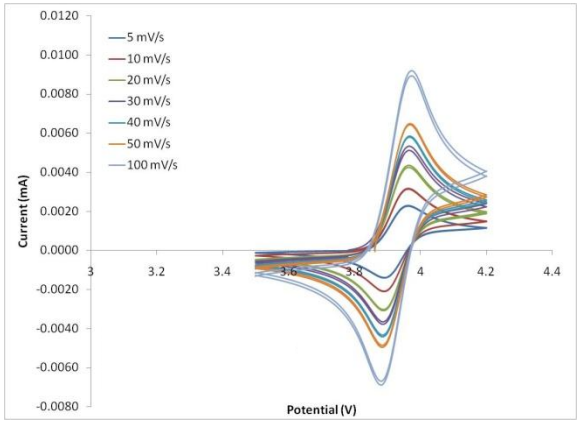

Figure 41. CV at varying rates to determine the oxidation potential and diffusion coefficient.

The diffusion coefficient of ANL-RS2 was determined using the Randles-Sevcik equation and the cyclic voltammetry (CV) at different scan rates. The diffusion coefficient was determined to be 1.60×10^{-6} cm^2/s.

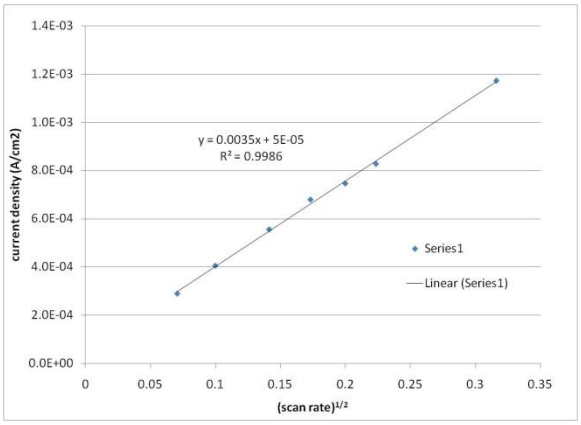

Figure 42. Best fit line to data for diffusion coefficient calculation

3.7.1 Cell Rebalancing

Individual cells (LFP/graphite) were constructed and formed that contained baseline electrolyte and 0.35 M of the ANL-RS2 redox shuttle. Cells with no redox shuttle were also constructed for comparison. After formation, cells were individually precharged to 40 and 80% state-of-charge (SOC). Three pairs of cells, with each pair having a cell at 40 and another at 80% SOC, were connected in series for each cell chemistry. The two-cell series was then charged to 8.4 V or 120% SOC for the least charged cell (160% for the cell with higher SOC), whichever occurred first. Cells with LFP/LTO were also constructed, formed, and rebalanced in a similar manner but different voltages were used to account for the high voltage of the LTO anode. A functioning redox shuttle should rebalance the SOC of the cells since the shuttle will hold the SOC of the cells constant once its redox potential is reached. Following the overcharge or rebalancing cycle, the two-cell series was then cycled twice under normal cycling conditions to evaluate the effectiveness of the cell rebalancing. Auxiliary voltage channels were used to monitor the potential of the individual cells in the series.

The results for the LFP/LTO cells in a two-cell series with the ANL-RS2 redox shuttle before and after cell rebalancing are shown in Figure 43, while Figure 44 shows the results for the LFP/LTO cells without the redox shuttle. Cells with the redox shuttle are effectively rebalanced as evidenced by similar voltage profiles following the overcharge cycle. During the overcharge cycle, two plateaus are observed in the voltage profile of the two-cell series. The first plateau corresponds to the one cell reaching the redox potential of the shuttle while the other cell continues to be charged. The second plateau occurs when both cells have reached the redox potential of the shuttle and it is during this time the cells have reached equal SOC and are rebalanced. Subsequent cycling shows similar voltage profiles between the cells during normal operational conditions demonstrating that the cells have been rebalanced.

LFP/LTO cells in a two-cell series without the shuttle are not rebalanced under the same cycling conditions. In fact, during the cell rebalance cycle, one of the cells reaches a very high voltage (3 V) while the other cell has not even reached 2.1 V that is its normal voltage at full SOC. Having one cell reach such a high voltage (3 V in a LFP/LTO corresponds to a voltage of ~4.6 V vs. Li at the LFP cathode) could present a control problem in larger cells. Subsequent cycles show that the cells are not balanced. During the CV charge, one cell is at about 2.3 V which exceeds the normal operational voltage (i.e. it is overcharged) while the other cell is about 1.9 V and has not been fully charged to 2.1 V. The consequences of continuing to cycle unbalanced cells would lead to decreased battery life since stress is placed on one cell. Extended cycling is likely to continue to further aggravate the situation as the overcharge cell is likely to lose capacity and be overcharged even further on subsequent cycles eventually leading battery failure. Furthermore, the capacity of a battery with cells that are not balanced is reduced

since the voltage of the one cell increases very rapidly while delivering very little capacity over that voltage range thus limiting the SOC reached by the other cell(s).

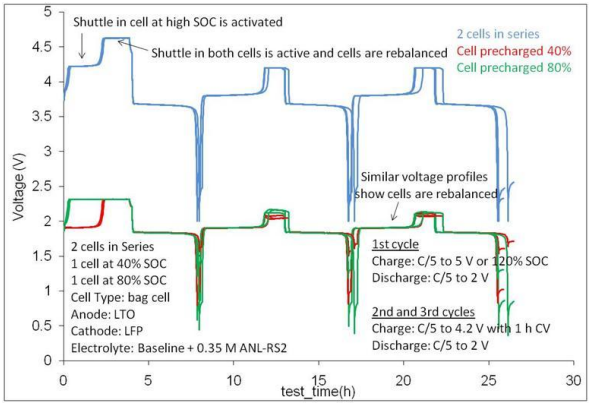

Figure 43. Voltage profile for LFP/LTO two cell series with ANL-RS2 redox shuttle

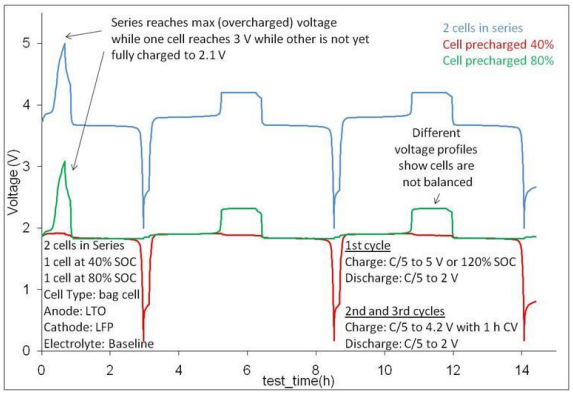

Figure 44. Voltage profile for LFP/LTO two cell series without redox shuttle

The results for the LFP/graphite cells in a two-cell series with the ANL-RS2 redox shuttle are shown in Figure 45. Figure 46 shows the results for the LFP/graphite cells without the redox shuttle. Cells with the redox shuttle are effectively rebalanced as evidenced by similar voltage profiles following the overcharge cycle. During the overcharge cycle, three plateaus are observed in the voltage profile of the two-cell series. The first plateau is during the normal operational voltage of the cell. The second plateau corresponds to the one cell reaching the redox potential of the shuttle while the other cell continues to be charged. The third plateau occurs when both cells have reached the redox potential of the shuttle and it is during this time the cells have reached equal SOC and are rebalanced. Subsequent cycling shows similar voltage profiles between the cells during normal operational conditions demonstrating that the cells have been rebalanced.

The results for the LFP/graphite cells in a two-cell series without the shuttle are not rebalanced under the same cycling conditions and are very similar to the LFP/LTO cells without the redox shuttle. During the cell rebalance cycle, one of the cells reaches a very high voltage (5 V) while the other cell has not even reached 3.65 V that is its normal voltage at full SOC. Subsequent cycles show that the cells are not balanced. During the CV charge, one cell is at about 4 V which exceeds the normal maximum

operational voltage of 3.65 V (i.e. it is overcharged) while the other cell is about 3.4 V. The consequences of having unbalanced LFP/graphite cells will be the same as that of unbalanced LFP/LTO cells and could be worse since the plating of lithium at the graphite anode is more likely.

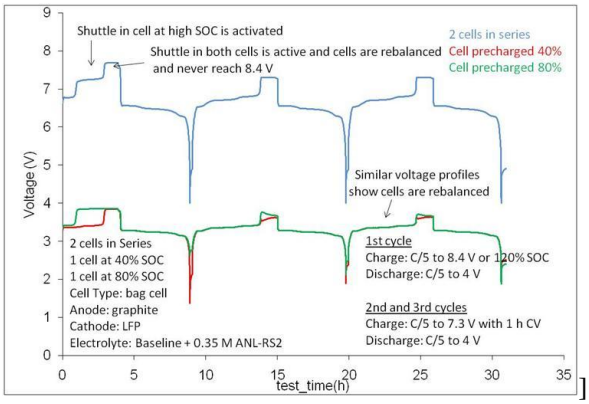

Figure 45. Voltage profile for LFP/graphite two cell series with ANL-RS2 redox shuttle

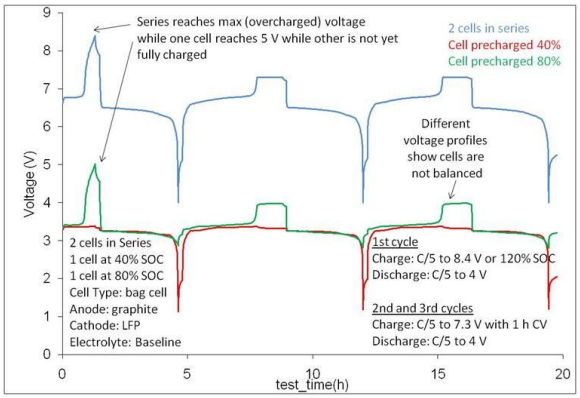

Figure 46. Voltage profile for LFP/graphite two cell series without redox shuttle

3.7.2 Overcharge cycling

The overcharge cycling was conducted with the cells used in the previously described cell rebalancing test. The cells were kept in the series configuration. The batteries (2 cell series) were cycled according to the profiles in Table 7.

Table 7. Cycling profiles for LFP/LTO and LFP/graphite cells

Chemistry	Charge	Overcharge	Discharge
LFP/LTO	1 C to 4.2 V	C/5 to 200% SOC or 5 V	1 C to 2.0 V
LFP/graphite	1 C to 7.3 V	C/5 to 200% or 8.4 V	1 C to 4.0 V

The voltage profile during charging for cycles 1, 25, and 50 for the LFP/LTO and LFP/graphite cells is shown in Figures 47 and 48 respectively. With increased cycling, the capacity delivered during the constant current 1 C cycling decreases significantly. The brief dip in voltage following end of 1 C charging is because of the change from 1 C to C/5 rate and the resulting smaller IR drop and relaxation processes. The LFP/graphite cells lose much more of their 1 C rate charge capacity than do the LFP/LTO

cells. Also, the voltage plateau, while relatively flat during an individual cycle, does increase somewhat with cycling. This indicates that the shuttle is losing its effectiveness.

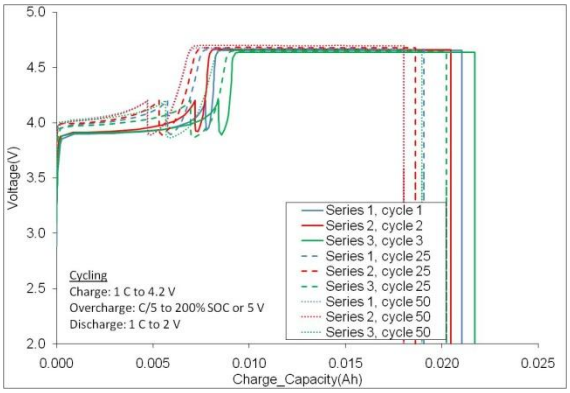

Figure 47. Voltage profile during charge for LFP/LTO cells

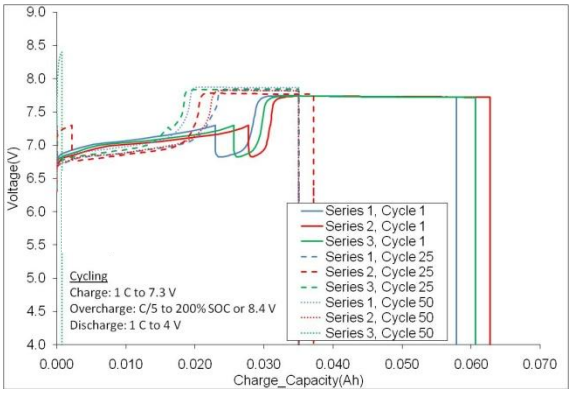

Figure 48. Voltage profile during charge for LFP/graphite cells

The voltage at the end-of-charge was plotted versus cycle life. The plot for LFP/LTO and LFP/graphite cells are shown in Figures 49 and 50, respectively. An increase in the potential indicates that the shuttle is losing its effectiveness. It is clear that the cells with graphite have shorter life than cells with LTO. It is believed that the SEI on the graphite is thicker than on LTO. If the shuttle is reacting with the SEI, it will require that the SEI layer be reformed and consume lithium in the process. Since the lithium content is limited by the cathode, the cycle life is shorter for cells with graphite than LTO. The redox shuttle failed in one set of LFP/graphite cells after about 40 cycles and another had failed after about 80 cycles. Dahn has observed similar behavior with another redox shuttle and LTO and graphitic anodes and attributed the difference to the reaction of the redox shuttle with the SEI [6].

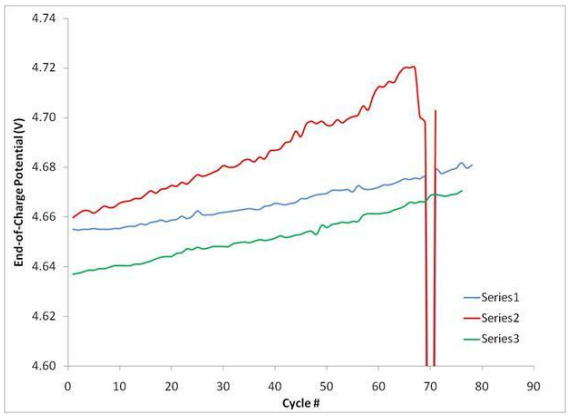

Figure 49. Voltage at the end of charge for LFP/LTO cells

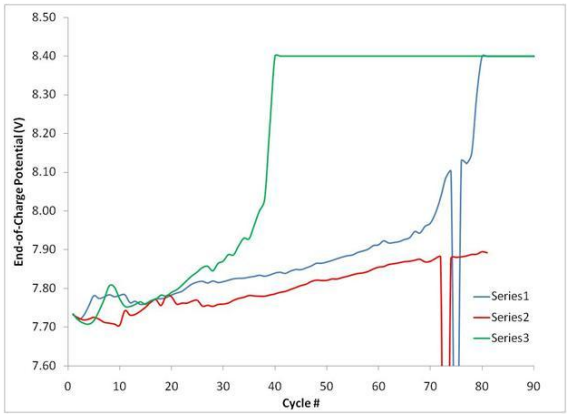

Figure 50. Voltage at the end of charge for LFP/graphite cells

The cycle life of the LFP/LTO and LFP/graphite cells is shown in Figures 51 and 52 respectively. The loss in discharge capacity coincides with the shuttle failure. The decrease in the charge capacity with cycle life is due to the lower capacity during constant current charging.

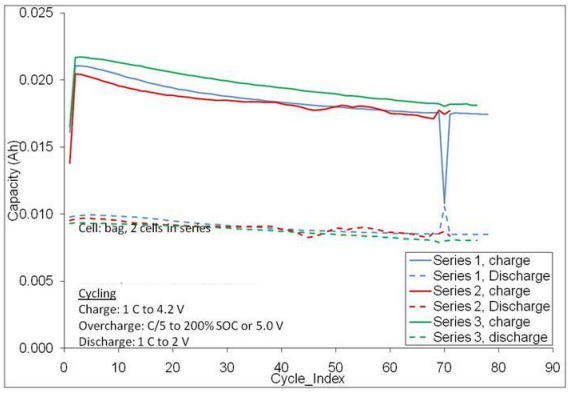

Figure 51. Cycle life of cells with LFP/LTO electrodes

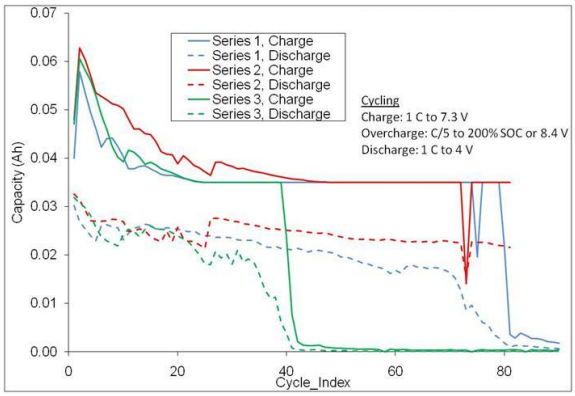

Figure 52. Cycle life of cells with LFP/graphite electrodes

3.7.3 Overcharge cycle life of ANL-RS2 to failure

Further overcharge cycling was conducted with the cells used in the cell rebalancing test. The cells were kept in the series configuration. The batteries (2 cells in series) were cycled according to the profiles in Table 8.

Table 8. Cycling profiles for LFP/LTO and LFP/graphite batteries

Chemistry	Charge	Overcharge	Discharge
LFP/LTO	1 C to 4.2 V	C/5 to 200% SOC or 5V	1 C to 2.0 V
LFP/graphite	1 C to 7.3V	C/5 to 200% or 8.4 V	1 C to 4.0 V

The voltage at the end-of-charge was plotted versus cycle life. The plots for LFP/LTO and LFP/graphite cells are shown in Figures 53 and 54, respectively. An increase in the potential indicates that the shuttle is losing its effectiveness. It is clear that the cells with graphite anodes have shorter life than cells with LTO anodes. The LTO/LFP cells all completed at least 150 cycles before overcharge protection failed and one of the cells had overcharge protection for over 350 cycles. The redox shuttle failed in one set of LFP/graphite cells after about 40 cycles and others had failed after about 80 and 110 cycles. Dahn has observed similar behavior with another redox shuttle and LTO and graphitic anodes and attributed the difference to the reaction of the redox shuttle with the SEI [6]. It is believed that the SEI on the graphite is thicker than on LTO. If the shuttle is reacting with the SEI, it will require that the SEI layer be reformed and consume lithium in the process. Because the lithium content is limited by the cathode, the cycle life is shorter for cells with graphite than LTO during overcharge in the presence of a redox shuttle.

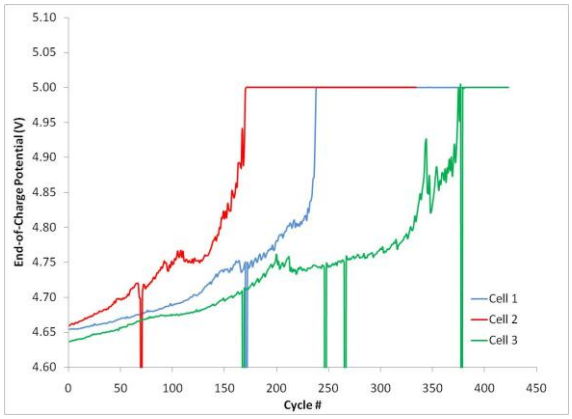

Figure 53. Voltage at the end of charge for LFP/LTO cells

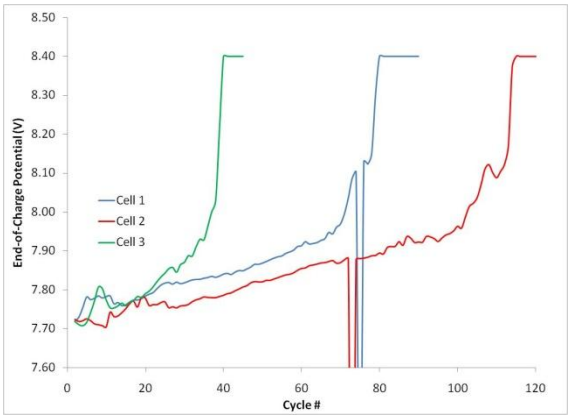

Figure 54. Voltage at the end of charge for LFP/graphite cells

The cycle life of the LFP/LTO and LFP/graphite cells is shown in Figures 55 and 56 respectively. The loss in discharge capacity coincides with the shuttle failure. The decrease in the charge capacity with cycle life is due to the lower capacity during constant current charging.

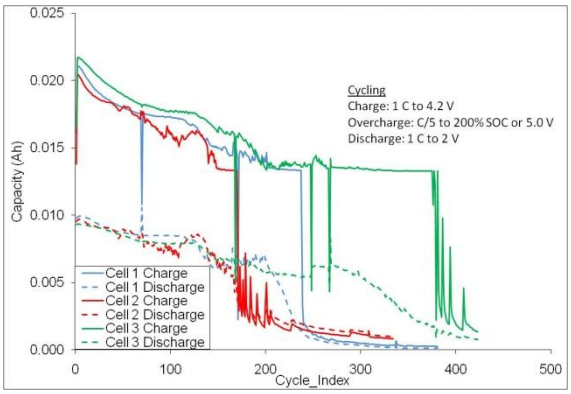

Figure 55. Cycle life of cells with LFP/LTO electrodes

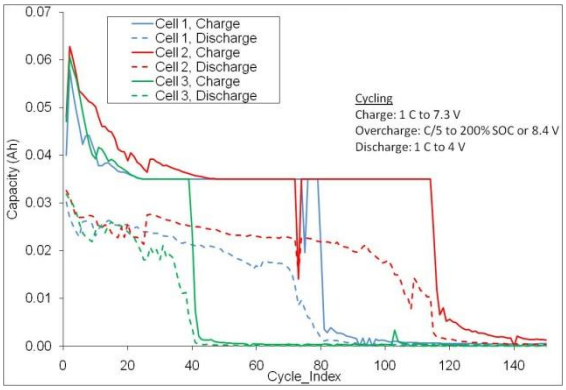

Figure 56. Cycle life of cells with LFP/graphite electrodes

The ANL-RS2 shuttle has been shown to be an effective redox shuttle with cells having LFP cathodes. This shuttle has longer overcharge life when used in combination with LTO anodes than graphitic anodes presumably because of a reaction with the SEI layer on the graphite anode. The combination of LiBOB, a known contributor to the SEI layer, negatively impacted overcharge protection when used in combination with the ANL-RS2 shuttle. The commercial electrolyte with a redox shuttle that was shown to provide overcharge protection for NMC cathodes has twice the overcharge cycle life and lower overcharge voltage when LiBOB is added to the electrolyte of cells with hard carbon anodes and NMC cathodes.

3.7.4 ANL-RS2 Redox Shuttle with LiBOB

Because the redox shuttle may be reacting with the SEI layer and limiting the overcharge cycle life, LiBOB (lithium bisoxalatoborate) was used as an additive in combination with the redox shuttle additive. LiBOB is a lithium salt that has been used as an SEI layer additive to improve the cycle life under at elevated temperatures. It is also highly oxygenated and its reduction products that form part of the SEI on the anode surface might be less susceptible to oxidation (because of the highly electronegative oxygen atoms) compared to the SEI formed from traditional electrolytes containing only organic carbonates and $LiPF_6$ salt and therefore have better resistance to being oxidized by the oxidized form of the redox shuttle.

Figure 57 shows the effect that the presence of 2 wt% LiBOB has on the overcharge life of graphite/LFP cells with the ANL-RS2 redox shuttle. Cells without LiBOB are shown for comparison. The cells were charged to 100% SOC at the 1 C rate and then overcharged continuously at the C/5 rate until the shuttle failed or 2000% SOC was reached. The data in Figure 57 shows that the cells with the LiBOB do not have a stable voltage plateau and reach a higher voltage and the shuttle fails much earlier than cells without LiBOB. Clearly, the presence of LiBOB does not improve overcharge performance in these cells. However, the fact that the LiBOB does have an impact on overcharge performance suggests that the SEI layer has a role in the overcharge cycle life.

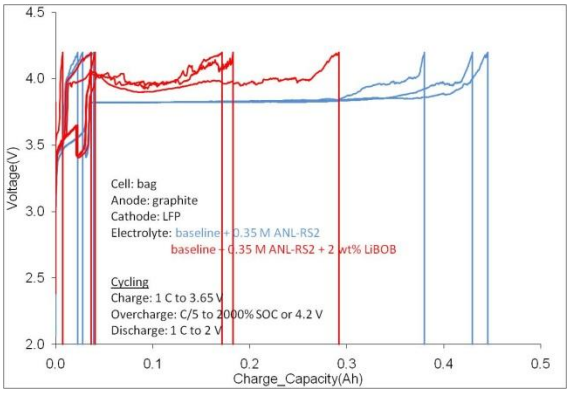

Figure 57. Overcharge of graphite/LFP cells with ANL-RS2 with and without LiBOB additive.

3.8 Commercial Electrolyte with Redox Shuttle

A commercially available electrolyte from Showa Denko that contains a redox shuttle compound has been tested. This electrolyte is being tested for calendar life, cycle life and for its ability to protect against overcharge. The electrolyte contains 0.4 M $Li_2B_{12}F_{12}$, 0.1 M $LiPF_6$, and an undisclosed additive. The source of the overcharge protection is the $Li_2B_{12}F_{12}$ salt which has been previously reported [1] and was described earlier in this report, but without the additive and at 1.0 M $LiPF_6$ and 0.1 M $Li_2B_{12}F_{12}$ concentrations.

The commercial redox shuttle electrolyte has similar or better formation characteristics in an NMC-hard carbon full cell than the baseline electrolyte, Figure 58. The first cycle has higher charge and discharge capacity and the Coulombic efficiency is a little higher than the baseline electrolyte. The voltage profile also looks different in the early portion of the cycling (~2.5 V).

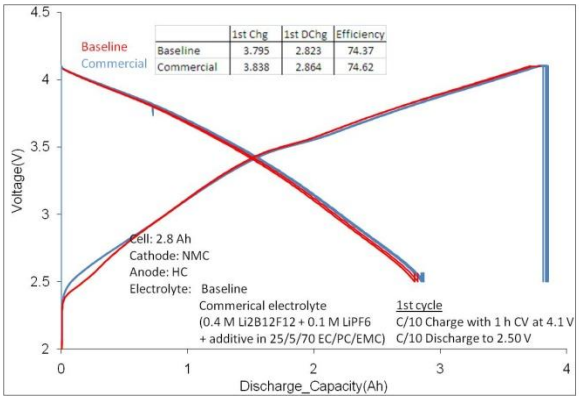

Figure 58. First cycle of the commercial redox shuttle electrolyte

Calendar and cycle life testing in 2.8 Ah cells is shown in Figures 59 and 60 respectively. The calendar life at 4.1 V (100% state-of-charge) at 55 °C is improved over that of the baseline electrolyte but there does not appear to be a significant difference between the commercial electrolyte and the baseline electrolyte during cycle life at the 2 C rate between 4.1-2.5 V (100% depth-of-discharge) testing at 45 °C.

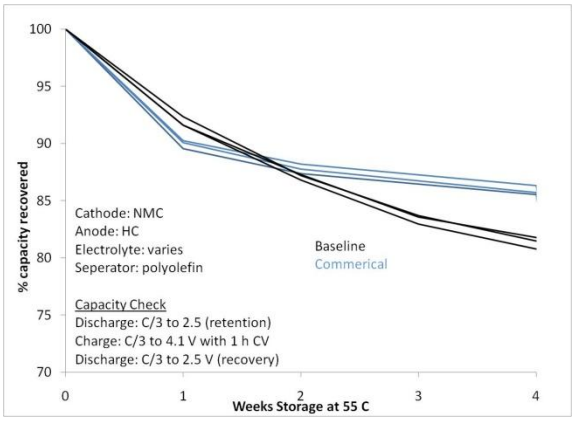

Figure 59. Calendar life testing of commercial redox shuttle electrolyte at 55 °C

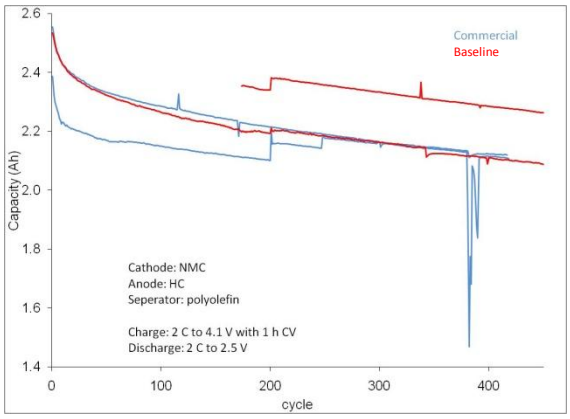

Figure 60. Cycle life testing of commercial redox shuttle electrolyte at 45 °C

Overcharge testing of the commercial redox shuttle electrolyte was also performed in pouch cells with hard carbon anodes and NMC cathodes. The cells were cycled according the profile in Table 9. Baseline cells with standard $LiPF_6$ based electrolyte with no redox shuttle were cycled as well as cells with 1 wt% LiBOB added to the commercial redox shuttle electrolyte.

Table 9. Overcharge cycling profile for cells with commercial redox shuttle electrolyte

Chemistry	Charge	Overcharge	Discharge
HC/NMC	1 C to 4.1 V	200% SOC or 4.9 V	1 C to 2.5 V

The overcharge cycle life is shown in Figure 61. The cells with the commercial redox shuttle electrolyte (red lines) performed the worst in terms of cycle life but did provide some overcharge protection for about 40 cycles before they completely failed. The cells with the baseline electrolyte (blue lines) had the best cycle life but had no overcharge protection. The cells with 1 wt% LiBOB (green lines) added to the commercial redox shuttle electrolyte had about twice the overcharge cycle life. These cells also had a lower end-of-charge voltage that was more stable than the cells with only the commercial electrolyte as Figure 62 shows. In this instance, it appears that LiBOB improves the stability of the cells presumably through affecting the SEI layer of the anode. The baseline cells had a longer cycle life despite

being overcharged to a greater extent presumably for at least three reasons related to the absence of the redox shuttle: less time spent at overcharge, no reaction between the oxidized form of the redox shuttle and the SEI layer, and no heat generation that occurs during the process of current shuttling.

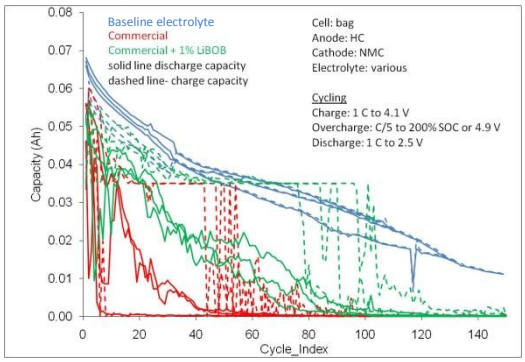

Figure 61. Overcharge cycle life of hard carbon/NMC cells with various electrolytes

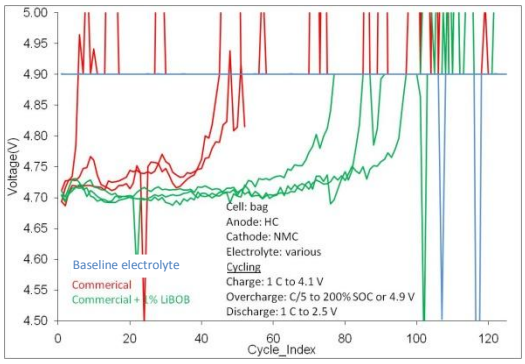

Figure 62. End-of-charge voltage for hard carbon/NMC cells with various electrolytes

3.9 Stability of BDB and DDB towards hydrolysis and methanolysis

The stability of two redox shuttle molecules, namely BDB (2-(pentafluorophenyl)-tetrafluoro-1,3,2-benzodioxaborole) and DDB (2,5-di-tert-butyl-1,4-dimethoxybenzene), in the presence of water or methanol was examined using gas chromatography-mass spectrometry (GC-MS). BDB was obtained from Argonne National Laboratory, while DDB was obtained from 3M. Two batches of BDB were tested; one batch was purified using recrystallization, while the other was purified using sublimation. The BDB samples were synthesized from extremely pure tetrafluorocatechol (TFC).

The two types of BDB were dissolved in acetonitrile at a concentration of about 2 mg/ml and injected into the GC-MS (Agilent, 7890A gas chromatograph with 5975C mass spectrometer). The chromatograms both displayed a main peak at 15.24 minutes which corresponded to the BDB. The mass spectrum of the BDB is in Figure 63 below.

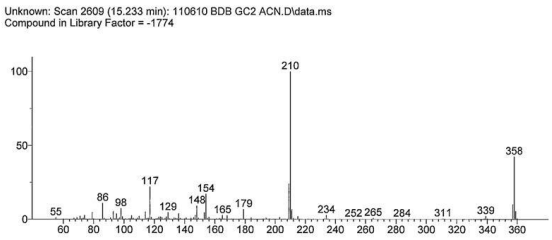

Figure 63. The 70 eV EI mass spectrum of BDB

The precursor ion is at 358 m/z, which is the molecular weight of BDB (z=1). The most abundant ion is at 210 m/z, which corresponds to the fragment on the right side of the molecule depicted in Figure 64. The C-O bonds are weaker than the B-O or B-C bonds, so that is where the molecule mainly fragments. (The average bond energy for B-O is about 808 kJ/mole, for B-C is about 448 kJ/mole, and for C-O Is about 358 kJ/mole.)

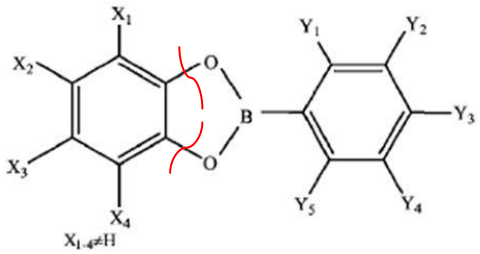

Figure 64. Fragmentation of BDB in the mass spectrometer

In both chromatograms, an impurity with retention time 15.24 minutes exists with an abundance of a few percent. The impurity was identified from its mass spectrum as $C_{12}F_8HBO_2$ and is the BDB molecule with one of the fluorine atoms substituted with a hydrogen atom (H-BDB). Its fragmentation pattern mimics that of BDB, and the hydrogen atom is not present on the TFC portion of the molecule. The mass spectrum of the impurity is shown in Figure 65. Many of the peaks in the mass spectrum originate from the BDB, such as those at 358 and 210 m/z since the small H-BDB peak elutes closely to the large BDB peak. The peaks at m/z 340 and 192 are due to the H-BDB impurity.

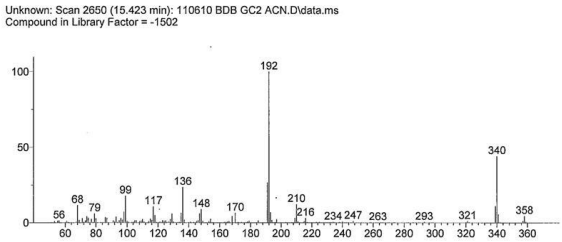

Figure 65. Mass spectrum of H-BDB

The recrystallized BDB had an observable peak at 11.49 minutes retention time, corresponding to TFC, but the sublimed BDB had a much smaller peak at 11.49 minutes retention time. Sublimation eliminated almost all of the TFC impurity, but since the BDB and the H-BDB impurity have such similar molecular structures and properties, sublimation did not reduce the amount of H-BDB impurity compared to the recrystallized BDB. It should be noted that the hydrogen atom impurity is not on the TFC side of the molecule. Very pure TFC was used in the synthesis of this lot of BDB. The hydrogen atom impurity originates from the boronic acid side of the molecule.

Next, about 10% water was added to the solutions of BDB in acetonitrile and the samples were immediately run on the GC-MS. In both the recrystallized and sublimed samples, the chromatograms displayed a major peak at 11.48 minutes retention time, and the mass spectrum at this retention time corresponds to TFC. The BDB hydrolyzed back to its starting materials, namely TFC and pentafluorophenyl boronic acid. Hydrolysis of the BDB molecule apparently occurs quite quickly and the starting materials are regenerated in the process. The pentafluorophenyl boronic acid was not observed in the chromatogram.

Another experiment was run in which the recrystallized and sublimed BDB samples were dissolved in methanol and injected immediately into the GC-MS. The chromatograms of both the crystallized and sublimed materials displayed a major peak for TFC. The BDB reacted very quickly with the methanol (methanolysis) to form TFC and presumably the dimethoxy derivative of the pentafluorophenyl boronic acid. The BDB is not stable in the presence of methanol or water. The purity of the product did not alter the reaction on the time scale studied (minutes).

Solutions of DDB were prepared using acetonitrile and methanol. Both chromatograms show one major peak at 16.67 minutes retention time and a nearly perfect library match to 2,5-di-tert-butyl-1,4-dimethoxybenzene. DDB has no bonds that are easily cleaved by reaction with hydroxyl containing species such as methanol or water and so it is stable in those solutions. DDB is more stable chemically than BDB.

The redox shuttle molecule BDB is not stable in the presence of water or methanol; it undergoes hydrolysis to regenerate the starting materials, or methanolysis to form TFC and presumably dimethoxy pentafluorophenyl boronic acid. This means that the BDB does not possess enough stability to be used as a redox shuttle in cells when long-term cycle life or calendar life is desired, since any water or alcohol that is present in the electrolyte or enters the packaging after sealing immediately reacts with the BDB to form compounds which are not redox shuttles.

.

3.10 Molecular imprinting: Does it play a role in the reduction of oxidized redox shuttle species?

Redox shuttle molecules prevent the overcharge of cells electrochemically. An effective redox shuttle species should have an oxidation potential about 0.2 to 0.3 V above the maximum desired cathode potential during normal operation. If the cell enters an overcharged state, the redox shuttle consumes charge when its oxidation potential is reached. It is oxidized at the cathode, and then diffuses to the anode, where it is reduced. This cycle can be repeated indefinitely for a species with chemically and electrochemically stable oxidized and reduced forms [7].

The solid electrolyte interphase (SEI) layer is formed during the first charging cycle of a lithium ion cell employing typical ethylene carbonate (EC) or propylene carbonate (PC) based electrolytes when the potential of the anode decreases below about 0.7 V vs. Li^+/Li. The SEI layer is formed from reduction products of the electrolyte solvent(s), salt(s), and additive(s) [8]. It is complex, having both inorganic and organic domains, and is a dynamic entity. It conducts Li^+ but is electrically insulating, and should prevent further reaction with the electrolyte during subsequent charge/discharge cycles. A good SEI layer is essential for the long life of a lithium ion battery employing a carbonaceous anode.

The contradiction is that the SEI layer is electrically insulating, yet is able to reduce the oxidized form of a redox shuttle species. A central fundamental question concerning the function of redox shuttle species is the mechanism by which oxidized redox shuttle molecules are reduced at the anode [4]. After formation, the anode is supposed to be passivated by the SEI layer and prevent further reduction of the electrolyte, which would also seemingly prevent the reduction of oxidized redox shuttle species. It is possible that an SEI layer formed in the presence of a redox shuttle molecule is molecularly imprinted for it and will have enhanced molecular recognition, transport, and electrochemical sensitivity towards it. Sensors fabricated by the polymerization or electropolymerization of monomers in the presence of the

desired template analyte species have enhanced sensitivity toward that particular analyte [5]. An SEI layer formed in the absence of the redox shuttle species will not be molecularly imprinted for it, although it may show some kinetically favorable properties due to the possible molecular imprinting of other similar species present during SEI formation such as solvent molecules or solvated Li^+. Molecular imprinting of the SEI layer by the redox shuttle molecule may facilitate the reduction of the oxidized redox shuttle species, even though the SEI layer is electrically insulating. It may allow the oxidized redox shuttle species to arrive at the conductive electrode surface, or close enough to the electrically conducting surface of the electrode for electron tunneling to occur [4, 9].

Molecular imprinting was discovered in the 1930s by Polykaov [5]. Template additives such as benzene were added to sodium silicate as it condensed from ammonium carbonate solutions of water. After drying and copious hot water washing, the resulting silica was found to have higher adsorption uptake for the template molecule over structurally similar molecules. The selectivity was explained as resulting from structural changes in the silica that reflected the nature of the additive. Later, it was determined that sites, or cavities, created during polycondensation or polymerization have steric (size and shape) and electrostatic recognition for the template molecule. Today, molecular imprinting is used in areas such as sensors, chromatography, synthesis, catalysis, and pseudoimmunoassays. Sensor technologies are of particular relevance, and molecular imprinting has been employed in quartz crystal microbalance, fluorescence, surface plasmon, and electrochemical studies. Electrochemical sensors based on conductivity, capacitance, potentiometry, and amperometric techniques such as square wave voltammetry have been shown to provide sensitivity and selectivity toward the template species over structurally similar molecules, even to the extent that enantiomers can be distinguished.

SEI layers formed on carbon anodes during the first cycle of formation of a lithium ion cell have many important attributes in common with molecularly imprinted films. Both are formed from monomers that are condensed or polymerized; chemical or electrochemical polymerization is employed in molecularly imprinted films, and SEI layers are formed in-situ electrochemically. The thickness of both films is on the order of tens to hundreds of nanometers. Template species are present during the formation of both of the layers; for molecularly imprinted films, the template species are intentionally added analyte molecules, and for SEI layers, the template species are all of the electrolyte components such as solvent(s), salt(s), and additive(s). Solvated Li^+ is a particularly important template species that is present during SEI formation. It is important to note that molecular imprinting results in preferential uptake of species present during SEI layer formation but will allow different molecules to use the cavities if they "fit."

Electrochemical and lithium ion cell experiments have been run to evaluate this hypothesis. The apparent diffusion coefficient of ferrocene was determined at a pristine glassy carbon electrode, a glassy carbon electrode with an SEI layer formed in the absence of ferrocene, and a glassy carbon electrode with an SEI layer formed in the presence of ferrocene. Lithium ion cells using lithium iron phosphate (LFP) cathodes and graphite anodes were formed in the presence or absence of a redox shuttle molecule, namely 2,5,-di-tert-1,4-dimethoxybenzene (DDB) [8]. Electrochemical impedance spectroscopy (EIS) was performed after formation. After addition of electrolyte so that all cells contained 75 mM DDB, the cell voltage during overcharge was monitored. The capacity that could be recovered after an overcharge at different C-rates was also measured.

3.10.1 Experimental

Cyclic voltammetry (CV) was performed using a three electrode electrochemical cell (Princeton Applied Research RDE0018) consisting of a glassy carbon working electrode (Pine AFE3T050GC), a platinum wire counter electrode, and a lithium reference electrode controlled by a Solartron SI 1287 Electrochemical Interface, SI 1255 HF High Frequency Analyzer, and SI 1260 Impedance/Gain Phase

Analyzer, with CorrWare software (Scribner Associates, Inc., Southern Pines, NC). The electrochemical instrumentation is located in a dry room with dew point -60°F to -110°F. The electrolyte composition was 1.2 M $LiPF_6$ dissolved in 3:7 ethylene carbonate (EC):diethyl carbonate (DEC). Cyclic voltammograms of 1 mM ferrocene (Sigma-Aldrich) in electrolyte were run at scan rates of 5, 10, 20, 30, 50, and 100 mV/sec. The electrode surface was pristine for the first set of cyclic voltammograms at various scan rates. After cleaning the electrode surface by polishing and rinsing, an SEI layer was formed on the glassy carbon electrode surface for the second determination of the ferrocene diffusion coefficient potentiostatically by holding at 0.6 V for 20 seconds in electrolyte. An aliquot of ferrocene in electrolyte was added to the electrochemical cell for a concentration of 1 mM, and cyclic voltammetry was run at the various scan rates. Finally, an SEI layer was formed on the glassy carbon electrode surface by holding at 0.6V for 20 seconds in a solution of 1 mM ferrocene in electrolyte, and cyclic voltammetry at the various scan rates was performed. Finally, the diffusion coefficient or apparent diffusion coefficient was calculated for the three experimental runs using the Randles-Sevcik equation. All voltages listed are versus Li/Li^+.

Cell Fabrication and Testing

Cell experiments were performed using EnerDel standard R&D pouch cells with approximately 35 mAh capacity for the lithium iron phosphate – graphite chemistry that was employed. Cells were fabricated using standard EnerDel R&D procedures and activated with one of four electrolytes (Table 10). After formation using an Arbin BT2000 (Table 11), the cells were subjected to EIS testing using the Solartron instrumentation described above with ZPlot and Zview software (Scribner Associates, Southern Pines, NC). They were then opened in the dry room and an equal volume of one of three electrolytes was added (Table 10) so that all cells contained 75 mM DDB. After vacuum resealing, the cells were subjected to overcharge at different C-rates (Table 11). All voltages listed are versus Li/Li^+.

Table 10. Electrolytes employed in LFP-graphite cell experiments. The standard electrolyte is 1.2 M $LiPF_6$ in 3:7 EC:DEC. VC = vinylene carbonate.

Group	Electrolyte present during formation	Electrolyte added after formation
1	standard	standard + 150 mM DDB
2	standard + 75 mM DDB	standard + 75 mM DDB
3	standard + 75 mM DDB + 1.65% VC	standard + 75 mM DDB
4	standard + 150 mM DDB	standard

Table 11. Formation and overcharge cycling schedules for LFP-graphite cells

Formation	Charge at 0.1C to 3.7V; rest 10 minutes; discharge at 0.2C to 2.5V
Overcharge cycles	Charge at 1C to 3.7V; rest 10 minutes; overcharge at 0.1, 0.2, or 0.5 C to 4.2V or 200% capacity; rest 10 minutes; discharge at 1C to 2.5V

3.10.2 Results and Discussion

Electrochemistry

Ferrocene is a model redox shuttle compound [10]. The 3.25 V potential of the ferrocene-ferrocenium couple is too low for practical use in lithium ion cells, but the chemical stability and electrochemical reversibility of ferrocene and ferrocenium make it a good compound to use in electrochemical studies. The diffusion coefficient of ferrocene in standard electrolyte was determined using a glassy carbon electrode with three different surface states: pristine, with an SEI layer formed in the absence of the ferrocene, and with an SEI layer formed in the presence of ferrocene.

The cyclic voltammograms and Randle-Sevcik plot for ferrocene at the pristine glassy carbon electrode are shown in Figure 66. The diffusion coefficient for ferrocene in the standard electrolyte is 2.09×10^{-6} cm^2/sec. This value agrees well with a literature value for ferrocene in electrolyte [10].

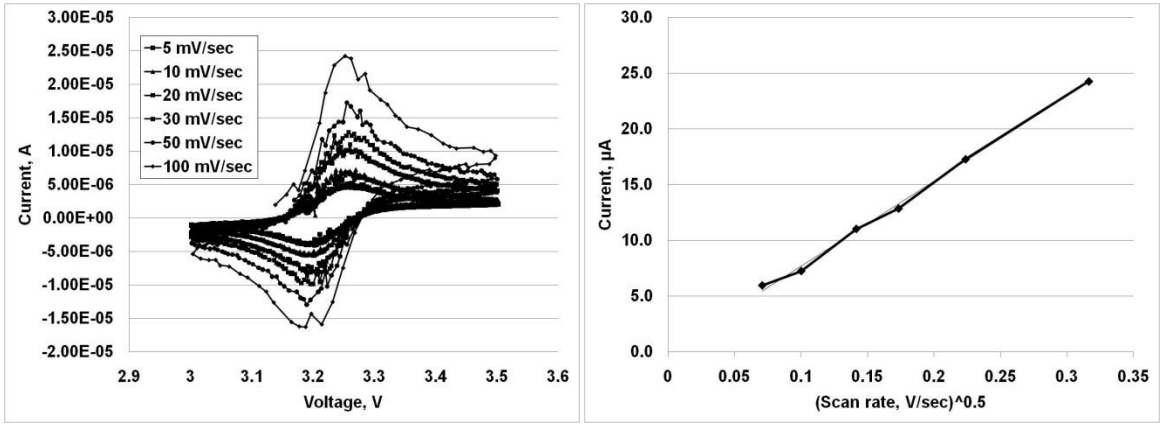

Figure 66. Top: CVs of ferrocene at a glassy carbon electrode in standard electrolyte (1.2 M $LiPF_6$ in 3:7 EC:DEC) at various scan rates. Bottom: Randle-Sevcik plot for determination of diffusion coefficient.

Next, an SEI layer was formed on the surface of the glassy carbon electrode by holding the potential at 0.6 V for 20 seconds and the apparent diffusion coefficient was determined. In one trial, the SEI layer was formed in the standard electrolyte, and in the next trial, the SEI layer was formed in standard electrolyte with 1 mM ferrocene. Figure 67 shows the plot of current versus time for the SEI layer formation on the glassy carbon electrode surface; no significant difference was observed for the two conditions.

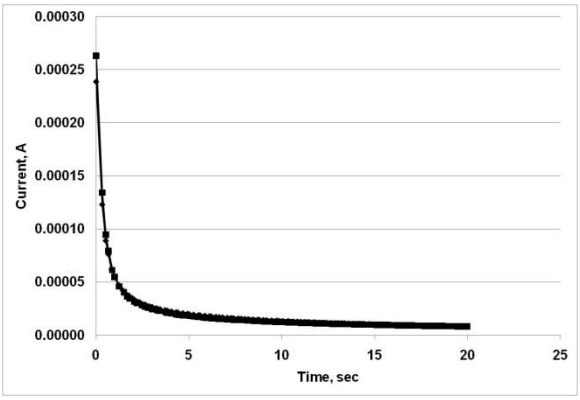

Figure 67. Plot of current vs. time for glassy carbon electrode in standard electrolyte at 0.6 V. Square points: standard electrolyte. Diamond points: standard electrolyte plus 1 mM ferrocene.

Cyclic voltammograms at various scan rates were run for the glassy carbon electrode with an SEI layer formed in the absence and in the presence of ferrocene. Randle-Sevcik plots were constructed, and apparent diffusion coefficients were calculated. The results are presented in Table 12.

Table 12. Apparent diffusion coefficients for ferrocene at a glassy carbon electrode in standard electrolyte (1.2 M $LiPF_6$ in 3:7 EC:DEC) and 1 mM ferrocene

Preparation of glassy carbon electrode	Apparent Diffusion Coefficient, cm^2/sec
Pristine	2.09×10^{-6}
SEI layer formed in the presence of Fc	1.31×10^{-6}
SEI layer formed in the absence of Fc	6.14×10^{-7}

The apparent diffusion coefficient for ferrocene is smaller for the glassy carbon electrode with an SEI layer formed on the surface than for a pristine surface. This is expected, since there are impedances associated with the SEI layer. The apparent diffusion coefficient for ferrocene when the SEI layer was formed in the presence of ferrocene is roughly double when compared to the SEI layer being formed in the absence of ferrocene. Enhanced transport of ferrocene through the SEI layer due to a molecular imprinting effect would explain the difference in apparent diffusion constants. Cavities in the SEI layer that are molecularly imprinted specifically for ferrocene would aid the transport kinetics of the ferrocene to the electrode surface.

The cavities formed by the various species that are present during the formation of the SEI layer can be thought of as functional porosity at a molecular level. This agrees with the solvent diffusion model for aging of lithium ion battery cells in which the SEI layer has both large scale and small scale porosity [11].

Cells

First cycle formation results for one representative cell from each group of LFP-graphite cells are presented in Figure 68. There were no discernible differences in the initial, reversible, or irreversible capacities in the four groups of cells. The redox shuttle molecule DDB is not active at the maximum

cathode voltage of approximately 3.7 V, so it does not affect the cell capacity. The different electrolytes tested the effect of DDB being present or absent during formation, the effect of the concentration of DDB during formation, and the effect of vinylene carbonate (VC), a well-known crosslinking agent that can improve the SEI layer of lithium ion cells [12].

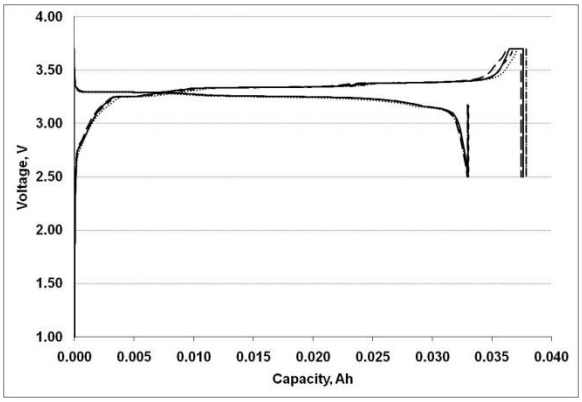

Figure 68. First cycle formation for LFP-graphite pouch cells. Solid line: standard electrolyte. Dashed line: standard electrolyte plus 75 mM DDB. Dotted line: standard electrolyte plus 75 mM DDB and 1.65% VC. Long dashed line: standard electrolyte plus 150 mM DDB.

After formation, EIS was performed on the cells at 0% SOC and the results are presented in Figures 69 and 70. The EIS spectra clearly show that the impedance of the LFP-graphite full cell is affected by the presence and concentration of the DDB. Previous experiments performed at EnerDel have shown that the impedance of both LFP and graphite half cells increases when a redox shuttle molecule is present (unpublished data). This implies that the redox shuttle molecule is indeed incorporated into the SEI layer during formation. Further experiments are required to separate the contributions from the anode and cathode to the EIS spectrum, but the following discussion assumes that the SEI layer on the anode is most affected by the presence of the DDB. The first semicircle in the EIS spectrum is generally agreed upon to be the SEI layer resistance (R_{SEI}), while the second semicircle represents either a charge transfer resistance or a desolvation resistance, or both (R_{CT} or R_{DESOLV}) [13]. The R_{SEI} increased with increasing DDB concentration, while the R_{CT} or R_{DESOLV} remained roughly constant. Since the DDB cannot likely successfully compete with EC to chelate lithium ions, the presence of DDB in the SEI layer increases the R_{SEI}. Since the DDB should not interfere with the desolvation of Li^+ and the associated charge transfer, the R_{CT} or R_{DESOLV} does not appear to be affected by the presence of DDB. VC should increase the amount of polymerized compared to polycondensed species in the SEI layer. The presence of VC during formation decreases the R_{SEI}, likely due to forming a thinner SEI layer [12] and increases the R_{CT} or R_{DESOLV}, perhaps due to interference with the desolvation process.

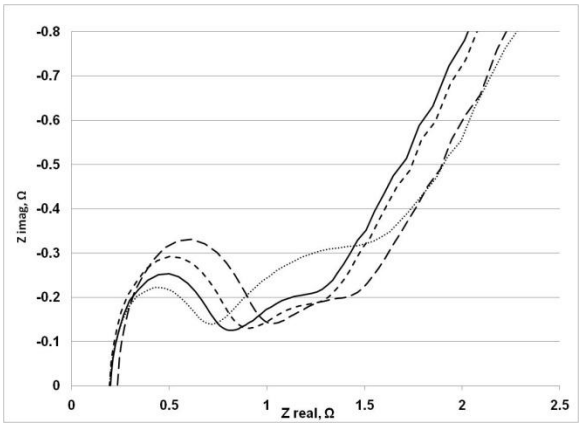

Figure 69. Electrochemical impedance spectra for LFP-graphite pouch cells after formation at 0% state of charge. Solid line: standard electrolyte. Dashed line: standard electrolyte plus 75 mM DDB. Dotted line: standard electrolyte plus 75 mM DDB and 1.65% VC. Long dashed line: standard electrolyte plus 150 mM DDB.

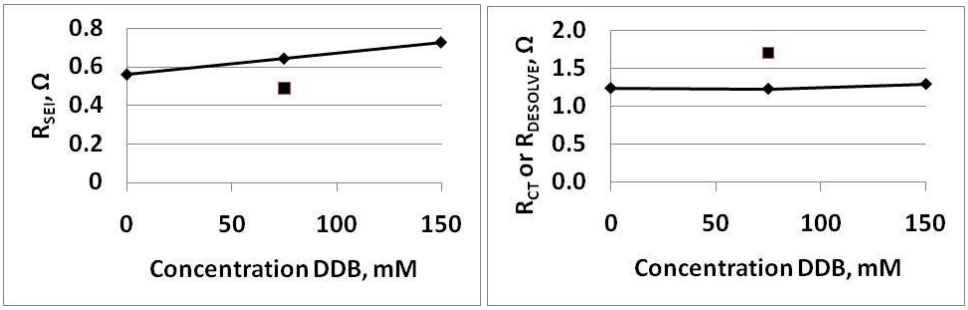

Figure 70. R_{SEI} and R_{CT} or $R_{DESOLVE}$ as a function of DDB concentration during formation for LFP-graphite pouch cells at 0% state of charge. Diamond-shaped data points are for electrolyte with DDB; square-shaped data point is for electrolyte with DDB and VC.

After addition of the second electrolyte, the cell voltages were monitored during a 0.1C overcharge and the results are shown in Figure 71. All cells contain 75 mM DDB as a redox shuttle agent, but the cells that did not contain any DDB during formation display the highest voltages during overcharge. This may be due to less facile transport of the DDB through the SEI layer.

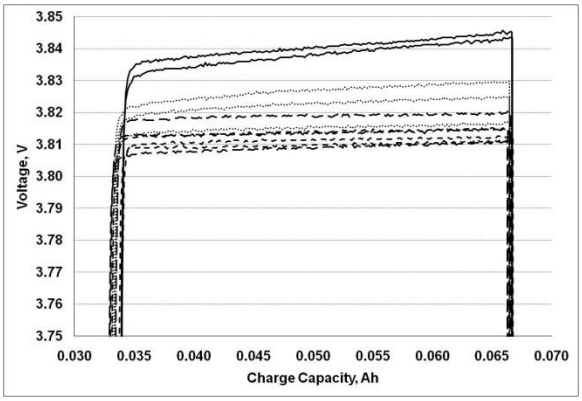

Figure 71. Voltage versus charge capacity curve for overcharge of LFP-graphite cells containing 75 mM DDB at 0.1C. Formation condition: Solid line: standard electrolyte; dashed line: standard electrolyte plus 75 mM DDB; dotted line: standard electrolyte plus 75 mM DDB and 1.65% VC; long dashed line: standard electrolyte plus 150 mM DDB.

The discharge capacity after overcharge at various C-rates for each formation condition is summarized in Figure 72. The discharge capacity is a measure of the effectiveness of overcharge protection; if the cell is effectively protected during overcharge by the redox shuttle, the discharge capacity should not be diminished since no damage to the cathode occurs. The group of cells with no DDB present during formation clearly displays the worst overcharge performance. Note that these cells are flooded with electrolyte; an optimized design would likely perform better at the higher C-rates. This data supports the hypothesis that cells formed in the presence of the redox shuttle compound DDB perform better than those formed in the absence of DDB. This effect is again attributed to molecular imprinting.

Some speculative comments follow concerning the influence of molecular imprinting on the SEI layer. It is possible that symmetric redox shuttle molecules are more successful than nonsymmetric molecules due to the fact that they will fit into the molecular recognition sites in more than one orientation. Also, molecular imprinting of the mainly organic portion of the SEI layer may change with distance from the carbon surface, reflecting the stepwise desolvation process of Li^+. Further, the SEI layer is thought to consist of a thin inorganic layer and a thicker porous organic layer, and it is likely that molecular imprinting affects mainly the organic layer. An oxidized redox shuttle species likely travels through the molecularly imprinted thick, porous organic layer and arrives at the surface of the thin, compact inorganic layer, where electron tunneling is responsible for its reduction. There is a much lower probability of solvent molecules being reduced in the same manner, since the driving force for their reduction is much lower than that of the oxidized redox shuttle species [14]. Thus the theory that SEI layers are molecularly imprinted helps explain the theories of selectivity of transport and the involvement of electron tunneling to reduce the oxidized redox shuttle species [7, 9].

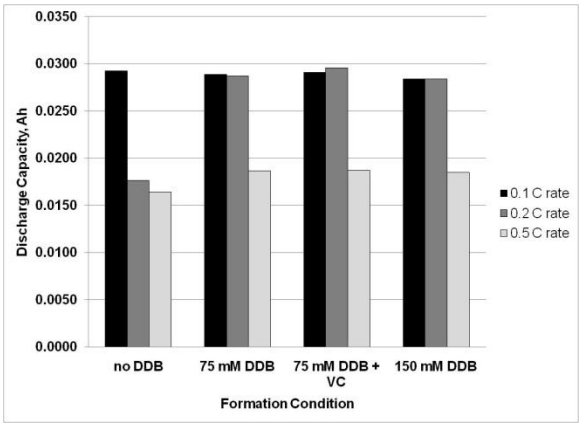

Figure 72. Plot of discharge capacity vs. formation condition for different overcharge C-rates for LFP-graphite pouch cells. Note that each group of cells contained 75 mM DDB.

3.10.3 Conclusions

The data from the above electrochemical and cell experiments support the involvement of molecular imprinting in the reduction of oxidized redox shuttle species at a carbon anode in a lithium ion cell. Indeed, molecular imprinting likely plays a role in the normal functioning of a lithium ion cell. Molecular imprinting imparts functional porosity at a molecular level to the SEI layer. Many more experiments, both diffusion controlled and non-diffusion controlled, can be envisioned to explore how molecular imprinting principles can be exploited to engineer better SEI layers for lithium ion batteries. Significantly, the large body of work that has been performed in the area of molecular imprinting can be applied to understanding the SEI layer.

3.11 4.5 V redox shuttle material from ANL

A new redox shuttle with a reported 4.5 V potential was provided by Argonne National Lab and evaluated at EnerDel. The redox potential of this shuttle was determined to be 4.52 V using cyclic voltammetry and the E_{ox}-E_{red} = ΔE = 64 mV which shows good reversibility. The shuttle's molecular formula and molecular weight were not provided so the diffusion coefficient could not be calculated. This potential is in a range that should be applicable to cells using "4 V" cathode materials.

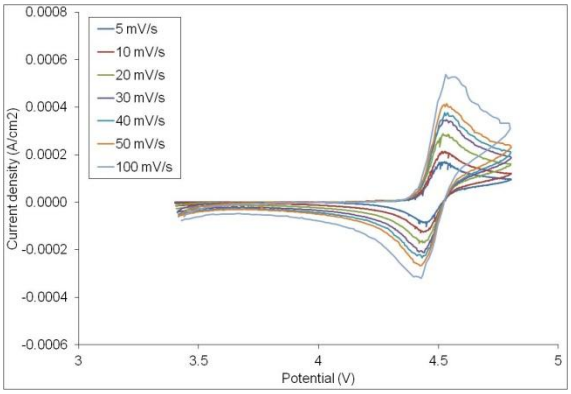

Figure 73. Cyclic voltammetry of the reported 4.5 V redox shuttle.

This redox shuttle was tested with several different anodes and cathodes. The cell chemistries that the redox shuttle was tested in are shown below. In addition, an additive was provided by ANL to be used with graphitic anodes. Cells with other anode materials were tested with and without the additive.

- NMC - HC
- NMC - graphite
- LMO - LTO
- LMO – graphite

NMC/HC cells

The voltage profile during formation for NMC/HC cells with and without the additive is shown in Figure 74. Cells with additive have a small voltage plateau at about 2.6 V, have a lower first charge capacity but a higher first discharge capacity and a higher Coulombic efficiency than cells without additive. The additive improves the formation characteristics in these cells. The Coulombic efficiency is lower compared to cells with no redox shuttle, which is typically about 74% for this cell chemistry. The Coulombic efficiency in the cells with 5% 4.5V redox shuttle is 65.0%, and the additive increases it to 71.5%.

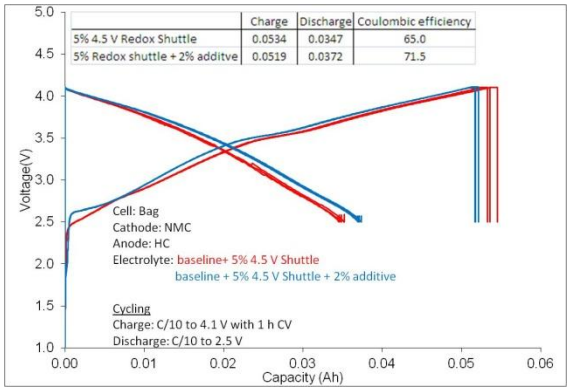

Figure 74. Voltage profile during formation for NMC/HC cells with the 4.5 V redox shuttle.

After formation, the cells were put on overcharge cycling. Overcharge cycling, for these cells and others described in this report, consisted of charging the cells to 100% SOC at the 1 C rate followed by overcharging at a C/5 rate until a 200% SOC was achieved (if the redox shuttle was effective), or a voltage well above the redox potential of the shuttle was reached (if it was not effective), unless otherwise specified. Cells were then discharged at the 1 C rate to the cell's normal discharge voltage and cycling was repeated.

The overcharge cycle life is shown in Figure 75. Although the cells cycled for up to 60 cycles, none of the cells had overcharge protection after the first 25 cycles (as marked) and many of the cells did not have protection after 10-15 cycles. Cells with additive had longer cycle life but had lower overcharge protection than cells without additive.

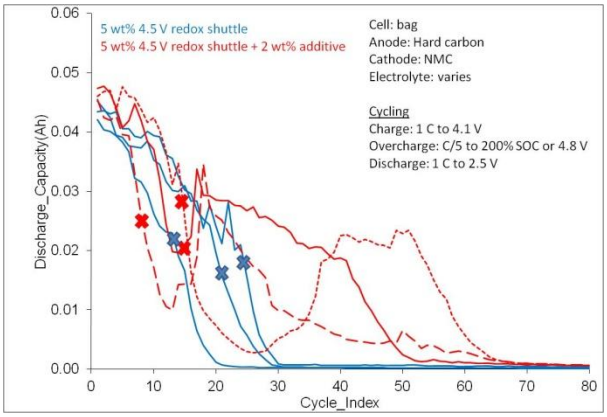

Figure 75. Overcharge cycle life of cells with the 4.5 V redox shuttle from ANL. Points marked with an X indicate where cells reached 4.8 V and complete failure of the shuttle.

The voltage profile for the first three overcharge cycles is shown in Figure 76. It is immediately obvious that the shuttle is not 100% effective in maintaining the voltage at the C/5 overcharge rate as can be seen from the increasing voltage throughout charge. If the shuttle was completely effective, a flat voltage plateau would be observed at about 4.5 V.

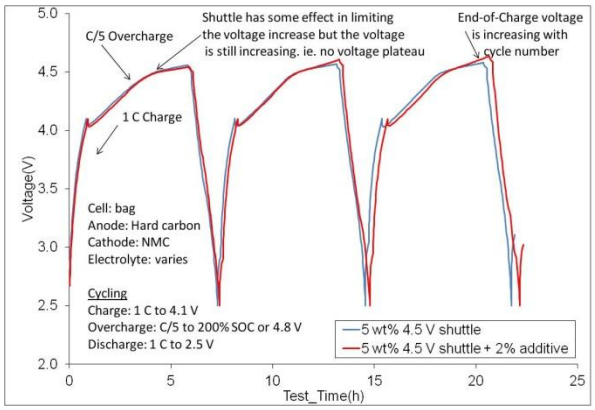

Figure 76. Voltage profile for first three overcharge cycles of NMC/HC cells.

Figure 77 shows that the end-of-charge voltage is also increasing with cycle life which indicates that the shuttle is losing its effectiveness. When the voltage first reaches 4.8 V, the shuttle was deemed to no longer be effective. Also, cells may reach 4.8 V and then have overcharge protection in subsequent cycles. This is not yet understood but in terms of effectiveness, one must consider that a large cell may have already experienced an event during the first failure to stabilize the voltage. Figure 77 also shows that the end-of-charge voltage increases very rapidly with cycle life so the actual overcharge protection may be less than the number of cycles required to reach 4.8 V. Cells with additive experienced a more rapid increase in end-of-charge voltage than cells without.

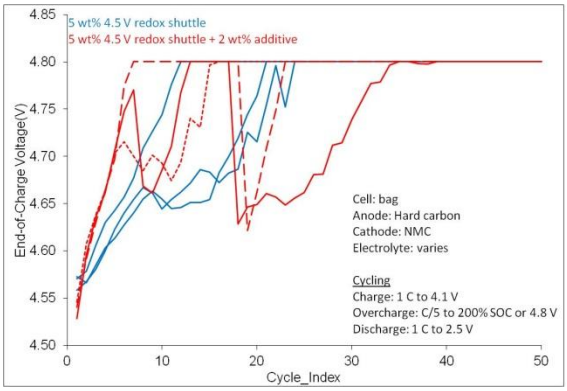

Figure 77. End-of-Charge voltage for NMC/HC cells with and without additive.

NMC/graphite cells

NMC/graphite cells were constructed and an electrolyte with 5 wt% 4.5V redox shuttle and 2 wt% additive was used in these cells. ANL advised that cells with graphite anodes require the use of additive, so testing without additive was not performed. The voltage profile during formation is shown in Figure 78. The Coulombic efficiency of the cells is lower than expected, with NMC/graphite cells normally having an efficiency of about 84%. It is unclear why these and the NMC/HC cells have a low efficiency.

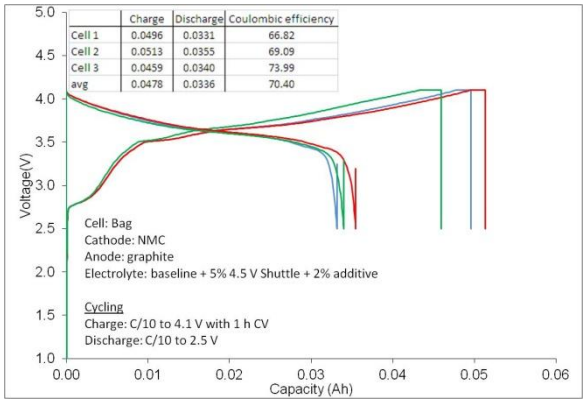

Figure 78. Voltage profile during formation for NMC/graphite cells with the 4.5 V redox shuttle

The overcharge cycle life and end-of-charge voltage for these cells is shown in Figure 79. The capacity of the cells drops rapidly with cycle life. The overcharge protection, as defined by the cells reaching 4.8 V, is between 15 and 28 cycles. This is less than the 50 and 80 cycles that ANL reported and the discrepancy is likely related to the C/5 overcharge rate that was used versus the C/10 overcharge rate that ANL used (see below). Also, it is observed that the end-of-charge voltage increases rapidly with cycling until reaching about 4.7 V, then decreases briefly before entirely losing overcharge protection. Cell failure also occurs shortly after the failure of the redox shuttle. Although cells without the shuttle were not tested in these experiments, prior experiments had shown that cells with no redox shuttle typically had longer cycle life than cells with a shuttle, but of course had no overcharge protection.

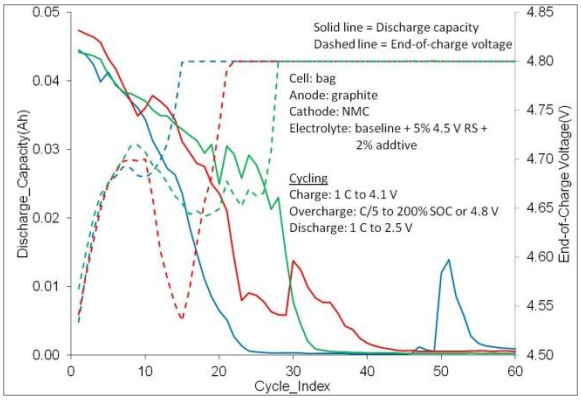

Figure 79. Overcharge cycle life and end-of-charge voltage for NMC/graphite cells

LMO/LTO

The voltage profile during formation for LMO/LTO cells with and without the additive is shown in Figure 80. Cells with additive have a small voltage plateau at about 2.1 V. Unlike NMC/HC cells, cells with additive have the same charge capacity but a lower discharge capacity and lower Coulombic efficiency.

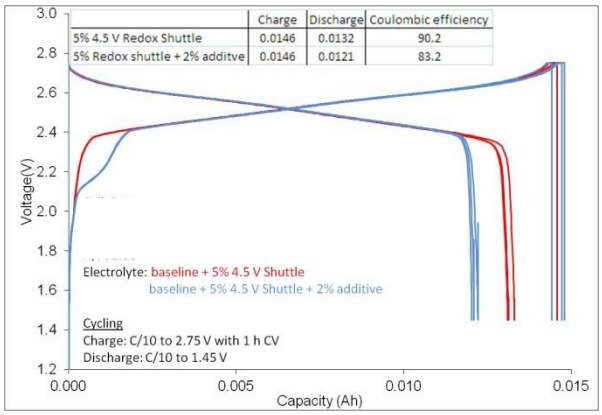

Figure 80. Voltage profile during formation for LMO/LTO cells with the 4.5 V redox shuttle

Representative voltage profiles during the first four overcharge cycles of LMO/LTO cells are shown in Figure 81. Overcharge protection is observed for the first two cycles. During the first cycle, the voltage profile is fairly flat as is desired but during the second cycle the voltage increases during overcharge and during the third overcharge cycle, both cells reach the limit of 3.25 V although the cell with no additive had a small amount of protection before the cell reached 3.25 V which is the maximum defined by the cycling profile. This is result is a little surprising since cells with LTO anodes often have better overcharge cycle life, such as LFP/LTO cells with ANL-RS2 which was described previously in another report among other examples in the literature [6].

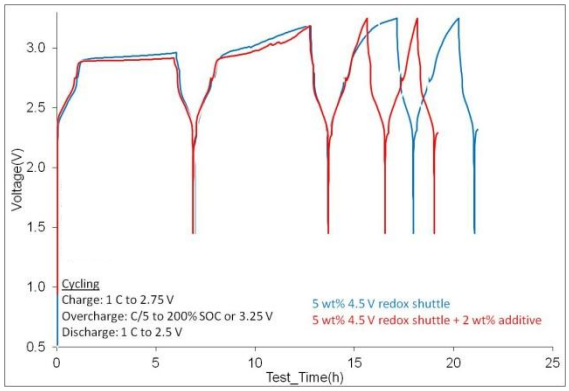

Figure 81. Voltage profile for first four overcharge cycles of LMO/LTO cells having the 4.5 V redox shuttle with and without additive

Following the failure of the shuttle to provide overcharge protection, the cells continued to cycle as shown in Figure 82. However, after the second cycle, the cells did not have overcharge protection.

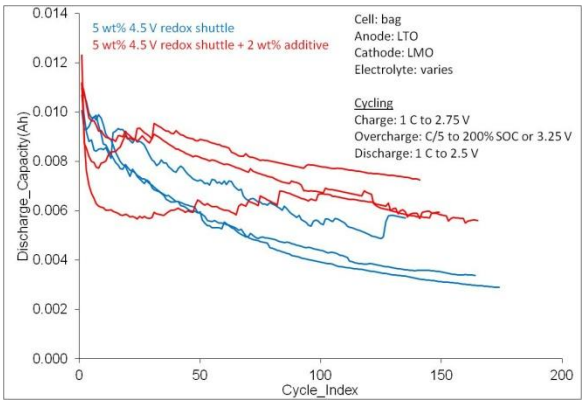

Figure 82. Overcharge cycle life of LMO/LTO cells having the 4.5 V redox shuttle with and without additive

LMO/graphite cells

After consulting with ANL, it was decided to test the 4.5 V redox shuttle in LMO/graphite cells. Testing was performed at the C/10 rates with 5 wt% redox shuttle + 2 wt% additive. Testing was also performed at the C/5 rate in LMO/graphite cells with 7 wt% shuttle + 4% additive. It was thought that the higher concentration of the redox shuttle may allow for higher overcharge rates. The voltage profile during formation for LMO/graphite cells with both electrolyte concentrations is shown in Figure 83. Cells with the higher concentration of redox shuttle and additive had similar charge capacities but lower discharge capacity and Coulombic efficiency.

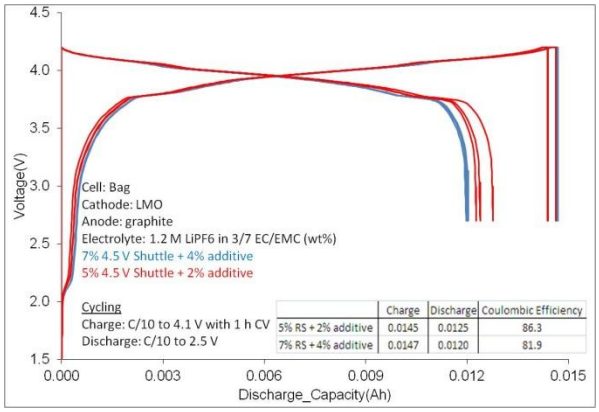

Figure 83. Voltage profile during formation for LMO/graphite cells with varying concentrations of the redox shuttle and additive

The cycle life capacity for cells cycled at the C/5 rate with 7% RS and 4% additive is shown in Figure 84.

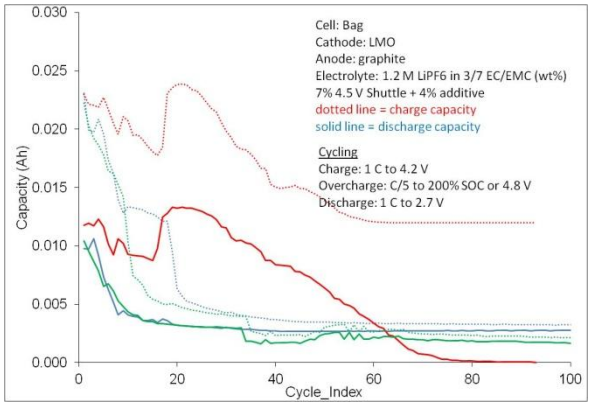

Figure 84. 100% overcharge cycle life at the C/5 rate of LMO/graphite cells with 7% redox shuttle and 4% additive

For two of the three cells, the cell capacity has fallen significantly by about 10 cycles and their end-of-charge voltage, Figure 85, increase very rapidly during the first few cycles and reaches the maximum set by the cycling program by 20 cycles. One of the cells however has much longer cycle life before losing significant capacity and while the end-of-charge voltage initially increases rapidly, it is then rather steady before decreasing. It is worth noting that after about cycle 70, the cell no longer has any discharge capacity but the cell is still charged to about 4.5 V and receives 100% overcharge. This appears to indicate that the redox shuttle is still active and has not decomposed.

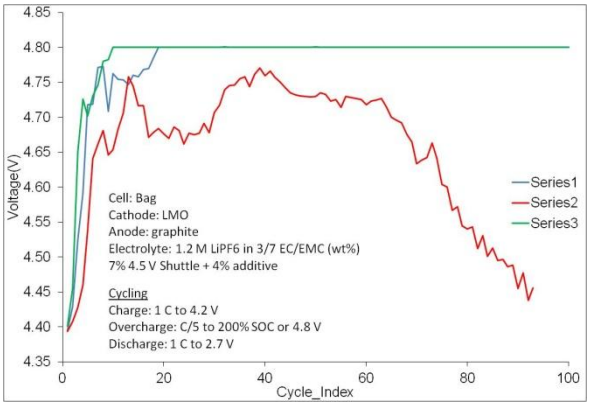

Figure 85. End-of-Charge voltage during 100% overcharge cycling at the C/5 rate of LMO/graphite cells with 7% redox shuttle and 4% additive

Two of the three LMO/graphite cells with 5 wt% redox shuttle with 2 wt% additive had a very rapid decrease in capacity after the degree of overcharge was increased from 50% to 100% after about 10 cycles while the other cell has a reasonable cycle life as shown in Figure 86. Cycling was at the C/10 rate. Furthermore, the cell that had lost less than 50% of its capacity after 50 cycles still had overcharge protection as evidenced by the end-of-charge voltage, Figure 87 that remained relatively steady at 4.65 V after it had initially increased upon going from 50 to 100% overcharge.

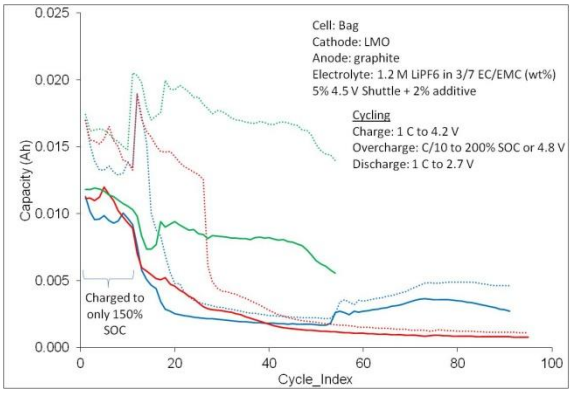

Figure 86. End-of-Charge voltage during overcharge cycle life at the C/10 rate of LMO/graphite cells with 5% redox shuttle and 2% additive. Cells were initially charged to only 50% overcharge and then overcharged to 100%. Upon changing the degree of overcharge, cell capacity dropped very rapidly for two of the cells.

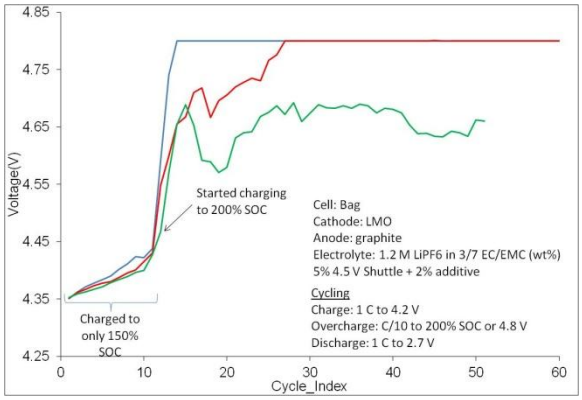

Figure 87. Overcharge cycle life at the C/10 rate of LMO/graphite cells with 5% redox shuttle and 2% additive. Cells were initially charged to only 50% overcharge and then overcharged to 100%. Upon changing the degree of overcharge, the end-of-charge voltage increased significantly for all of the cells.

Reports from ANL of a higher number of overcharge cycles are likely the result of lower overcharge currents than what has typically been used in these experiments. In general, many more overcharge cycles can be achieved at lower overcharge currents and/or lower degrees of overcharge.

3.12 Gas analysis from NMC/HC cell with $Li_2B_{12}F_{12}$ redox shuttle

Most cells containing a redox shuttle that have been overcharged to the point of failure have gas generation. Baseline cells that do not have a redox shuttle that have been overcharged under the same conditions as those having a redox shuttle have little to no gas generation (but also no overcharge protection).

The gas from a NMC/HC cell containing a commercial electrolyte with the $Li_2B_{12}F_{12}$ redox shuttle, an unknown commercial additive, and 1 wt% LiBOB was withdrawn and analyzed by GC-MS. The primary species detected were CO_2 (1.45 min) and ethylmethylcarbonate (EMC) (3.4 min) which is a solvent in the electrolyte. The GC-MS chromatogram is shown in Figure 88. Other minor species detected included various esters and ethyl hydrogen oxalate.

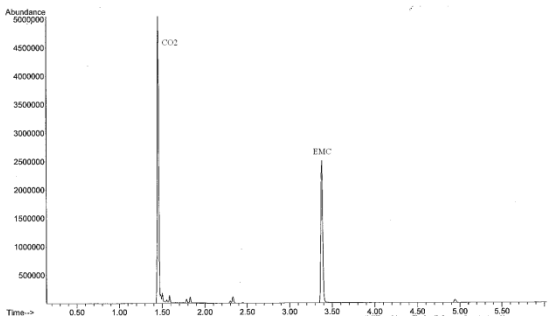

Figure 88. GC-MS chromatogram of gas from NMC/HC cell containing a commercial electrolyte with the $Li_2B_{12}F_{12}$ redox shuttle, an unknown commercial additive, and 1 wt% LiBOB after overcharge cycling.

Discussion

There are a few key observations that suggest that the interaction of the redox shuttle with the anode may be limiting the overcharge cycle life. These are:

- Longer overcharge cycle life for Li half cells
- Longer overcharge cycle life for cells with LTO anodes compared to graphitic and HC anodes
- The fact that an anode additive affects cycle life

The longer overcharge cycle life of Li half cells is believed to be due to the excess Li present in the cell. In a typical full cell, the lithium content is limited by the cathode. In a half cell, if lithium is irreversibly consumed, the Li anode can provide more lithium and capacity does not decrease as quickly.

Cells with the LTO anode also generally have longer overcharge cycle life than cells with carbonaceous anodes. LTO has a much higher potential (1.55 V) when it is fully lithiated than carbonaceous anodes (0.1 V). As a result, LTO electrodes do not have the same kind of SEI layer as carbonaceous anodes, if indeed one is present at all. Therefore, the redox shuttle lasts longer either due to the higher potential of the anode or the absence of the SEI layer.

The presence of an anode additive has also been observed to affect the overcharge cycle life. We have observed that the anode additive improves the overcharge cycle life (Figures 75 and 81) and has hurt the overcharge life during continuous overcharge in LFP/graphite cells (Figure 77). The fact that an anode additive can strongly affect overcharge cycle life suggests that the redox shuttle has an effect at the anode.

These observations also suggest that shuttle instability and cathode degradation are not major contributors to limiting the overcharge cycle life, compared to the effects at the anode.

Conclusions

A new redox shuttle with a redox potential of about 4.5 V was evaluated in several different cell chemistries. Overcharge protection was best in NMC/graphite and LMO/graphite cells. This is the most effective 4.5 V class redox shuttle that we have tested to date, but it is not stable enough to be commercially viable.

3.13 Effect of overcharge conditions

Previous observations were made that suggested that the charge rate and the state-of-charge (SOC) may affect the overcharge cycle life. To further explore these observations, LFP/graphite cells containing ANL-RS2 redox shuttle with a redox potential of 3.9 V were overcharged under the conditions listed in Table 13. Cells were overcharged at C/5 and C/10 rates to 150% and 200% SOC. Testing was terminated when the cell voltage reached 4.5 V as this voltage level signifies complete failure of the redox shuttle to prevent overcharge.

Table 13. Table of overcharge cycling conditions and points of failure of the redox shuttle

Overcharge rate	SOC (%)	# of cycles to failure	Cumulative overcharge to failure (%)
C/5	200	11-20	1100-2000
C/5	150	26-33	1350-1700
C/10	200	Ongoing (over 16)	Ongoing (over 1600)
C/10	150	Ongoing (over 25)	Ongoing (over 1250)

The overcharge protection of the cells appears to vary with the rate of overcharge. From the C/5 overcharge rate results, the overcharge protection appears to be less affected by the overcharge SOC per cycle. Figures 89 and 90 show the end-of-charge voltage versus cycle life and cumulative overcharge, respectively. Cells overcharged at the C/10 rate have an end-of-charge voltage vs. cycle curve that is increasing very slowly compared to the cells that were overcharged at the C/5 rate. Tests are ongoing for the cells overcharging at C/10 but preliminary results appear as if the lower rate significantly improves the overcharge cycle life.

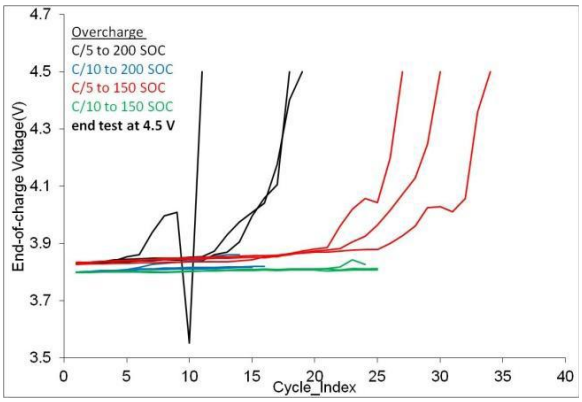

Figure 89. End-of-charge voltage versus cycle life under various overcharge conditions

There appears to be little to no difference in the cumulative overcharge performance of cells overcharged at C/5 to 200% SOC and 150% SOC. The lower overcharge rates may improve the life because it allows enough time for the proper reformation of a damaged SEI layer, since the charge rate is similar to the first cycle formation rate.

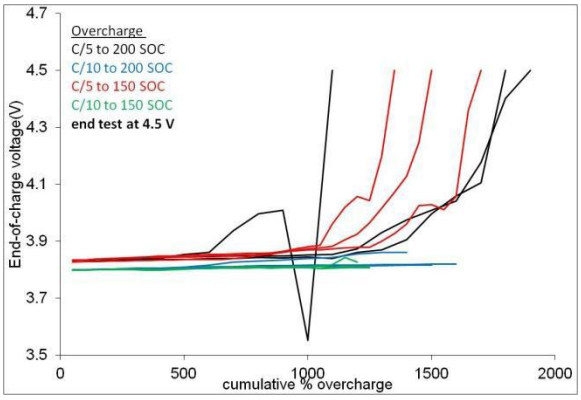

Figure 90. End-of-charge voltage versus cumulative overcharge % under various overcharge conditions

3.14 Understanding Failure of Redox shuttles

3.14.1 Heat generation

During overcharge, the redox shuttle consumes the electrons that would increase the cell voltage, thereby limiting the voltage gain in the cell. During this process, heat is generated. Data from ANL in an accelerated rate calorimeter (ARC), Figure 91, shows that over 90% of the electrical current is converted to heat. In a 50 mAh capacity cell, a 100% SOC overcharge at a C/2 rate at 3.95 V generates about 700 J of heat. If this heat is not dissipated efficiently, it could cause a substantial rise in temperature. Since the carbonaceous anode SEI layer may break down at about 100 °C, it is possible that this may be the cause of cell failure during overcharge.

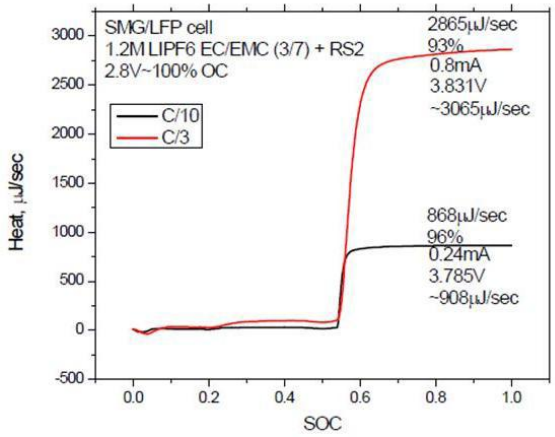

Figure 91. Accelerated Rate Calorimetry (ARC) results for a LFP/graphite cell with the ANL-RS2 redox shuttle during overcharge (data courtesy of ANL)

In order to investigate this possibility, LFP/graphite small pouch cells were overcharged with the ANL-RS2 redox shuttle at C/5 and the temperature was monitored with thermocouples attached to the outside of the pouch cell in an environmental chamber set to 25 °C. A representative plot of the data for the three cells tested is shown in Figure 92. The temperature of the cell does not increase substantially and only briefly rises above 25.5 °C. However, a large format cell where there is less external surface area for heat dissipation of more electrode stacks and also higher input currents might have heat generation problems.

It must be noted that the outside temperature of the cell may not be representative of the localized temperatures at particular areas on the anode surface, so that the possibility of thermally induced failures has not been ruled out. Additionally, the localized temperatures likely increase as the redox shuttle begins to fail and extra heat is generated during overcharge. Further, the thickness of the SEI layer increases as discussed previously, so the resistance of the SEI layer increases with overcharge cycling, which may generate more heat.

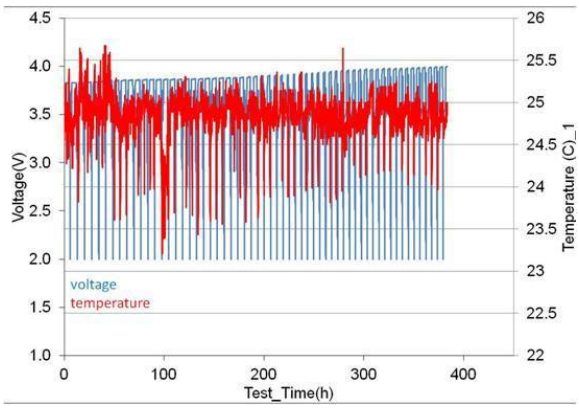

Figure 92. Cell voltage and temperature during cycling.

3.14.2 Reaction of SEI with oxidized redox shuttle

Mass spectroscopic gas analysis of the cell containing redox shuttle additive following overcharge cycling showed the generation of a large quantity of CO_2, and the amount of gas generated was much larger than cells without a redox shuttle. Furthermore, cell dissection of overcharged LFP/graphite cells with ANL-RS2 showed a black suspension in the liquid electrolyte following overcharge, Figure 93. It is speculated that gas formation may have destroyed active material or detached particles from the electrode, perhaps by deterioration of the binder. The only one of the six cells that did not have significant gas generation had electrolyte that was still clear and colorless.

Figure 93. Black suspension in electrolyte following overcharge.

One way in which CO_2 could be generated is if the Li_2CO_3, which is a known component in the anode SEI layer, were to decompose when it came in contact with the oxidized form of the redox shuttle. In order to investigate this, oxidized $Li_2B_{12}F_{12}$ was generated electrochemically on a Pt electrode held at 4.8 V in an electrochemical cell containing Li_2CO_3. Over twice the amount of current was passed to generated enough of the oxidized $Li_2B_{12}F_{12}$ shuttle to react with the Li_2CO_3 (although some could have been reduced at the Li counter and reference electrodes). The before and after pictures, Figure 94, look as if some of the Li_2CO_3 has disappeared after the $Li_2B_{12}F_{12}$ was oxidized. However, since more than twice (less the amount reduced at the Li electrodes) the amount of $Li_2B_{12}F_{12}$ was generated to react with Li_2CO_3, one would have expected that no Li_2CO_3 would remain. The final weight of the Li_2CO_3 was also less than the starting weight despite it not being able to be fully dried. The results are inconclusive since it is possible some of the Li_2CO_3 might have also dissolved in the electrolyte.

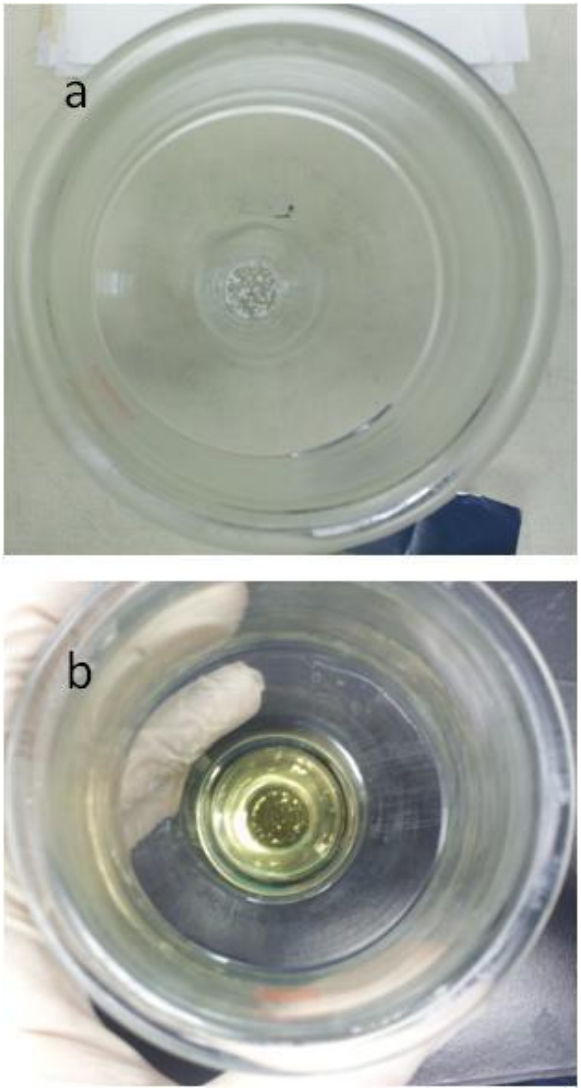

Figure 94. Before (a) and after electrochemical oxidation of $Li_2B_{12}F_{12}$ (b) pictures of Li_2CO_3 in an electrochemical cell. The amount of Li_2CO_3 appears to be reduced although not entirely gone despite more than two-fold generation of the oxidized form of the redox shuttle.

3.15 Additive testing

It has been suggested that there may be a reaction between the anode SEI layer and the oxidized form of the redox shuttle. Since there presumably is a reaction at the SEI of the anode, additives that form layers on the anode surface to protect the SEI layer may improve the overcharge performance of cells with redox shuttles. Evidence of this was reported in previous reports. Further, commercial electrolyte from Showa Denko with a redox shuttle compound, $Li_2B_{12}F_{12}$, contains an additive, and our collaborators at ANL also use an additive with some redox shuttles.

Several different additives were tested. The ANL-RS2 redox shuttle was tested in electrolytes containing 2 wt% of the additives hexafluoroglutaric acid (HFGA) and hexafluoroacetylacetone (HFacac) in LFP/graphite cells. The formation data, Figure 95, for electrolytes with these additives is not good with significantly lower Coulombic efficiencies. This could be improved by lowering the amount of the additive if evidence of good overcharge cycle life was observed compared to the cells without these additives. However, these additives made the overcharge protection worse, Figure 96, with complete failure of the redox shuttle occurring much earlier in the cycle life than cells without these additives.

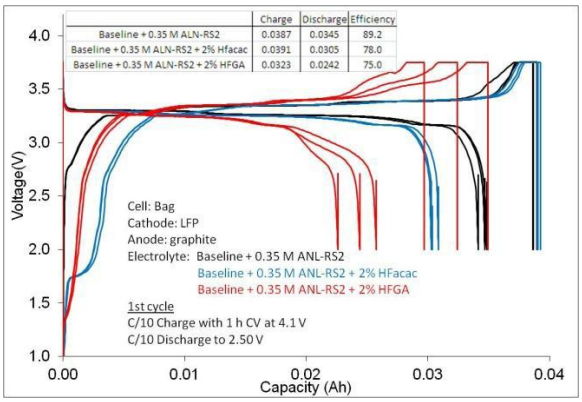

Figure 95. Formation data for LFP/graphite cells with the ANL-RS2 redox shuttle with and without additives

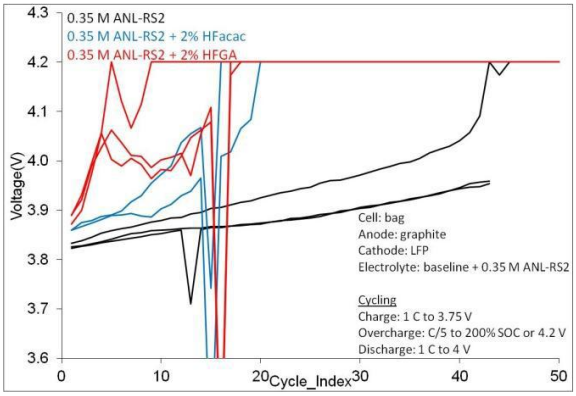

Figure 96. End-of-charge voltage versus cycle life for LFP/graphite cells with the ANL-RS2 redox shuttle with and without additives

Other additives that were tested were hexafluorobutyric anhydride (HFB) and tetrafluorophthalic anhydride (TFPT) in NMC/HC cells with 0.2 M $Li_2B_{12}F_{12}$ as the redox shuttle. LiBOB was used as an additive in some of the cells as well. The formation data, Figure 97, is good with the charge, discharge, and Coulombic efficiency about the same as cells with no additives. Cells with LiBOB have a voltage plateau at about 2.7 V.

The end-of-charge voltage during C/5 overcharge versus cycle life is shown in Figure 98. The cells that had LiBOB present have a longer overcharge cycle life than the other cells. Cells with TFPT may have slightly longer cycle life than cells without an additive but the difference is marginal. Cells with HFP have the same cycle life as cells with the baseline electrolyte.

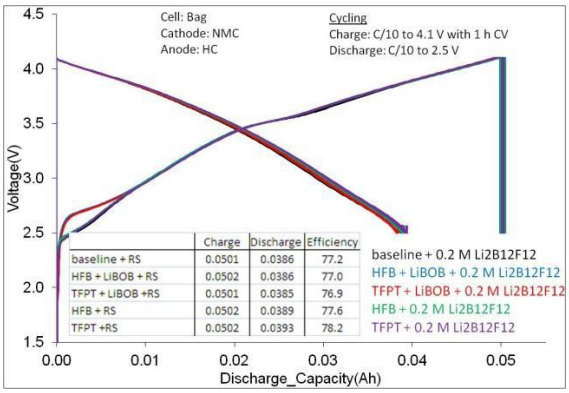

Figure 97. First cycle of NMC/HC cells with 0.2 M $Li_2B_{12}F_{12}$ with various additives.

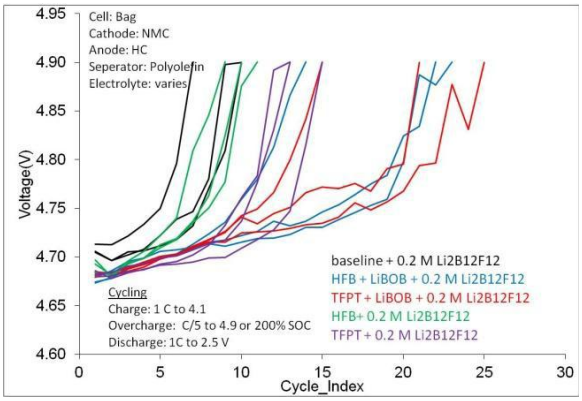

Figure 98. End-of-charge voltage versus cycle life for NMC/HC cells with $Li_2B_{12}F_{12}$ with various additives.

3.16 An Ultra-Controlled Cell

Li-ion cells, like many other battery chemistries, have a risk for a thermal event under abusive conditions. An approach to reducing this risk and improving the control of Li-ion cells is to limit the state-of-charge (SOC) of the cathode while also incorporating a redox shuttle to ensure that it does not exceed this SOC should the control electronics fail. The possibility of using NMC cathode material at a lower voltage than is typically employed coupled with the use of ANL-RS2 redox shuttle to produce an ultra-controlled cell was explored.

The maximum potential that cells could be charged to before significant self-discharge occurred with the ANL-RS2 shuttle was determined using NMC/Li cells. The cells were charged to various potentials at C/5 and holding the voltage at that potential for 24 hours followed by a C/5 discharge to 2.5 V. By holding at a specified potential for 24 hours, self-discharge effects should be amplified and easier to observe. Cells without a redox shuttle were also constructed for comparison. The charge, discharge, and

Coulombic efficiency at each charging voltage for representative baseline and redox shuttle cells are shown in the Table 14 below. The capacity for half cells in the absence of ANL-RS2 with this NMC loading is about 41 mAh when charged to 4.1 V with a 1 hour CV. The Coulombic efficiency and capacity versus charging voltage is shown in Figures 99 and 100, respectively.

Table 14. Charge, discharge, and Coulombic efficiency for NMC/Li cells with and without ANL-RS2 redox shuttle

	no shuttle			ANL-RS2 Redox Shuttle		
voltage	Charge	Discharge	efficiency	Charge	Discharge	efficiency
3.60	0.0009	0.0001	14.4	0.0011	0.0001	10.5
3.65	0.0030	0.0005	16.1	0.0032	0.0004	14.0
3.70	0.0062	0.0037	60.2	0.0064	0.0036	55.2
3.75	0.0122	0.0115	94.4	0.0127	0.0111	87.7
3.80	0.0211	0.0203	96.3	0.0240	0.0197	82.4
3.85	0.0277	0.0270	97.5	0.0430	0.0256	59.6
3.90	0.0326	0.0316	97.0	0.0952	0.0291	30.6

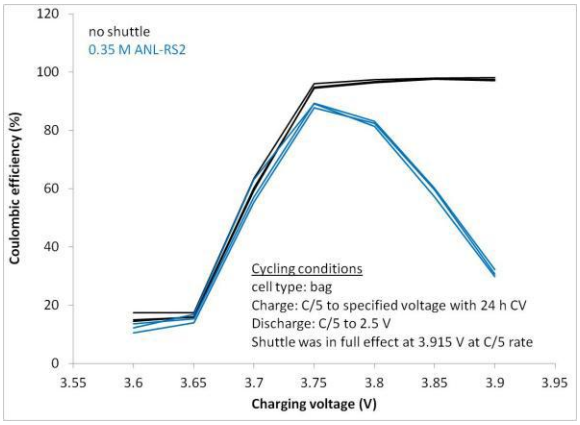

Figure 99. Coulombic efficiency versus charging voltage for NMC/Li cells with and without ANL-RS2 redox shuttle

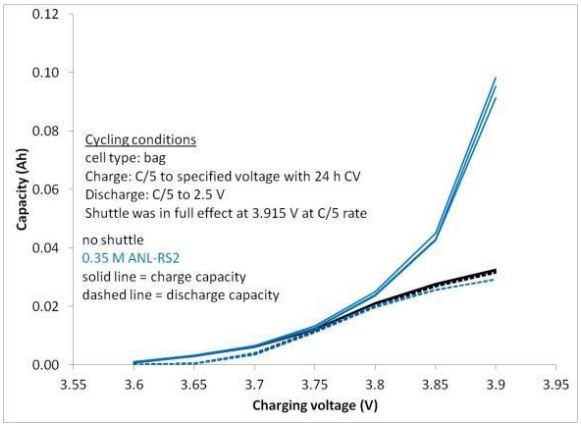

Figure 100. Charge and discharge capacity versus charging voltage for NMC/Li cells with and without ANL-RS2 redox shuttle

The data shows that the ANL-RS2 redox shuttle is effective at limiting the voltage to 3.915 V. However, prior to reaching this voltage, there is leakage current or self-discharge of the cell due to partial operation of the redox shuttle. This is normal electrochemical behavior.

The highest voltage that could realistically be used in cells with ANL-RS2 redox shuttle is about 3.75 V and even at this voltage the self-discharge is elevated compared to cells without a redox shuttle. The capacity for the NMC at this voltage is only 11.5 mAh, compared to 41 mAh that would be expected if the cell was charged to 4.1 V. This capacity is probably too low and would yield very poor energy density in a cell. In order to develop an extremely controlled cell with this concept, either a new redox with a redox potential in the range of about 4.1-4.2 V would need to be found or a different cathode material with a lower intercalation potential is needed.

3.17 Effect of overcharge conditions

Prior observations were made that suggested the charge rate and the state-of-charge (SOC) may affect the overcharge cycle life. Experiments were performed that overcharged LFP/graphite cells with the ANL-RS2 shuttle (redox potential 3.9 V) under the conditions listed in Table 15. Cells were overcharged at C/5 and C/10 rates to 150% and 200% SOC. Testing was terminated when the cell voltage reached 4.5 V as this signifies complete failure of the redox shuttle to prevent overcharge.

Table 15. Table of overcharge cycling conditions and points of failure of the redox shuttle

Overcharge rate	SOC (%)	# of cycles to failure	Cumulative overcharge to failure (%)
C/5	200	11-20	1100-2000
C/5	150	26-33	1350-1700
C/10	200	20-40	2000-4000
C/10	150	70-90	3500-4500

The overcharge protection of the cells appears vary with the rate of overcharge and is mostly independent of the SOC during overcharge. Figures 101 and 102 show the end-of-charge voltage versus cycle life and cumulative overcharge, respectively. Cells overcharged at the C/10 rate have greater overcharge cycle life and are capable of handling more cumulative overcharge than cells overcharged at C/5. The lower overcharge rates may improve the life because it allows enough time for the proper reformation of the SEI; i.e. charge rate is similar to the first cycle formation rate. There appears to be little to no difference in the cumulative overcharge of cells overcharged at C/5 to 200% SOC and 150% SOC. At a C/10 rate, cells that are cycled to 150% SOC accumulate more overcharge than cells charged to 200% SOC before overcharge protection fails. This may be due to a lower maximum temperature reached at localized areas on the anode surface.

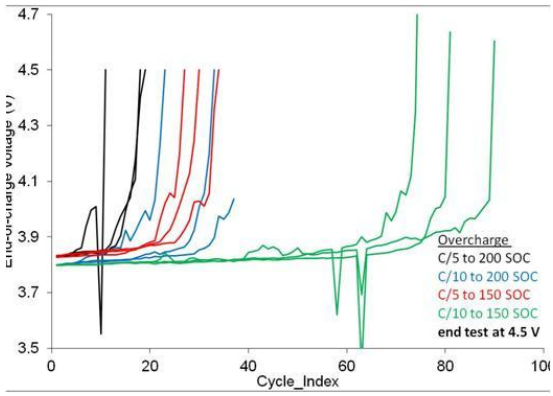

Figure 101. End-of-charge voltage versus cycle life under various overcharge conditions.

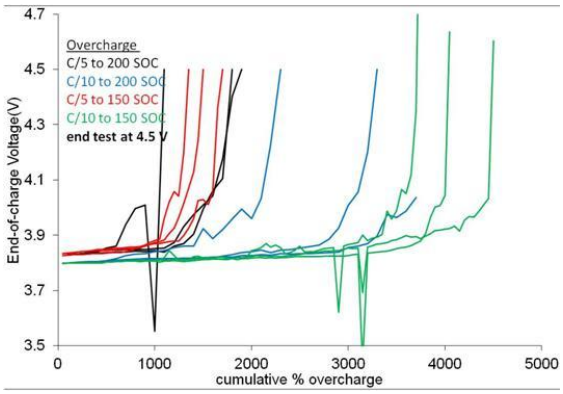

Figure 102. End-of-charge voltage versus cumulative overcharge % under various overcharge conditions.

3.18 Effect of Anode on the Capacity Loss of Li-ion Cells with Redox Shuttles during Overcharge

3.18.1 Introduction

Redox shuttles provide a number of overcharge protection cycles for Li-ion cells. Cells with lithium anodes exhibit the largest number of protected overcharge cycles and cells with carbonaceous anodes exhibit the smallest number of protected overcharge cycles, with cells employing lithium titanate (LTO) anodes in the middle of these two extremes. Full cells with ANL-RS2 redox shuttle using lithium iron phosphate (LFP) cathodes and either graphite or LTO anodes were overcharge cycled and analyzed to explain the differing overcharge cycle life. The negative-to-positive (N/P) ratio of LFP-graphite cells decreases more rapidly than that of LFP-LTO cells, resulting in decreased overcharge cycle life. The redox shuttle ANL-RS2 likely undergoes oxidative dehydrogenation and oxygen insertion during overcharge cycling, perhaps catalyzed by the delithiated LFP cathode.

Redox shuttle molecules prevent the overcharge of cells electrochemically. An effective redox shuttle species should have an oxidation potential about 0.2 to 0.3 V above the maximum desired cathode potential during normal operation. If the cell enters an overcharged state, the redox shuttle consumes charge when its oxidation potential is reached. It is oxidized at the cathode, and then diffuses to the

anode, where it is reduced. This cycle ideally can be repeated indefinitely for a species with chemically and electrochemically stable oxidized and reduced forms [14].

A redox shuttle developed at Argonne National Laboratory, 1,4-bis(2-methoxyethoxy)-2,5-di-*tert*-butyl-benzene (ANL-RS2), has been evaluated for overcharge protection and cell rebalancing in lithium iron phosphate (LFP) – graphite and LFP – lithium titanate (LTO) cells. In addition to providing overcharge protection, ANL-RS2 has a reported higher solubility in typical lithium ion battery electrolytes than 1,4-di-*tert*-butyl-2,5-dimethoxybenzene, a well-known redox shuttle compound [15].

It has been observed that the number of successful overcharge cycles that can be achieved using a redox shuttle compound depends on the type of anode employed [6]. It was suggested that a reaction between the solid electrolyte interphase (SEI) layer and the redox shuttle may be occurring. Since carbonaceous anodes operate at a low potential that results in solid electrolyte interphase (SEI) layer formation and LTO anodes typically operate around 1.5 V vs. Li^+/Li with little or no SEI layer formation, this theory is reasonable. Given the trend of less overcharge protection cycles for carbonaceous anodes, there may be a destructive reaction between the anode solid electrolyte interphase (SEI) layer and the redox shuttle. Analysis of formed and overcharge cycled cells with ANL-RS2 redox shuttle was performed to characterize the role that the anodes play in the eventual failure observed in the cells.

3.18.2 Experimental

Cell experiments were performed using EnerDel standard R&D pouch cells with approximately 35 mAh capacity for the LFP – graphite chemistry and approximately 11 mAh capacity for the LFP – LTO chemistry. PVdF binder was employed for each coating. Nine cells of each chemistry were fabricated using standard EnerDel R&D procedures and activated with electrolyte (Table 16). An Arbin BT2000 battery cycler was employed for cell testing (Table 17). LFP - graphite cells were removed from the battery cycler in three groups: after formation, after 10 overcharge cycles, and after failure (typically about 40 cycles). For a fair comparison, LFP - LTO cells were also removed from the battery cycler in three groups: after formation, after 10 overcharge cycles, and after 40 overcharge cycles, even though they had not yet failed. EIS testing was performed using a Solartron SI 1287 Electrochemical Interface, SI 1255 HF High Frequency Analyzer, and SI 1260 Impedance/Gain Phase Analyzer, with ZPlot and Zview software (Scribner Associates, Inc., Southern Pines, NC). The pouch cells were opened in a dry room with dew point -60°F to -110°F. First, a small corner of the pouch cell was clipped and the excess electrolyte was drained into a container. Next, the anode, cathode, and separator were carefully detatched from one another. Coin cell electrodes were punched from the pouch cell electrodes and the electrode thickness and weight were recorded, then 2032 coin cells using lithium metal as the anode and 0.100 ml of fresh electrolyte were fabricated. A capacity check (Table 17) was run on the half cells made from LFP, LTO, and graphite to determine the capacity remaining in the formed and overcycled electrodes, followed by EIS.

Table 16. Full and half cell electrolyte compositions. EC = ethylene carbonate; DEC = diethyl carbonate; PC = propylene carbonate; EMC = ethyl methyl carbonate; ANL-RS2 = 1,4-bis(2-methoxyethoxy)-2,5-di-*tert*-butyl-benzene

Chemistry	Electrolyte Composition
LFP - graphite	3:7 EC:DEC, 1.2 M $LiPF_6$, 0.35 M ANL-RS2
LFP - LTO	25:5:70 EC:PC:EMC, 1.2M $LiPF_6$, 0.35 M ANL-RS2
LFP – Li and LTO - Li	25:5:70 EC:PC:EMC, 1.2M $LiPF_6$
Graphite - Li	3:7 EC:DEC, 1.2 M $LiPF_6$

Table 17. Formation, overcharge cycling, and capacity check schedules

Cell Chemistry Experiment	Schedule
LFP-graphite Formation	Charge at 0.1 C to 3.75 V; rest 10 minutes; discharge at 0.1 C to 2.5 V; rest 10 minutes; repeat
LFP- graphite Overcharge cycles	Charge at 1 C to 3.7 V; overcharge at 0.2 C to 4.2 V or 200% capacity; rest 10 minutes; discharge at 1 C to 2.5 V
LFP-LTO Formation	Charge at 0.1 C to 2.2 V; rest 10 minutes; discharge at 0.1 C to 1.0 V; rest 10 minutes; repeat
LFP-LTO Overcharge cycles	Charge at 1 C to 2.1 V; overcharge at 0.2 C to 4.2 V or 200% capacity; rest 10 minutes; discharge at 1 C to 1.0 V
LFP-Li Capacity Check	Charge at 0.1 C to 4.0 V; hold at 4.0 V for 1 hour; rest 10 minutes; discharge at 0.1 C to 2.5 V; rest 10 minutes; repeat
Graphite-Li Capacity Check	Charge at 0.1 C to 0.002 V; hold at 0.002 V for 1 hour; rest 10 minutes; discharge at 0.1 C to 1.5 V; repeat
LTO-Li Capacity Check	Charge at 0.1 C to 1.0 V; hold at 1.0 V for 1 hour; rest 10 minutes; discharge at 0.1 C to 2.5 V; repeat

The electrolyte from the formed and overcharged pouch cells as well as the anode, cathode, and separator samples were subjected to various analytical tests. Gas samples, dilutions of the electrolyte, and extractions of the solids in methanol or acetonitrile were analyzed using gas chromatography – mass spectrometry (GC-MS, Agilent 7890A Gas Chromatograph with 5975C Inert XL Mass Sensitive Detector). Solid surfaces and liquids were analyzed using attenuated total reflection infrared absorption spectroscopy (FTIR, Thermo Scientific Nicolet 6700 FTIR) and Raman spectroscopy (Thermo Scientific DXR Raman microscope using 532 nm laser excitation). Scanning electron micrographs were taken using a Zeiss EVO MA10 scanning electron microscope (SEM) with a Bruker Quantax 200 energy dispersive spectroscopic analysis (EDS). Thermal analysis was performed using a TA Instruments Q2000 Differential Scanning Calorimeter (DSC) and a Q5000 Thermogravimetric Analyzer (TGA).

3.18.3 Cell Results and Discussion

Thermocouples were attached to the outside of the LFP-graphite pouch cell packaging to monitor the temperature during overcharge cycling. A significant temperature rise was not observed at the 0.2 C overcharge rate as can be seen in Figure 103; however, the localized internal cell temperature may be higher.

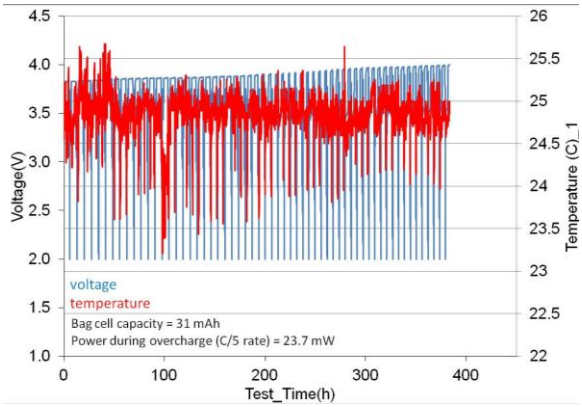

Figure 103. Voltage and temperature measurements for an LFP-graphite full cell during overcharge cycling

Gas is generated by the overcharge cycling in the presence of the redox shuttle, and the amount of gas increases with the number of overcharge cycles. Much less gas is produced by the LFP-LTO cells than the LFP-graphite cells for a given number of cycles. The gas was analyzed using GC-MS and it was found to be mainly CO_2 (if hydrogen was present, it was not detected due to the use of helium as carrier gas). Some other volatile small molecules, such as POF_3, oxalic acid, methoxyethane, and 1,2-diethoxyethane were also detected. HF was probably produced as well but likely reacted with a chemical present in the cell, so it was not detected. The CO_2 could be produced from HF or other acid reacting with the Li_2CO_3 in the SEI layer, or from some other reaction with the oxidized redox shuttle.

Figure 104. LFP-graphite cells after being formed (left), 10 overcharge cycles (middle), and overcharge cycled to failure (right). Note the increasing amount of gas that is formed with overcharge cycling in the presence of the redox shuttle

EIS was run on the cells and is shown in Figure 105 below for LFP-graphite and LFP-LTO cells after formation and after 10 overcharge cycles. The impedance of the LFP-graphite cells increases greatly with overcharge cycling, and gas formation is one obvious factor. The impedance of the LFP-LTO cells increases less than the LFP-graphite cells for 10 overcharge cycles, which is consistent with the observations that less gas is formed and that the cells with LTO anodes have longer overcharge cycle life.

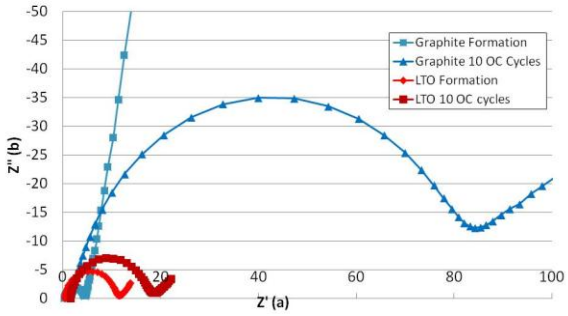

Figure 105. EIS spectra for LFP-graphite cells after formation (blue squares) and 10 overcharge cycles (blue triangles) and for LFP-LTO cells after formation (red diamonds) and after 10 overcharge cycles (red squares)

Electrolyte from formed cells is virtually unchanged visually from its original form, being clear and colorless with perhaps a very slight yellow tint, and with the same approximate viscosity. The electrolyte becomes increasingly dark brown in color and the viscosity increases substantially with overcharge cycling. It is important to note that an increase in viscosity decreases the current that can be successfully shuttled by the redox shuttle compound. The polyolefin separator, which is initially white in color, turns light brown and then dark brown with increased overcharge cycling. Electrolyte and separator from LFP-LTO cells are less discolored than electrolyte and separator from LFP-graphite cells for the same number of overcharge cycles.

Figure 106. Electrolyte drained from the LFP-graphite cells after formation (left), 10 overcharge cycles (middle), and overcharge cycling to failure (right)

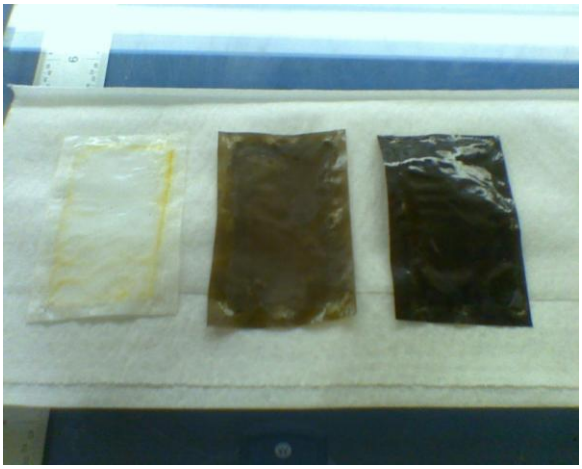

Figure 107. Separators taken from LFP-graphite cells after formation (left), 10 overcharge cycles (middle) and overcharge cycling to failure (right)

Half cell capacity checks were performed on the anode and cathode materials from each of the six groups of cells and the results are presented in Figures 108 and 109. The capacity of the graphite and LTO anodes decreases more rapidly than the capacity of the LFP cathodes; therefore, the anodes are more affected by the presence of the oxidized redox shuttle compound than the LFP is. Also, LTO appears to be less affected than graphite for a given number of overcharge cycles.

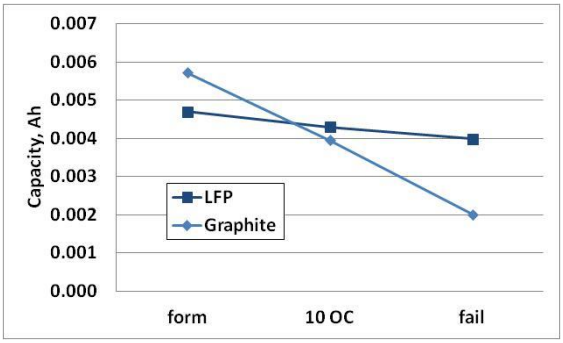

Figure 108. Capacity of half coin cells fabricated using the LFP or the graphite electrodes from LFP-graphite full cells after formation, 10 overcharge cycles, and overcharge cycling to failure

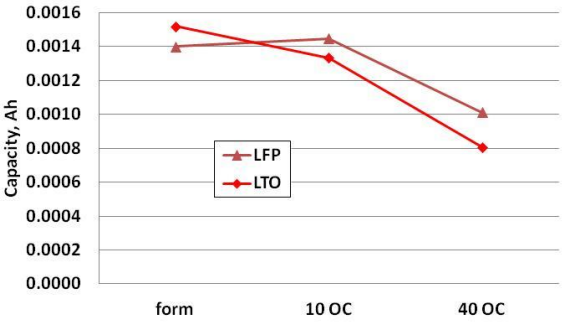

Figure 109. Capacity of half coin cells fabricated using the LFP or the LTO electrodes from LFP - LTO full cells after formation, 10 overcharge cycles, and 40 overcharge cycles

The negative-to-positive ratio (N/P ratio) is an important parameter in battery design and represents the ratio of the amount of anode capacity to the amount of cathode capacity. The half cell capacity data from Figures 108 and 109 was used to calculate the N/P ratio for each type of full cell and is presented in Figure 110. The N/P ratio of the LFP-graphite cells is initially greater than one and decreases to below one with overcharge cycling. This creates a situation where the cathode provides more Li ions than the anode can intercalate, and Li metal dendrites may be created, causing rapid capacity fade. Cells with carbon anodes should have an N/P ratio greater than one for good cycle life. In the case of LFP-LTO, the N/P ratio starts at about one, but decreases to below one with overcharge cycling. In contrast to the graphite case, cells with LTO anodes actually cycle better with an N/P ratio less than one [16]. Therefore, in addition to other possible factors, cells with LTO anodes will have better overcharge cycling than cells with graphite anodes due to this N/P ratio consideration.

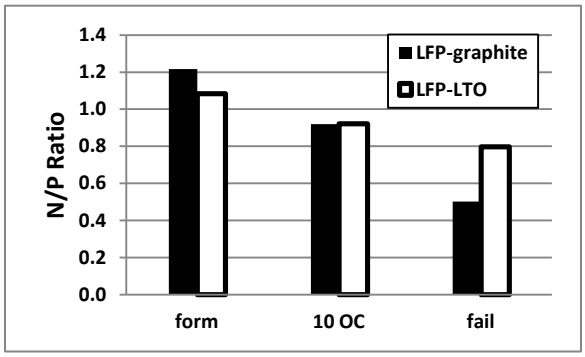

Figure 110. N/P ratio for LFP-graphite and LFP-LTO cells after formation, 10 overcharge cycles, and failure (40 overcharge cycles for the LFP-LTO cells)

The electrodes that were harvested from the LFP-graphite and LFP-LTO cells were weighed and the thicknesses were measured. From this data, the porosity and the density of the electrodes could be calculated. The cathodes did not exhibit a significant change in porosity or density, but the anodes became heavier with overcharge cycling while the thickness remained fairly constant. The calculated porosity and density of the anodes is shown in Figures 111 and 112. The decrease in porosity and the increase of the density of the anodes is evident. This implies that the pores are filling with a substance such as SEI layer products, redox shuttle molecules or reaction products, other reaction products from electrolyte or binder, or lithium dendrites. The graphite is affected more than the LTO and this correlates with the capacity fade trend. The seemingly insoluble reaction products are likely preventing some lithium ions from participating in the charge/discharge process. It is also likely that this results in the increase of the SEI layer resistance. Additionally, pores may be clogged with reaction products, and this effectively decreases the available electrode surface area. These factors may cause the increase of the amount of heat generated during the shuttling process and a tipping point may occur when a temperature that causes disruption of the SEI layer is reached.

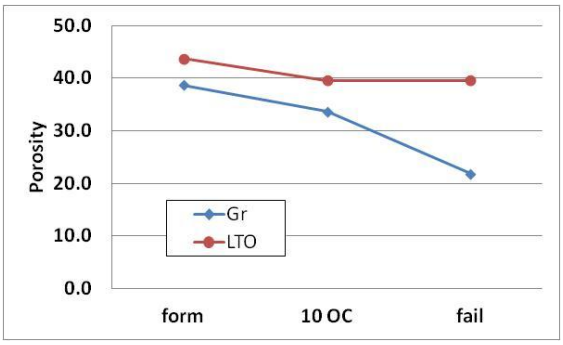

Figure 111. Porosity for graphite and LTO electrodes from LFP-graphite and LFP-LTO cells after formation, 10 overcharge cycles, and failure (40 overcharge cycles for the LFP-LTO cells)

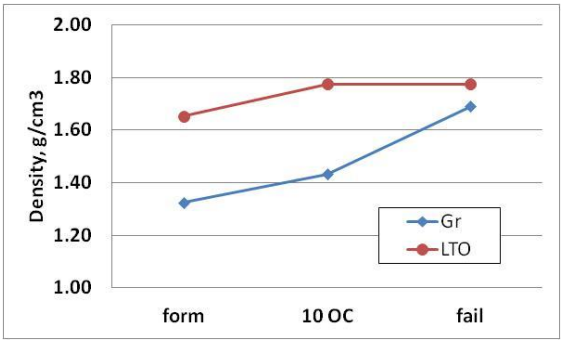

Figure 112. Density for graphite and LTO electrodes from LFP-graphite and LFP-LTO cells after formation, 10 overcharge cycles, and failure (40 overcharge cycles for the LFP-LTO cells)

EIS was run on the half coin cells made using the electrodes harvested from the full cells. The results for the graphite half cells taken from the LFP-graphite full cells after formation, 10 overcharge cycles, and overcharged to failure are presented in Figure 113. The half cells were at 0 % state of charge. The graphite after formation has the lowest impedance and the graphite after overcharge to failure have the highest impedance, with the graphite after 10 overcharge cycles in the middle of these two extremes. This implies that either the SEI layer has increased in thickness or become more resistive due to a different chemical composition, or both. Additionally, the desolvation of the Li^+ ions at the anode may be impacted by the change in the SEI layer, or the Li^+ ions are at least partially solvated by different species that were produced by decomposition of the redox shuttle species.

EIS analysis of the graphite half cells charged to 100% state of charge also showed that the impedance of the cells that were overcharge cycled to failure increased compared to the impedance of the cells with 10 overcharge cycles as shown in Figure 114.

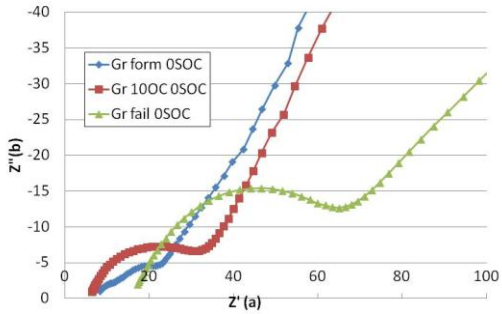

Figure 113. EIS results for graphite half cells at 0% state of charge made from LFP-graphite cells after formation, 10 overcharge cycles, and overcharge cycling to failure

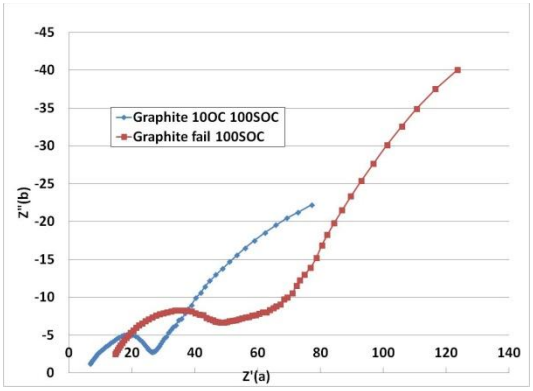

Figure 114. EIS results for graphite half cells at 100% state of charge made from LFP-graphite cells after 10 overcharge cycles and overcharge cycling to failure

EIS results for the LTO half cells taken from the LFP-LTO full cells after formation and 10 overcharge cycles are presented in Figure 115. The half cells were at 100 % state of charge. The high frequency semicircle at the left part of the trace represents the SEI or interfacial resistance. The SEI or interfacial resistance of the LTO after formation and after 10 overcharge cycles is roughly the same. Since the LTO should not have an appreciable SEI layer, we will assign this semicircle to interfacial resistance and it is higher than that of graphite. The lower frequency semicircle is more prominent for the LTO that had experienced 10 overcharge cycles than the LTO that had experienced formation only. This semicircle in the EIS spectrum is associated with the charge transfer resistance, or the desolvation of the Li^+ ions prior to insertion. The higher impedance could imply that the Li^+ ions are at least partially solvated with another species, perhaps one of the chemically oxidized ANL-RS2 molecules, that has a higher energy of desolvation than that of EC. It could also imply that the large amount of EC that was detected at the anodes (see below) pushes the equilibrium toward EC-solvated Li^+, thus making it more difficult to desolvate the Li^+ ions prior to intercalation.

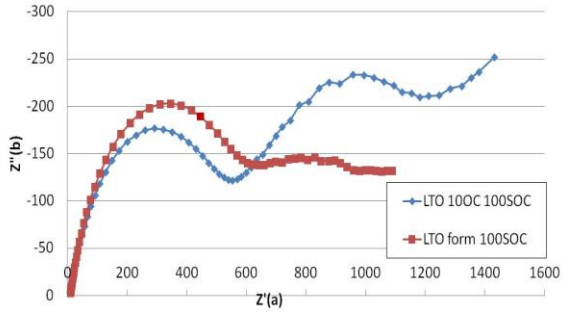

Figure 115. EIS results for LTO half cells at 100 state of charge made from LFP-LTO cells after formation or 10 overcharge cycles

3.18.4 Analytical Results and Discussion

Dilutions of electrolyte and extractions of anode, cathode, and separator materials were analyzed using GC-MS. The data is shown in Figures 117-120 below and is summarized here. As the overcharge cycling progresses, the amount of redox shuttle decreases, which implies that it is being consumed in a reaction or sequestered in the active material pores where it cannot be extracted. New peaks appeared in the GC-MS total ion chromatogram of the electrolyte drained from both the LFP-LTO and the LFP-graphite cells as overcharge cycling progressed and the data is summarized in Table 18. The LFP-graphite chemistry is discussed here since the changes occur more rapidly than in the LFP-LTO chemistry. Similar changes were observed in the extracts of the anode, cathode, and separator materials.

Table 18. Molecular ion mass-to-charge ratio (m/z), retention times, and relative amounts based on integrated peak area of ANL-RS2 and oxidation products of ANL-RS2 for LFP-graphite cells according to GC-MS electrolyte analysis.

	ANL-RS2	**ANL-RS2-O**	**ANL-RS2-2O**
Molecular ion, m/z	338	352	366
Retention time, min.	21.87	22.38	22.88
Formation, %	100.0	0	0
10 OC Cycles, %	95.6	4.4	0
Fail, %	80.3	14.9	4.8

Table 19. Mass spectral intensity ratios for ANL-RS2, ANL-RS2-O, and ANL-RS2-2O.

m/z Peak Area Ratio	ANL-RS2	ANL-RS2-O	ANL-RS2-2O	Comments
57/molecular ion	0.22	0.25	0.21	*tert*-butyl group, approx. ratio 1:1:1
59/molecular ion	0.89	0.57	0.06	$C_2H_4OCH_3$ group, approx. ratio 2:1:0
73/molecular ion	0.00	0.30	0.60	$C_2OH_2OCH_3$ group, approx. ratio 0:1:2

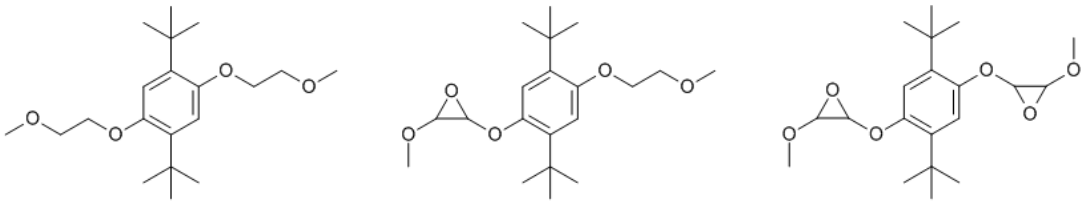

Figure 116. Structure of ANL-RS2 (left) and proposed structures for ANL-RS2-O (middle) and ANL-RS2-2O (right) rendered as epoxides

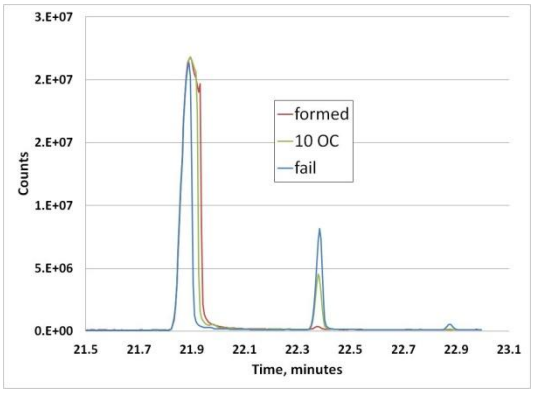

Figure 117. GC-MS chromatographic trace for electrolyte taken from LFP-graphite cells after formation (red), 10 overcharge cycles (green), and overcharge cycling to failure (blue)

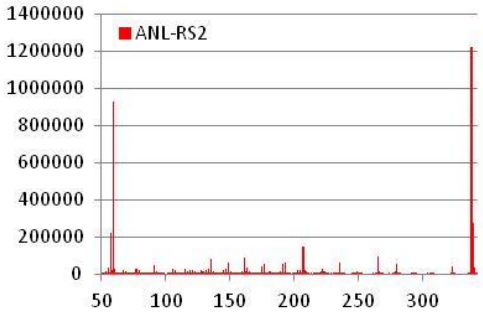

Figure 118. Mass spectrum of ANL-RS2, electron impact ionization. Parent ion at m/z 338.

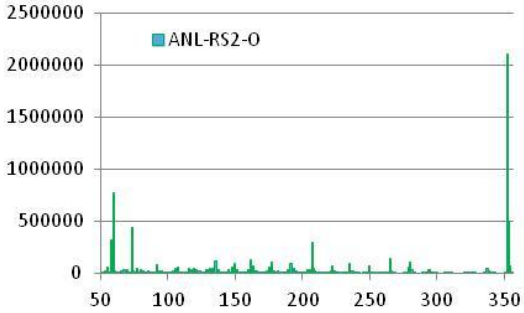

Figure 119. Mass spectrum of ANL-RS2-O, electron impact ionization. Parent ion at m/z 352. Note the new signal at m/z 73 and the changing abundance of the signals at m/z 57 and m/z 59.

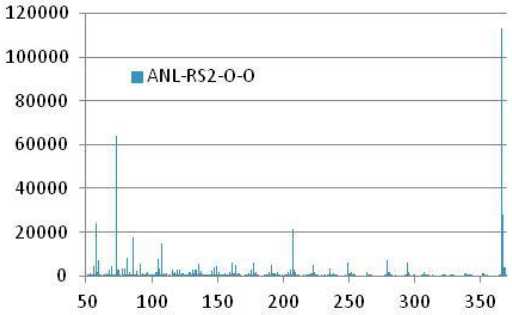

Figure 120. Mass spectrum of ANL-RS2-2O, electron impact ionization. Parent ion at m/z 366. Note the larger abundance of signal at m/z 73 and the changing abundance of the signals at 57 and 59 m/z.

The compounds associated with the new peaks at retention time 22.38 and 22.88 minutes are designated ANL-RS2-O and ANL-RS2-2O, respectively. The increase in molecular weight of 14 atomic mass units for each successive species could be explained by an oxidative dehydrogenation and oxygen insertion process whereby the molecule loses two hydrogen atoms and gains one oxygen atom. The difference in retention times between each successive compound is 0.51 and 0.50 minutes, respectively, which may indicate that a family of compounds with similar differences in polarity is present.

The ratios of the intensity of different fragments of the ANL-RS2 and the two chemical oxidation products help reveal the identity of these products. In particular, fragments at 57, 59, and 73 are used to assess the changes in the ANL-RS2 molecule. The fragment at 57 m/z can be attributed to the *tert*-butyl group; the ratio of the intensity of this fragment to the intensity of the molecular ion remains fairly constant for all three compounds; therefore, the *tert*-butyl group appears to be present at the same amount in all three molecules. The fragment at 59 m/z is attributed to the $C_2H_4OCH_3$ group, and ANL-RS2 has two of them. The fragment at 73 m/z is attributed to the $C_2OH_2OCH_3$ group, which is the $C_2H_4OCH_3$ group with one oxygen atom added and two hydrogen atoms removed. The approximate ratio of the number of groups with 59 m/z and 73 m/z can be calculated for each molecule as seen in Table 19.

Since ANL-RS2 is known to contain two *tert*-butyl groups, these results imply that two *tert*-butyl groups are present in all three molecules. ANL-RS2 has two $C_2H_4OCH_3$ groups, while these results imply that ANL-RS2-O has one $C_2H_4OCH_3$ group and one $C_2OH_2OCH_3$ group, and that ANL-RS2-2O has two $C_2OH_2OCH_3$ groups. Proposed structures are presented in Figure 116 above. It should be noted that this chemical change, likely an oxidative dehydrogenation with an oxygen insertion, is infrequent compared to the usual electrochemical loss or gain of an electron, which is the redox shuttle mode of action. In addition to preventing the dimerization of aromatic compounds, the *tert*-butyl group can protect an ortho methoxy group from chemical reactions via a "key and lock" geometry, such as is present in 1,4-di-*tert*-butyl-2,5-dimethoxy benzene [17], but apparently is not large enough to protect the longer $OC_2H_4OCH_3$

groups that are present in ANL-RS2. The formation of an epoxide is consistent with the oxidative dehydrogenation/oxygen insertion process, but another oxygen-containing species may be formed instead. The compounds ANL-RS2-O and ANL-RS2-2O may react with the SEI layer or undergo polymerization at the anode, thus accounting for the increase in weight and decrease in porosity. Since these chemical oxidation products of ANL-RS2, namely ANL-RS2-O and ANL-RS2-O-O, are present in both the LFP-graphite and LFP-LTO overcharged cells, this implies that the cathode material may be responsible for their production. Interestingly, a substance that is known to catalyze oxidative dehydrogenation is $FePO_4$, which is produced when LFP is delithiated during the charging process [21]. It does not usually promote oxygen insertion when used as a gas phase catalyst, but may do so when utilized as an electrocatalyst.

The GC-MS analysis also revealed trends in the fractionation of the electrolyte components in the various cell components. Figures 121 through 124 show the relative amounts of redox shuttle species (RS), diethyl carbonate (DEC), and ethylene carbonate (EC) detected in electrolyte, separator, cathode, and anode extracts of LFP-graphite cells after formation, 10 overcharge cycles, and overcharge cycling to failure. The relative amounts of a given compound under different conditions can be interpreted in a semiquantitative manner.

The amount of redox shuttle species decreases most rapidly in the electrolyte, but also decreases in the separator, cathode, and anode extracts. This implies that the redox shuttle is being removed from the electrolyte, and that it is either being consumed or sequestered where it cannot be extracted in the separator, anode, and cathode samples, perhaps by becoming insoluble via a reaction or polymerization process. The relative amount of DEC is enriched and is found mainly in the electrolyte. It is well known that EC preferentially solvates the Li^+ due to its high dielectric constant, compared to DEC with its low dielectric constant; therefore, more EC is found at the anode and cathode due to the intercalation/deintercalation process, in which the desolvation of the Li^+ is necessary and likely enriches EC in the pores and on the surface of the active materials. In contrast, the EC and DEC are both slightly enriched in the separator sample in about the same amount as the overcharge cycling progresses compared to the redox shuttle species, because of the disappearance of some of the redox shuttle.

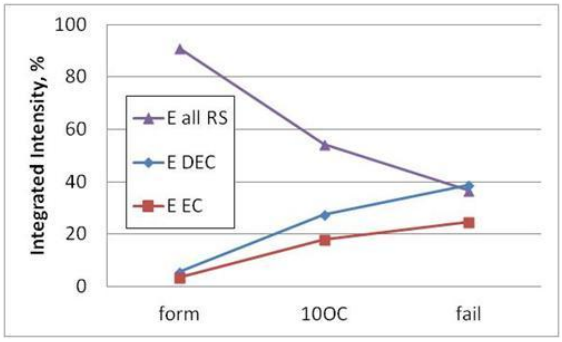

Figure 121. Integrated peak intensities for redox shuttle species (RS, purple triangles), diethyl carbonate (DEC, blue diamonds), and ethylene carbonate (EC, red squares) in electrolyte from LFP-graphite cells after formation, 10 overcharge cycles, and overcharge cycling to failure

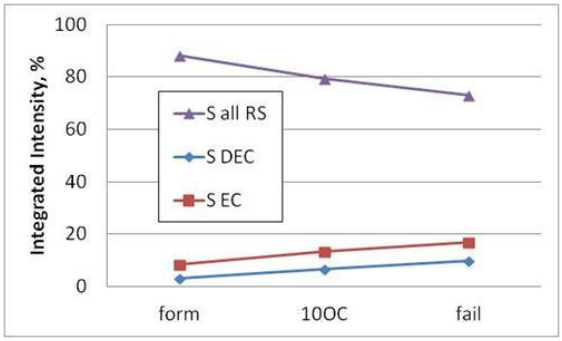

Figure 122. Integrated peak intensities for redox shuttle species (RS, purple triangles), diethyl carbonate (DEC, blue diamonds), and ethylene carbonate (EC, red squares) in separator extract from LFP-graphite cells after formation, 10 overcharge cycles, and overcharge cycling to failure

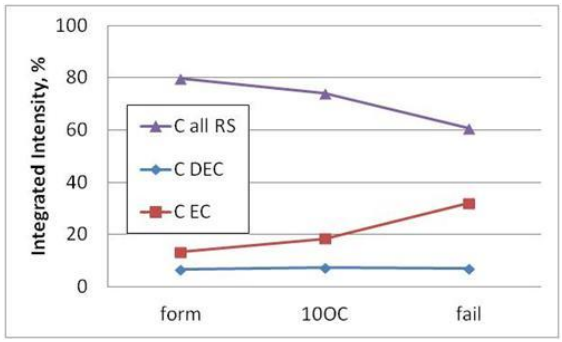

Figure 123. Integrated peak intensities for redox shuttle species (RS, purple triangles), diethyl carbonate (DEC, blue diamonds), and ethylene carbonate (EC, red squares) in cathode extract from LFP-graphite cells after formation, 10 overcharge cycles, and overcharge cycling to failure

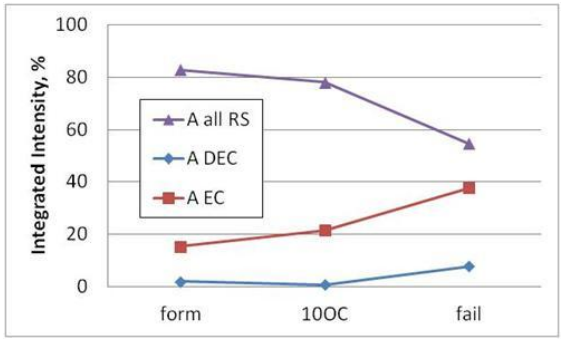

Figure 124. Integrated peak intensities for redox shuttle species (RS, purple triangles), diethyl carbonate (DEC, blue diamonds), and ethylene carbonate (EC, red squares) in anode extract from LFP-graphite cells after formation, 10 overcharge cycles, and overcharge cycling to failure

Scanning electron microscopy with energy dispersive spectroscopy was also employed to discern differences in the cell components with overcharge cycling. No visual differences were noted in the electrodes with overcharge cycling. The anodes, cathodes, and separators were then examined using EDS and the percentage of elements that were present was quantified. Results for the graphite anodes,

separators, and LFP cathodes from the LFP-graphite cell are presented in Figures 125, 126, and 127. The graphite anode contains less carbon and more oxygen, fluorine, and phosphorus as the overcharge cycling progresses. Increased oxygen content is consistent with ANL-RS2, its oxygen-containing degradation products, or organic carbonates or their degradation products being trapped or polymerized at the graphite surface. Increased fluorine and phosphorus content is consistent with the PF_6^- anion or its degradation products being present. The separator shows similar trends to the anode, but the elemental content of the cathode material is basically unchanged with overcharge cycling.

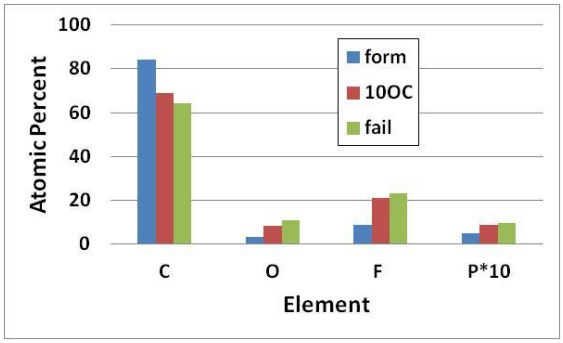

Figure 125. EDS analysis of the graphite anodes from the LFP-graphite full cells after formation, 10 overcharge cycles, and overcharge cycling to failure. Note that the phosphorus atomic percent is multiplied by 10 for clarity

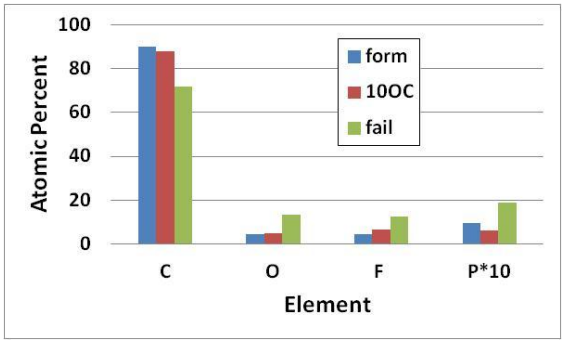

Figure 126. EDS analysis of the separator from the LFP-graphite full cells after formation, 10 overcharge cycles, and overcharge cycling to failure. Note that the phosphorus atomic percent is multiplied by 10 for clarity

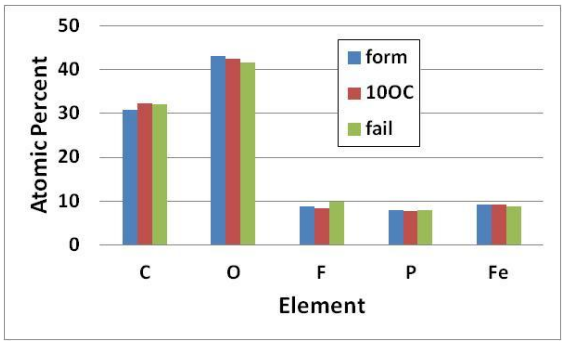

Figure 127. EDS analysis of the LFP cathodes from the LFP-graphite full cells after formation, 10 overcharge cycles, and overcharge cycling to failure

Thermal analysis was performed on the graphite anodes from the LFP-graphite cells. A baseline DSC was performed on pure ANL-RS2 and is presented in Figure 128. The apparent melting point is 71°C and the apparent heat of fusion is 29.6 kJ/mole. This agrees favorably with a calculated heat of fusion using the Joback method of 30.35 kJ/mole. The melting point of ANL-RS2 is lower than that of 1,4-di-tert-butyl-2,5-dimethoxybenzene, which is about 104°C.

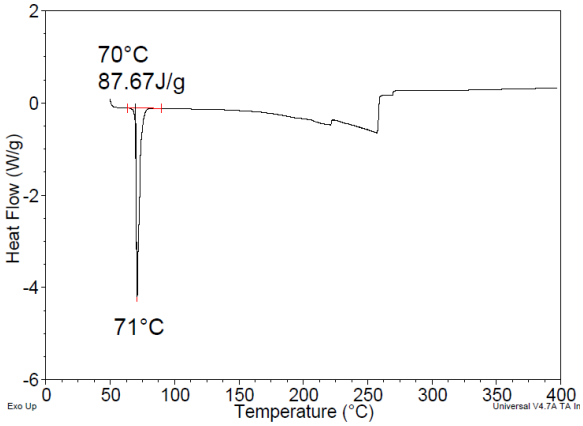

Figure 128. DSC of 8.61 mg of ANL-RS2 from 50 to 400°C with a ramp rate of 10°C/minute

The graphite anode from LFP-graphite cells that had undergone formation was analyzed using DSC and the results are in Figure 129. The endothermic peak at about 68°C can likely be assigned to the melting of ANL-RS2, the slightly lower melting point compared to the neat sample melting temperature due to colligative freezing point depression. The exothermic peak at about 90°C is slightly lower than is typical of SEI layer degradation at graphite anodes [18]. Since formation was performed in the presence of the ANL-RS2, some redox shuttle molecules were likely incorporated into the SEI layer.

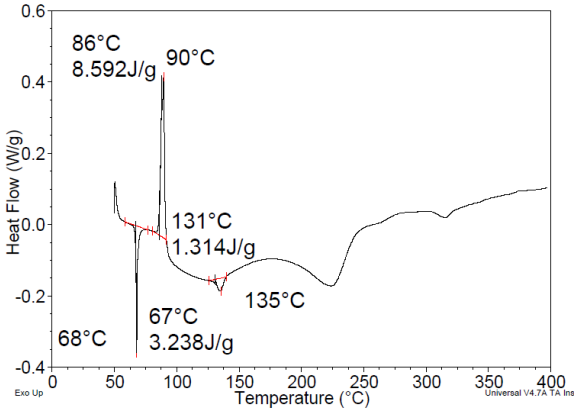

Figure 129. DSC of graphite anode after formation from LFP-graphite cell from 50 to 400°C with a ramp rate of 10°C/minute

The graphite anode from LFP-graphite cells that had undergone overcharge cycling to failure was analyzed using DSC and the results are presented in Figure 130. The endotherm due to the ANL-RS2 melt is almost completely absent, and the exotherm at 103°C that is typically assigned to SEI layer degradation is larger, releasing 19.5 J/g of heat compared to the 8.6 J/g of the formed graphite. This implies that the SEI layer is thicker, and/or is composed of different compounds after overcharge cycling compared to formation.

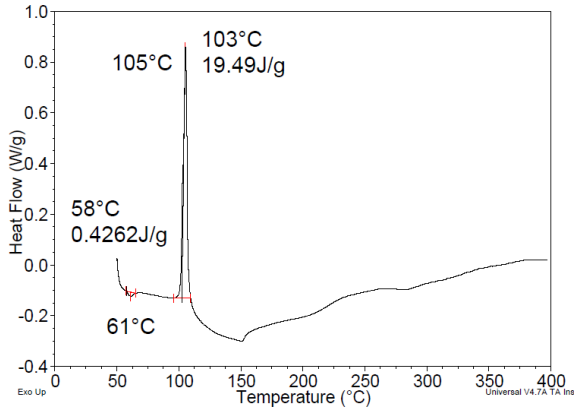

Figure 130. DSC of graphite anode after overcharge cycling to failure from LFP-graphite cell from 50 to 400°C with a ramp rate of 10°C/minute

TGA was then performed on the formed and overcharged cycled graphite and the results are presented in Figures 131 and 132. No weight loss occurs at the melting point of ANL-RS2, but weight loss does occur at the temperature where the exotherm associated with SEI layer degradation is observed, with an onset temperature of about 110°C. A larger weight loss is observed during the SEI layer degradation for the formed cell than the overcharged cell. This is likely due to the fact that the overcharged cell already degraded and generated gas, mainly carbon dioxide, during the overcharging process. The methoxyethane and 1,2-diethoxyethane that were detected in the GC-MS analysis of the evolved gas from the LFP-graphite cells are consistent with the presence of the ANL-RS2, which contains methoxyethoxy groups.

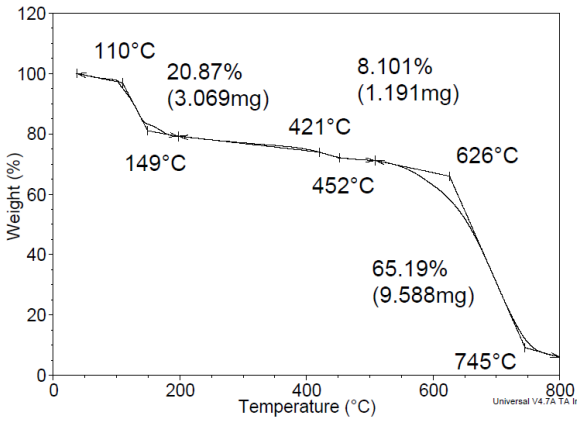

Figure 131. TGA of graphite anode after LFP-graphite cell formation from 50 to 800°C with a ramp rate of 10°C/minute

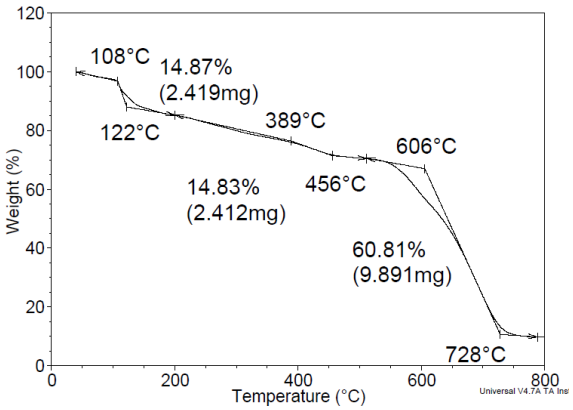

Figure 132. TGA of graphite anode after LFP-graphite cell overcharge cycling to failure from 50 to 800°C with a ramp rate of 10°C/minute

Vibrational spectroscopy was also employed to characterize the various cell components. The infrared spectrum of ANL-RS2 in solid phase is presented in Figures 133 and 134.

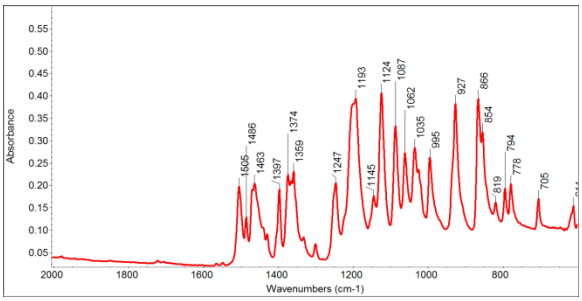

Figure 133. FTIR spectrum of ANL-RS2 from 600 to 2000 cm^{-1}.

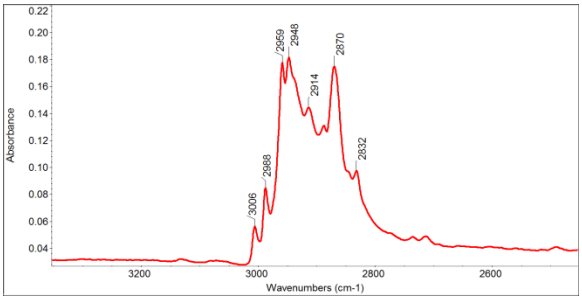

Figure 134. FTIR spectrum of ANL-RS2 in the C-H stretching region.

The electrolyte, anode, cathode, and separator samples were analyzed using attenuated total reflectance FTIR. Results for graphite electrodes and LFP electrodes from as formed and overcharge cycled cells are presented in Figures 135 through 138. It was noted that the ~1765 cm^{-1} to ~1806 cm^{-1} and the ~1191 cm^{-1} to ~1181 cm^{-1} ratios increase with overcharge cycling. These areas of the vibrational spectrum correspond to C=O and C-O stretching, respectively. Distinctive peaks attributable to ANL-RS2 were not observed in the infrared spectrum, presumably due to its lower concentration compared to other electrolyte components and perhaps also due to a lower absorption coefficient. Carbonyl and ether linkages are present in the organic carbonate solvents in the electrolyte, so it is difficult to separate their contributions to the FTIR spectrum from the redox shuttle and its chemically oxidized forms. Epoxide vibrations also occur in the same general area of the vibrational spectrum as ethers.

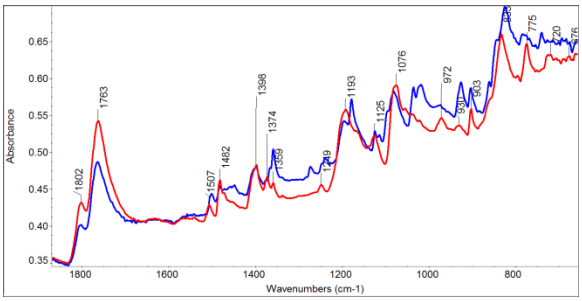

Figure 135. FTIR spectrum of graphite electrodes from LFP-graphite full cells. Blue trace: as formed. Red trace: overcharge cycled to failure.

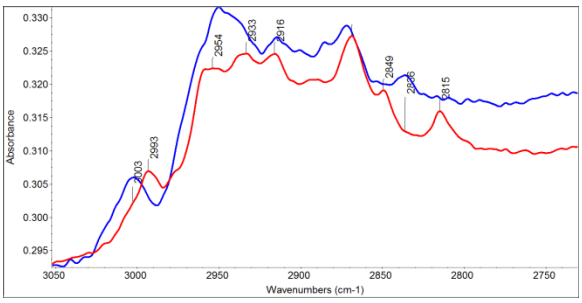

Figure 136. FTIR spectrum in the C-H stretching region of graphite electrodes from LFP-graphite full cells. Blue trace: as formed. Red trace: overcharge cycled to failure.

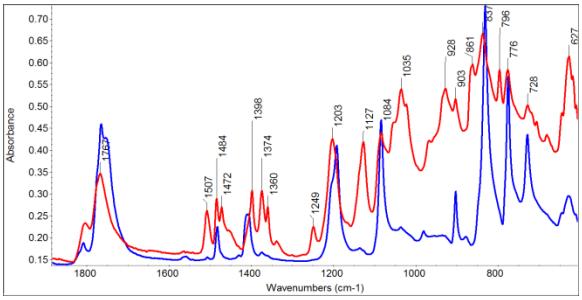

Figure 137. FTIR spectrum of LFP electrodes from LFP-graphite full cells. Blue trace: as formed. Red trace: overcharge cycled to failure.

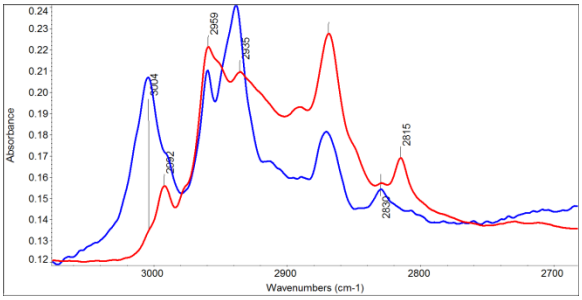

Figure 138. FTIR spectrum in the C-H stretching region of LFP electrodes from LFP-graphite full cells. Blue trace: as formed. Red trace: overcharge cycled to failure.

The Raman spectrum of ANL-RS2 is presented in Figures 139 and 140. Distinctive Raman peaks of ANL-RS2 include aromatic C-C stretching vibration at 1611 cm^{-1} and the aromatic C-H stretching vibration at 3112 cm^{-1}, which are not observed in the FTIR spectrum. As seen in Figures 141 and 142, these two peaks are clearly observed in the electrolyte sampled from the formed LFP-graphite cell; however, fluorescence interferes with the Raman spectrum obtained from electrolyte from the 10 overcharge cycle and failed LFP-graphite cells. The use of surface enhanced Raman spectroscopy may amplify the Raman signal to allow the observation of the ANL-RS2 and its chemical oxidation products [19].

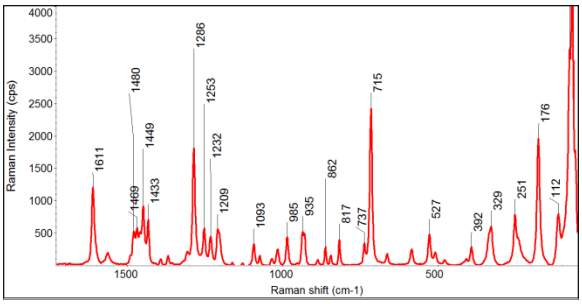

Figure 139. Raman spectrum of ANL-RS2.

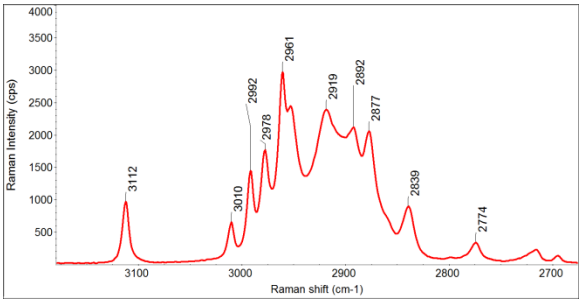

Figure 140. Raman spectrum of the C-H stretching region of ANL-RS2.

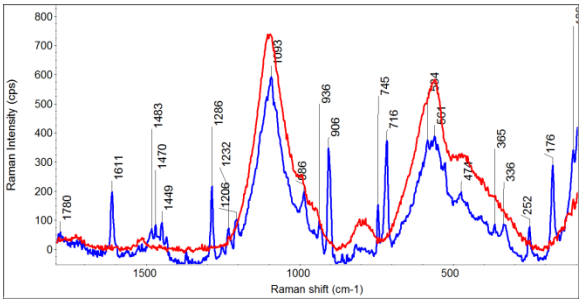

Figure 141. Raman spectrum of electrolyte from LFP-graphite full cells. Blue trace: as formed. Red trace: 10 overcharge cycles.

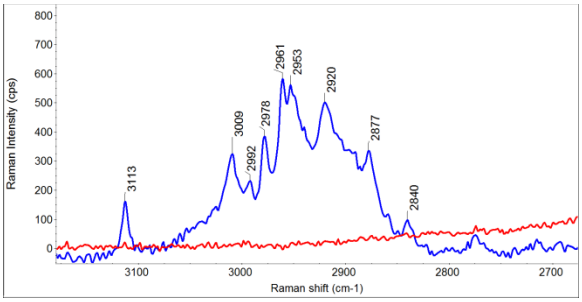

Figure 142. Raman spectrum in the C-H stretching region of electrolyte from LFP-graphite full cells. Blue trace: as formed. Red trace: 10 overcharge cycles.

3.18.5 Conclusions

This study attempted to explain the difference in overcharge cycling behavior between full cells with LFP cathodes and either graphite or LTO anodes. Using many different methods of analysis, the following conclusions were reached:

- ANL-RS2 is a redox shuttle molecule that provides overcharge protection to full cells employing LFP cathodes.
- Amongst other factors, full cells employing LFP cathodes and graphite anodes have a shorter overcharge cycle life compared to full cells employing LFP cathodes and LTO anodes due to the decreasing N/P ratio that occurs with overcharge cycling. Cells employing graphite anodes must have more negative capacity than positive capacity (N/P>1) to avoid lithium dendrite formation and achieve good cycleability. Cells employing LTO anodes actually cycle better when the N/P ratio is <1, so they are not as affected.

- The decrease in porosity and increase in density of graphite and LTO anodes with overcharge cycling may indicate a build-up of reaction products in the pores of these composite electrodes.
- ANL-RS2 contains two ethoxymethoxy groups which are too long to be protected by the ortho positioned tert-butyl group. Chemical oxidation, likely followed by more chemical reactions, occurs.
- ANL-RS2 appears to undergo an oxidative hydrogenation and oxygen insertion during overcharge cycling to form two new compounds which likely contain epoxide or other oxygen-containing moieties.
- The chemical oxidation of ANL-RS2 likely occurs at the LFP cathode in both the LFP-graphite and LFP-LTO cells.
- The formation of these new compounds, which may be chemically reactive, could be catalyzed by $FePO_4$ at the delithiated LFP cathode surface.

3.19 Reaction of SEI layer components with oxidized redox shuttle

It was previously observed that overcharged cells without redox shuttle in the electrolyte form little or no gas, while overcharged cells with redox shuttle in the electrolyte form observable quantities of gas. It is hypothesized that the oxidized form of the redox shuttle reacts with solid electrolyte interphase (SEI) layer components on the carbon anode and generate gas in the process. Various chemicals that are thought to be present in the SEI layer were oxidized to determine if gas is formed, and if so, to identify the gas that is formed.

First, oxidized ANL-RS2 redox shuttle was chemically prepared by reaction with nitronium hexafluorophosphate (NO_2PF_6) to form ANL-RS2$^+PF_6^-$. This oxidized ANL-RS2 should be identical to electrochemically generated oxidized ANL-RS2 produced at an LFP cathode during overcharge. Next, the oxidized ANL-RS2 was reacted with various chemicals believed to be present in the SEI layer and also with charged graphite and hard carbon electrodes in vials sealed with a septum. The gas was sampled and analyzed using a gas chromatograph – mass spectrometer (GC-MS). It should be noted that if any hydrogen was generated, is not detected in this analysis; the minimum mass-to-charge ratio was set at 6 due to helium being used as the carrier gas. The samples can be categorized into two different groups:

1. CO_2 as the major reaction product: Li_2CO_3
2. HF likely produced from the PF_6^-, as evidenced by various silicon-containing products, probably generated by reacting with the GC capillary column or glass liner: polyethylene oxide, $LiOCH_3$, $Li_2C_2O_4$, charged graphite, charged hard carbon

The gas produced by a LFP-graphite overcharged cell was also analyzed. In addition to the expected volatile linear carbonates present in the electrolyte, detected gases were CO_2, PO_3F, oxalic acid, methoxyethane, ethyl formate, and 1, 2-diethoxyethane. Since PO_3F is present, HF was likely also produced, but would probably not be detected since it reacts with various components of the cell, GC inlet liner, and GC column.

3.20 Detection of electrolyte components using Raman spectroscopy

It was earlier noted that it was difficult to detect ANL-RS2 present in electrolyte from an overcharged LFP-graphite cell using vibrational spectroscopy. The distinctive vibrations of the small amount of ANL-RS2 in electrolyte are too weak to be detected using FTIR, and fluorescence interfered with detection of ANL-RS2 in electrolyte from overcharged cells using Raman spectroscopy. It was

hypothesized that surface enhanced Raman spectroscopy (SERS) would amplify the signal from the ANL-RS2 and allow its detection. A ThermoFisher DXR Raman microscope was employed to collect the data.

LFP-graphite cells were formed and some were overcharged. The electrolyte was drained and mixed in a ratio of about 1:3 with a silver colloid solution prepared using the citrate method. An aqueous solution was used, but it is believed that better results may be obtained using a nonaqueous colloid or a prepared SERS substrate. The Raman spectrum of the colloid is presented in Figure 143. Excitation energy was 5 mW at 532 nm.

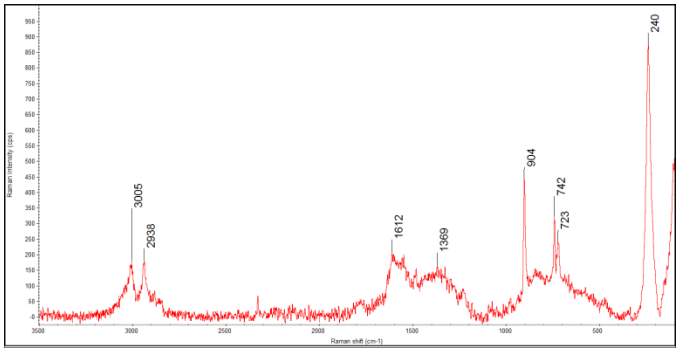

Figure 143. Raman spectrum of the Ag colloid prepared using the citrate method.

Next, the electrolytes were analyzed. Figure 144 shows the Raman spectra of the electrolyte and electrolyte with ANL-RS2 added. The higher intensity around 1603 cm^{-1} for the electrolyte with the ANL-RS2 added could be a result of the band that is observed at 1611 cm^{-1} in the solid state.

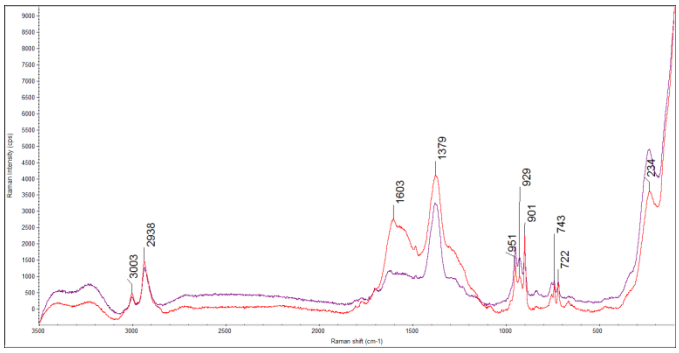

Figure 144. Raman spectra of electrolyte (purple) and electrolyte with ANL-RS2 (red) in Ag colloid.

Electrolyte from an overcharge cycled LFP-graphite cell was analyzed and compared to previous results. The blue trace in Figure 145 is a previous result and shows broad features and little detail. The red trace was collected using the Ag colloid and shows more vibrational detail.

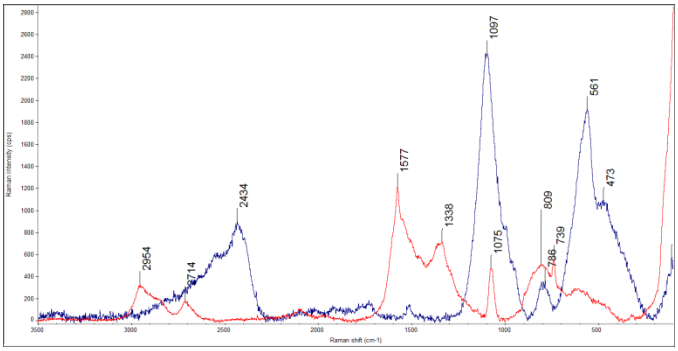

Figure 145. Raman spectra for electrolyte with ANL-RS2 drained from overcharged LFP-graphite cells. The blue trace is from electrolyte only, while the red trace is from electrolyte in Ag colloid.

The electrolyte (from an LFP-graphite formed cell) and Ag colloid mixture was dried to determine if a more intense signal could be obtained. The blue trace in Figure 146 is the wet mixture, and the red trace is the dried mixture. More vibrational detail can be seen in the dried mixture.

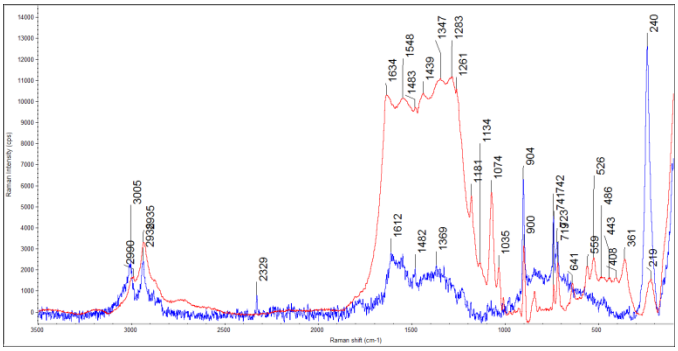

Figure 146. Raman spectra for electrolyte from formed cell. The blue trace is from the wet electrolyte and Ag colloid mixture, while the red trace is from the dried mixture.

Finally, a solution of $AgPF_6$ in electrolyte was applied directly to a charged graphite anode to determine if enhanced Raman signals would be obtained. Figure 147 shows the result. Many vibrational features can be seen in the spectrum, and it is believed that the addition of the Ag enhances the Raman signal.

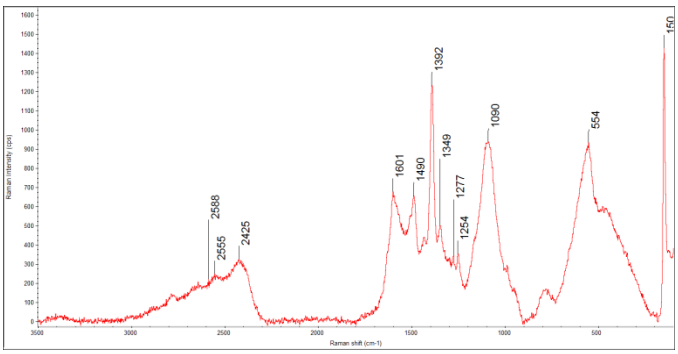

Figure 147. Raman spectrum of a charged graphite anode from a LFP-graphite cell with $AgPF_6$ added.

Analysis of the reaction products of chemically oxidized ANL-RS2 with SEI layer component compounds can help understand reactions that may occur at the anode in cells during overcharge.

Raman spectra can be generated for electrolyte and graphite surfaces using Ag colloid or $AgPF_6$ reduction. This may help characterize the reactions that occur in the electrolyte and at the anode surface during normal charge cycles and overcharge cycles.

3.21 Identification of the decomposition products of 1,4-di-tert-butyl-2,5-dimethoxybenzene (DDB)

A well-known and commercialized redox shuttle compound is 1,4-di-tert-butyl-2,5-dimethoxybenzene (DDB). It is available from 3M Corporation as 3M™ Redox Shuttle BE-3.9V. Its E^0 value of 3.9V is suitable for overcharge protection of cells employing lithium iron phosphate (LFP) cathodes. Its stability likely stems from steric protection of the methoxy groups by the adjacent tertiary butyl groups and has been described as a "lock-and-key" configuration [17].

DDB was added to electrolyte with composition ethylene carbonate:diethyl carbonate (EC:DEC) 3:7 and 1.2M $LiPF_6$. Lithium iron phosphate (LFP) – lithium titanate (LTO) cells with capacity 11 mAh were activated using this electrolyte and were subjected to overcharge cycling after formation. After about 40 overcharge cycles, the electrolyte was analyzed using gas chromatography – mass spectrometry (GC-MS).

Electrolyte drained from the cell was light brown and did not seem to be more viscous than the original electrolyte. The electrolyte was diluted in GC-MS grade methanol, analyzed using GC-MS, and the resulting chromatographic trace was analyzed. It was noted that the cell had become slightly swollen with a gaseous product. Previous analysis of this gas showed that it is mainly carbon dioxide (please note that hydrogen gas could have been present but not detected by this method).

DDB is one of the most stable redox shuttle agents for batteries. Accordingly, very small amounts of degradation products were detected. Methyl benzoate was detected, as was phthalic anhydride. Two unidentified compounds with apparent molecular weights of 128 and 143 g/mole were detected with retention times just before and just after that of diethylcarbonate. At least one of these compounds may contain fluorine, which could be provided by the $LiPF_6$ or its degradation products, or by the PVdF binder.

The trimethyl ester of phosphoric acid was detected in the electrolyte diluted in methanol. Therefore, phosphate from the LFP must have dissolved into the electrolyte. This indicates that the LFP cathode undergoes dissolution into the electrolyte during the overcharge cycling. There is likely a concomitant dissolution of iron, which would certainly plate on a carbon anode during cycling, and may plate on an LTO anode during cycling.

Conclusive identification of the degradation products requires the generation of larger amounts of these compounds. This could be accomplished by extended cell cycling. It was noted in an Argonne National Laboratory publication that it is difficult to identify the degradation products of DDB [20].

1,4-di-tert-butyl-2,5-dimethoxybenzene is one of the most stable redox shuttle agents for batteries. Its main degradation products are tentatively identified as methyl benzoate and phthalic anhydride. Additional degradation products may contain fluorine. Its E^0 value makes it appropriate for use in cells that employ LFP cathodes.

4 Conclusions

The desired characteristics for a successful redox shuttle species in a lithium ion cell are daunting. The shuttle must have stable electrochemistry over millions of oxidation-reduction cycles and also be stable over a large voltage window. Also, it must be chemically stable and non-reactive in both the oxidized and reduced forms toward all other cell chemicals and materials. Further, it must have a large diffusion coefficient and a large solubility in electrolyte to maximize the amount of current that can be shuttled. Lastly, the redox shuttle cannot interfere with the normal operation and performance of the lithium ion cell.

The best redox shuttle for lithium ion cells with LFP cathodes is DDB (3M), while the best redox shuttle for cells with 4.5 V class cathodes is $Li_2B_{12}F_{12}$ (Air Products, Showa Denko). These species have the best electrochemical and chemical stability of the redox shuttles that were tested. No redox shuttle was identified that is suitable for commercial use in lithium ion cells with NMC cathodes, which are usually operated at a maximum potential of about 4.1 to 4.2 V vs. Li^+/Li.

The eventual failure of the redox shuttle is likely caused by degradation products of the redox shuttle (and other electrolyte components) that cause a thickening of the resistive layer on the anode and a decrease of the electrode porosity. This probably causes an increase in localized temperature of the anode, which degrades the SEI layer and consumes cycleable lithium to repair the SEI layer. Further, the oxidized form of the redox shuttle of some species may be reactive enough to attack some of the SEI layer components.

Since the overcharge cycle life depends on the anode material, the redox shuttle must be tested in the full cell chemistry. Overcharge cycling in half cells may result in artificially enhanced results.

Molecular imprinting appears to play a role in the reduction of the oxidized redox shuttle species. This is a key finding that may help understand the fundamental mechanism of redox shuttle action.

5 PRESENTATIONS

1. Thomas Barbarich and Mary L. Patterson, "Effect of Anode on the Capacity Loss of Li-ion Cells with Redox Shuttles during Overcharge." 221st Meeting of the Electrochemical Society, Seattle, May 9, 2012.

2. Mary L. Patterson, "Perfluoro Aryl Boronic Esters as Redox Shuttle Additives in Lithium Ion Batteries." DOE Merit Review, Washington, DC, May 12, 2011.

3. Mary L. Patterson, "Molecular Imprinting: Does It Play a Role in the Reduction of Oxidized Redox Shuttle Molecules?" 219th Meeting of the Electrochemical Society, Montreal, May 5, 2011.

4. Mary L. Patterson, Mohamed Taggougui, and Adam J. Hunt, "Perfluoro Aryl Boronic Esters as Redox Shuttle Additives in Lithium Ion Batteries." 217th Meeting of the Electrochemical Society, Vancouver, April 27, 2010.

6 PUBLICATIONS

1. Thomas Barbarich and Mary L. Patterson, "Effect of Anode on the Capacity Loss of Li-ion Cells with Redox Shuttles during Overcharge." ECS Trans. 45 (29), 49 (2013).
2. Mary L. Patterson, "Perfluoro Aryl Boronic Esters as Redox Shuttle Additives in Lithium Ion Batteries." DOE Merit Review, Washington, DC, May 12, 2011.
3. M.L. Patterson. "Molecular Imprinting: Does It Play a Role in the Reduction of Oxidized Redox Shuttle Species?" ECS Trans. 35 (32), 203 (2011).
4. M.L. Patterson and M. Taggougui. "Perfluoro Aryl Boronic Esters as Redox Shuttle Additives in Lithium-Ion Batteries." ECS Trans. 28 (30), 69 (2010).

7 PATENT APPLICATION

U.S. Patent “Redox Shuttle for High Voltage Lithium Battery”, U.S. Patent Application 2012/0244,446, published Sept. 27, 2012.

8 GLOSSARY

ANL Argonne National Laboratory

ANL-RS001 another name for BDB 2-(pentafluorophenyl)-tetrafluoro-1,3,2-benzodioxaborole

ANL-RS2 1,4-bis(2-methoxyethoxy)-2,5-di-*tert*-butyl-benzene

ARC accelerated rate calorimetry

BDB 2-(pentafluorophenyl)-tetrafluoro-1,3,2-benzodioxaborole

CV cyclic voltammetry or cyclic voltammogram

DDB 2,5-di-tert-butyl-1,4-dimethoxybenzene

DEC diethyl carbonate

DSC differential scanning calorimetry

EC ethylene carbonate

EI electron impact ionization

EIS electrochemical impedance spectroscopy

EMC ethyl methyl carbonate

FTIR Fourier transform infrared spectroscopy

GC-MS gas chromatography – mass spectrometry

HC hard carbon

LFP lithium iron phosphate

$Li_2B_{12}F_{12}$ dilithium dodecafluorododecacarborate

LiBOB lithium bisoxalatoborate

LiF lithium fluoride

LMO lithium manganese oxide

$LiPF_6$ lithium hexafluorophosphate

LTO lithium titanium oxide

NMC lithium nickel manganese cobalt oxide

N/P negative-to-positive

PC propylene carbonate

SEI solid electrolyte interphase

SEM scanning electron microscopy

SOC state of charge

TGA thermogravimetric analysis

TFC tetrafluorocatechol

VC vinylene carbonate

9 ACKNOWLEDGEMENTS

The author wishes to acknowledge technical contributions to this report by Thomas J. Barbarich, Ph.D., who performed much of the redox shuttle testing in cells. Further, the initial diffusion coefficient measurements on the 2-(pentafluorophenyl)-tetrafluoro-1,3,2-benzodioxaborole (BDB) redox shuttle were performed by Mohamed Taggougui, Ph.D. and Ms. Ashley Brockhaus. The author would also like to thank Dr. Christopher Johnson and Ms. Brittley Robbins of NETL, who provided much appreciated support during the course of the program.

10 REFERENCES

[1] G. GirishKumar, W.H. Bailey III, B.K. Peterson, and W.J. Casteel, Jr., "Electrochemical and Spectroscopic Investigations of the Overcharge Behavior of StabiLife Electrolyte Salts in Lithium-Ion Batteries", *J. Electrochem. Soc*., **158**, A146 (2011) and Z. Chen, J. Liu, A.N. Jansen, G. GirishKumar, B. Casteel, K. Amine, "Lithium Borate Cluster Salts as Redox Shuttles for Overcharge Protection of Lithium-Ion Cells", Electrochem. Solid-State Lett. 13 (4) A39 (2010).

[2] J. Chen, C. Buhrmester, and J. R. Dahn, "Chemical Overcharge and Overdischarge Protection for Lithium-Ion Batteries", Electrochem. Solid-State Lett., **8**, A59 (2005) and J. R. Dahn, J. Jiang, L. M. Moshurchak, M. D. Fleischauer, C. Buhrmester, and L. J. Krause, "High-Rate Overcharge Protection of LiFePO4-Based Li-Ion Cells Using the Redox Shuttle Additive 2,5-Ditertbutyl-1,4-dimethoxybenzene", J. Electrochem. Soc., **152**, A1283 (2005).

[3] C. L. Campion, W. Li, W. B. Euler, B. L. Lucht, B. Ravdel, J. F. DiCarlo, R. Gitzendanner and K. M. Abraham, "Suppression of Toxic Compounds Produced in the Decomposition of Lithium-Ion Battery Electrolytes", Electrochem. Solid-State Lett., 7, A194 (2004).

[4] M. Tang and J. Newman, "Electrochemical Characterization of SEI-Type Passivating Films Using Redox Shuttles", *J. Electrochem. Soc.*, **158**, A530 (2011).

[5] C. Alexander, H.S. Andersson, L.I. Andersson, R.J. Ansell, N. Kirsch, I.A. Nicholls, J. O'Mahony, and M.J. Whitcombe, "Molecular imprinting science and technology: a survey of the literature for the years up to and including 2003", *Journal of Molecular Recognition*, **19**, 106 (2006).

[6] L.M. Moshuchak, M. Bulinski, W.M. Lamanna, R.L. Wang, and J.R. Dahn, "Direct comparison of 2,5-di-tert-butyl-1,4-dimethoybenzene and 4-tert-butyl-1,2-dimethoxybenzene as redox shuttles in LiFePO4-based Li-ion cells", *Electrochemistry Communications*, **9**, 1497-1501 (2007).

[7] L.M. Moshurchak, C. Buhrmester, R.L. Wang, and J.R. Dahn, *Electrochim. Acta*, "Comparative studies of three redox shuttle molecule classes for overcharge protection of $LiFePO_4$-based Li-ion cells", **52**, 3779 (2007).

[8] E. Peled, D. Golodnitsky, C. Menachem, and D. Bar-Tow, "An Advanced Tool for the Selection of Electrolyte Components for Rechargeable Lithium Batteries", J. Electrochem. Soc., 145, 3482 (1998).

[9] M. Tang and J. Newman, "Transient Characterization of Solid-Electrolyte-Interphase Using Ferrocene", *J. Electrochem. Soc*. **159** (3), A281-A289 (2012).

[10] M.N. Golovin, D.P. Wilkinson, J.T. Dudley, D. Holonko, and S. Woo, "Applications of Metallocenes in Rechargeable Lithium Batteries for Overcharge Protection", J. *Electrochem. Soc.*, **139**, 5 (1992).

[11] H.J. Ploehn, P. Ramadass, and R.E. White, "Solvent Diffusion Model for Aging of Lithium-Ion Battery Cells", J. Electrochem. Soc., 151, A456 (2004).

[12] D. Aurbach, K. Gamolsky, B. Markovsky, Y. Gofer, M. Schmidt, and U. Heider, "On the use of vinylene carbonate (VC) as an additive to electrolyte solutions for Li-ion batteries", *Electrochim. Acta*, 47, 1423 (2002).

[13] K. Xu, "Charge-Transfer" Process at Graphite/Electrolyte Interface and the Solvation Sheath Structure of Li + in Nonaqueous Electrolytes", *J. Electrochem. Soc*., **154**, A162 (2007).

[14] J. Dahn, J. Jiang, L. Moshurchak, C. Buhrmester, and R.L. Wang, "The Drugstore Li-ion Cell", *The Electrochemical Society Interface*, **Winter 2005**, 27 (2005).

[15] L. Zhang, Z. Zhang, and K. Amine, in *Lithium Ion Batteries – New Developments*, I. Belharouak, Editor, p. 184, InTech, Rijeka, Croatia (2012).

[16] H.M. Wu, I. Belharouak, H. Deng, A. Abouimrane, Y.-K. Sun, and K. Amine, "Development of LiNi0.5Mn1.5O4/Li4Ti5O12 System with Long Cycle Life"**,** *J. Electrochem. Soc*., **156** A1047 (2009).

[17] C. Buhrmester, J. Chen, L. Moshurchak, J. Jiang, R.L. Wang, and J.R. Dahn, "Studies of Aromatic Redox Shuttle Additives for $LiFePO_4$-Based Li-Ion Cells"**,** *J. Electrochem. Soc.*, **152**, A2390 (2005).

[18] A.M. Andersson, M. Herstedt, A.G. Bishop, and K. Edstrom, "The influence of lithium salt on the interfacial reactions controlling the thermal stability of graphite anodes", *Electrochimica Acta*, **47** 1885-1898 (2002).

[19] T.J. Tague Jr., M. Leona, and P. Wang, "Raman Spectroscopy of Documents", *Spectroscopy (Special Issue)*, (April 1, 2010).

[20] Z. Chen and K. Amine, "Degradation pathway of 2,5-di-tert-butyl-1,4-dimethyoxybenzene at high potential", *Electrochim. Acta*, **53**, 453 (2007).

[21] M. Ai and K. Ohdan, "Oxidation by iron phosphate catalyst, J. Mol. Catal. A, **159** 19 (2000).

END OF DOCUMENT